Light-Responsive Polymer Systems Aiming Towards Programmable Friction

The Application Driven Development of 9-Anthracene Ester-Terminated Silicone Oils and Spiropyran Graft Copolymers as Novel Functional Materials

Dissertation

Submitted for the Degree

Doctor Rerum Naturalium

(Dr. rer. nat.)

In the Discipline Polymer Science

by

Chris Gäbert

At the
Faculty of Science
Institute of Chemistry
University of Potsdam
and the
Fraunhofer Institute for Applied Polymer Research IAP

Place and Date of the Disputation: Potsdam-Golm, 10.06.2022

Abstract

The development of novel programmable materials aiming to control friction in real-time holds potential to facilitate innovative lubrication solutions for reducing wear and energy losses. This work describes the integration of light-responsiveness into two lubricating materials, silicon oils and polymer brush surfaces.

The first part focusses on the assessment on 9-anthracene ester-terminated polydimethylsiloxanes (PDMS-A) and, in particular, on the variability of rheological properties and the implications that arise with UV-light as external trigger. The applied rheometer setup contains an UV-transparent quartz-plate, which enables radiation and simultaneous measurement of the dynamic moduli. UV-A radiation (354 nm) triggers the cycloaddition reaction between the terminal functionalities of linear PDMS, resulting in chain extension. The newly-formed anthracene dimers cleave by UV-C radiation (254 nm) or at elevated temperatures (T > 130 °C). The sequential UV-A radiation and thermal reprogramming over three cycles demonstrate high conversions and reproducible programming of rheological properties. In contrast, the photochemical back reaction by UV-C is incomplete and can only partially restore the initial rheological properties. The dynamic moduli increase with each cycle in photochemical programming, presumably resulting from a chain segment re-arrangement as a result of the repeated partial photocleavage and subsequent chain length-dependent dimerization. In addition, long periods of radiation cause photooxidative degradation, which damages photo-responsive functions and consequently reduces the programming range. The absence of oxygen, however, reduces undesired side reactions. Anthracene-functionalized PDMS and native PDMS mix depending on the anthracene ester content and chain length, respectively, and allow fine-tuning of programmable rheological properties. The work shows the influence of mixing conditions during the photoprogramming step on the rheological properties, indicating that material property gradients induced by light attenuation along the beam have to be considered. Accordingly, thin lubricant films are suggested as potential application for light-programmable silicon fluids.

The second part compares strategies for the grafting of spiropyran (SP) containing copolymer brushes from Si wafers and evaluates the light-responsiveness of the surfaces. Pre-experiments on the kinetics of the thermally initiated RAFT copolymerization of 2-hydroxyethyl acrylate (HEA) and spiropyran acrylate (SPA) in solution show, first, a strong retardation by SP and, second, the dependence of SPA polymerization on light. Surprisingly, the copolymerization of SPA is inhibited in the dark. These findings contribute to improve the synthesis of polar, spiropyran-containing copolymers. The comparison between initiator systems for the grafting-from approach indicates PET-RAFT superior to thermally initiated

ABSTRACT

RAFT, suggesting a more efficient initiation of surface-bound CTA by light. Surface-initiated polymerization via PET-RAFT with an initiator system of EosinY (EoY) and ascorbic acid (AscA) facilitates copolymer synthesis from HEA and 5-25 mol% SPA. The resulting polymer film with a thickness of a few nanometers was detected by atomic force microscopy (AFM) and ellipsometry. Water contact angle (CA) measurements demonstrate photo-switchable surface polarity, which is attributed to the photoisomerization between non-polar spiropyran and zwitterionic merocyanine isomer. Furthermore, the obtained spiropyran brushes show potential for further studies on light-programmable properties. In this context, it would be interesting to investigate whether swollen spiropyran-containing polymers change their configuration and thus their film thickness under the influence of light. In addition, further experiments using an AFM or microtribometer should evaluate whether light-programmable solvation enables a change in frictional properties between polymer brush surfaces.

Die Entwicklung neuartiger programmierbarer Materialien zur Anpassung von Reibung in Echtzeit birgt Potenzial, innovative Schmierungslösungen zu ermöglichen, um Verschleiß und Energieverluste zu reduzieren. Die vorliegende Arbeit beschreibt die Integration von Lichtlichtschaltbarkeit in zwei schmierende Materialien, Silikonöle und Oberflächen mit Polymerbürsten.

Der erste Teil konzentriert sich auf die Bewertung von 9-Anthracenester-terminierten Polydimethylsiloxanen (PDMS-As) und insbesondere auf die Veränderbarkeit der rheologischen Eigenschaften sowie Implikationen, die sich bei der Verwendung von UV-Licht als externe Trigger ergeben. Der verwendete Rheometeraufbau enthält eine UV-transparente Quarzplatte, welche somit die Bestrahlung bei gleichzeitiger Messung der dynamischen Moduli ermöglicht. UV-A-Strahlung (354 nm) löst die Cycloadditionsreaktion zwischen den endständigen Funktionalitäten des linearen PDMS aus und führt so zu einer Kettenverlängerung. Die dabei gebildeten Anthracen-Dimere werden durch UV-C-Strahlung (254 nm) oder bei erhöhten Temperaturen (T > 130 °C) gespalten. Die sequentielle UV-A-Bestrahlung und thermische Reprogrammierung in drei Schaltzyklen führen zu hohen Umsätzen und zeigen reproduzierbar einstellbare Materialeigenschaften. Im Gegensatz dazu ist die photochemische Rückreaktion durch UV-C unvollständig und kann die ursprünglichen rheologischen Eigenschaften nur teilweise wiederherstellen. Die dynamischen Module nehmen mit jedem Zyklus der photochemischen Programmierung zu, was vermutlich auf eine Neuanordnung der Kettensegmente infolge der wiederholten partiellen Photospaltung und der anschließenden kettenlängenabhängigen Dimerisierung zurückzuführen ist. Darüber hinaus kommt es bei langer Bestrahlungsdauer zu einem photooxidativen Abbau, der die

ABSTRACT

photoschaltbaren Funktionen des Silikons beeinträchtigt und folglich den Programmierbereich verringert. Der Ausschluss von Sauerstoff reduziert jedoch unerwünschte Nebenreaktionen. Anthracenfunktionalisiertes PDMS und unfunktionalisiertes PDMS mischen sich in Abhängigkeit vom Anthracenestergehalt beziehungsweise der Kettenlänge und ermöglichen die Feinabstimmung programmierbarer rheologischer Eigenschaften. Die Arbeit zeigt den Einfluss der Mischungsbedingungen während des Photoprogrammierungsschritts auf die rheologischen Eigenschaften, was darauf hindeutet, dass Materialeigenschaftsgradienten, die durch Lichtabschwächung entlang des Lichtstrahls entstehen, berücksichtigt werden müssen. Entsprechend werden dünne Schmiermittelfilme als mögliche Anwendung für lichtprogrammierbare Silikonöle vorgeschlagen.

Der zweite Teil vergleicht ‚grafting-from'-Methoden zur Synthese Spiropyran(SP)-haltiger Copolyme auf Si-Wafern und bewertet die Lichtschaltbarkeit der Oberflächeneigenschaften. Vorversuche zur Kinetik der thermisch initiierten RAFT-Copolymerisation von 2-Hydroxyethylacrylat (HEA) und Spiropyranacrylat (SPA) in Lösung zeigen erstens, eine starke Retardierung durch SP, und zweitens, die Lichtabhängigkeit der SPA-Polymerisation. Überraschenderweise ist die Copolymerisation von SPA im Dunkeln gehemmt. Diese Ergebnisse tragen dazu bei, die Synthese von polaren, spiropyranhaltigen Copolymeren zu verbessern. Der Vergleich zwischen Initiatorsystemen für den ‚grafting-from'-Ansatz zeigt, dass PET-RAFT der thermisch initiierten RAFT überlegen ist, was auf eine effizientere Initiierung von oberflächengebundenem CTA durch Licht hindeutet. Die oberflächeninitiierte Polymerisation via PET-RAFT mit einem Initiatorsystem aus EosinY (EoY) und Ascorbinsäure (AscA) ermöglicht die Copolymersynthese aus HEA und 5-25 mol% SPA. Der entstandene Polymerfilm mit einer Dicke von einigen Nanometern wurde mittels Rasterkraftmikroskopie (AFM) und Ellipsometrie nachgewiesen. Die Messungen des Wasserkontaktwinkels (CA) zeigt eine photoschaltbare Oberflächenpolarität, welche der Photoisomerisierung zwischen unpolaren Spiropyran und zwitterionischen Merocyanin-Isomer zugeschrieben wird. Darüber hinaus zeigen die erhaltenen Spiropyranbürsten Potenzial für weitere Untersuchungen zu lichtprogrammierbaren Eigenschaften. In diesem Zusammenhang wäre es interessant weiterführend zu untersuchen, ob gequollene spiropyranhaltige Polymere unter Lichteinfluss tatsächlich ihre Konfiguration und damit ihre Filmdicke ändern. Darüber hinaus wäre es sinnvoll, mit Hilfe eines AFM oder Mikrotribometers zu evaluieren, ob diese lichtprogrammierbare Solvatisierung eine Veränderung der Reibungseigenschaften zwischen Polymerbürstenoberflächen ermöglicht.

Acknowledgement

List of Schemes

LIST OF SCHEMES

List of Figures

LIST OF TABLES

List of Tables

List of Abbreviations

A-COCl	9-Anthracenecarbonyl chloride
A-COOH	9-Anthracenecarboxylic acid
AFM	Atomic force microscopy
AscA	Ascorbic acid
AIBN	Azobis(isobutyronitril)
ATR	Attenuated total reflection
ATRP	Atomic transfer radical polymerization
APTES	(3-Aminopropyl)-triethoxysilane
BF	Bright-field microscopy
Bipy	2,2'-Bipyridine
BTPA	2-(N-butyltrithiocabonate)-propionic acid
CA	Water contact angle
CD	Cyclodextrin
COSY	Correlated spectroscopy (NMR)
CTA	Chain transfer agent
CVD	Chemical vapor deposition
DABCO	1,4-Diazabicyclo[2.2.2]octane
DFT	Density function theory
DMAM	N,N-Dimethyl acrylamide
DMF	Dimethylmethanamide
DMSO	Dimethyl sulfoxide
DoD	Degree of dimerization
DoF	Degree of functionalization
EDC·HCl	1-Ethyl-3-(3-dimethylaminopropyl)-carbodiimid hydrochloride
Et al.	Et alia, and others
EoY	Eosin Y; 7, 2',4',5',7'-Tetrabromfluorescein
FM	Fluorescence microscopy
HALS	Hindered amine light stabilizer
HDI	Hexamethyelene diisocyanate
HEA	2-Hydroxy acrylate
I.e.	Id est, that is to say
LCST	Lower critical solution temperature
LED	Light emitting diode
MC	Merocyanine

NAM	4-Acryloylmorpholine
NMR	Nuclear magnetic resonance spectroscopy
NMP	N-Methyl-2-pyrrolidon (solvent)
	Nitride-oxide mediated polymerization (polymerization technique)
OEGA	Oligo(ethylen glycol) acrylate
Ppy	2-Phenylpyridine
PEG	Poly(ethylene glycol)
PDMAM	Poly(N,N-dimethyl acrylamide)
PDMS	Poly(dimethylsiloxane)
	9-anthracene ester-terminated polydimethylsiloxane
	PDMS-A with
PDMS-A	$x = 0$, [ ], 2, 3 running number referring to the used precursor
PDMSX-A$_y$	PDMSX-(OH)$_2$
	$y = 1$; 2 number of functionalized termini per chain
	hydroxyethoxypropyl-terminated PDMS
PDMS-OH	bis(hydroxyethoxypropyl)-terminated PDMS
PDMSX-(OH)$_2$	with
	$x = 0$, [ ], 2, 3 running number referring to a specific molar mass
PET-RAFT	Photo-induced electron/energy transfer RAFT
PFA	Perfluoroalkoxy alkanes
PHEA	Poly(2-hydroxyethyl acrylate)
PHEA$_x$SPA$_y$	Poly(2-hydroxyethyl acrylate-co-2-spiropyranethyl acrylate)
	x and y refer to the feedratio of HEA and SPA relative to the CTA
PMAA	Poly(methylacrylic acid sodium salt)
PNAM	Poly(4-acryloylmorpholine)
PNIPAM	Poly(N-isopropyl acrylamide)
POEGA	Poly[oligo(ethylenglycol) acrylate]
PTFE	Polytetrafluoroethylen
RAFT	Reversible addition-fragmentation chaintransfer
Ref	Reference
RT	Room temperature
RI	Refractive index
SEC	Size exclusion chromatography
SP	Spiropyran
SPA	2-Spiropyranethyl acrylate
SPOH	2-Spiropyranethyl alcohol

LIST OF ABBREVIATIONS

SPP	2-Spiropyranethyl propionate
STM	Scanning tunnel microscopy
THF	Tetrahydrofuran
TRISAM	N-[Tris(hydroxymethyl)methyl] acrylamide
TTP	5,10,15,20,-Tetraphenylporphyrin
UV	Ultraviolet light
VIS	Visible light

Table of Contents

1. Introduction

1.1 The Advantages of Programmable Materials for Lubrication Solutions

The ability to passively adapt or actively regulate an inherent property of a material sets new standards in technology and engineering. So-called programmable materials are considered suitable to replace entire control peripherals consisting of sensors, controllers and actuators. The integrated functionality facilitates on-demand programming of the material behavior in response to an external signal such as temperature or light and therefore improves the overall performance or even enables novel applications. The targeted development of programmable materials is a promising strategy to address technological challenges and reach higher resource and energy efficiency.

Global energy consumption is a crucial problem that must be addressed in order to create a modern sustainable society. In this context, friction deserves special attention as a phenomenon that generally occurs in mechanical systems in motion. Friction contributes to the conversion of energy through heat loss, to the wear of parts and to their replacement, which is costly in terms of resources and energy. Holmberg and Erdemir reviewed the global impact of friction and studied the two largest energy consumption sectors in this context. Transportation and industry alone consumed more than 70 % of the global oil in 2019.[1] After analyzing these sectors, the authors conclude that about 20% of the energy produced worldwide is required to overcome friction.[2]

Normally, mechanical systems are lubricated to optimize their friction behavior. The resulting reduced wear and energy requirements enable smooth and continuous machine operation and extend the service life of the mechanical connections. Consequently, lubrication is economically and ecologically profitable.

Lubrication solutions are highly individual. Each friction system is characterized by specific friction pair materials, occurring temperatures, shear forces, loadings and other parameters that need to be taken into account for the selection of an appropriate lubricant. Most friction systems operate under dynamic conditions, meaning that parameters such as load or velocity change over time. This usually forces engineers to compromise on the selection of a conventional lubricant suitable for a specific range of friction conditions encountered. A programmable lubrication system, on the other hand, allows the real-time adjustment to the current friction conditions. The following Chapter 1.2 surveys friction scenarios and identifies possible applications for programmable lubricating materials.

1.2 Scenarios for the Application of Light-Programmable Friction

The application potential of a programmable material depends on the engineering effort arising with the implementation of the external trigger to control the material response, and on the performance of the material itself. A detailed knowledge about programming parameters such as graduation, range, timescale, reprogramming fatigue and more is crucial to envision a particular utility.

This section on the application potential of programmable friction systems focusses on switching with light. Controlling a material with light has many advantages over other external stimuli. Useful light sources are relatively cheap and easy to implement. Commercially available components such as LEDs, lenses and optical filter are sufficient to precisely control the radiated area, wavelength and intensity. The light can be switched instantly, facilitating rapid material programming. However, a typical limitation of light-programming is the necessity to build certain components of a device from light-transmissive materials. Another challenge is homogeneous programming of photo-responsive bulk materials, since light is attenuated as it travels through an absorbing medium. Nevertheless, the lubricating layers between machine parts are usually very thin, as the friction evolves from the nature of the surface[3] or the viscosity of a few micron lubricant layer.[4] In addition, inhomogenities in lubricating layers can be eliminated by mixing under the influence of shear. Alternatively, the lubricant can also be fed through an external programming and mixing unit.

The first friction scenario that offers feasible applications for light-programmable lubricants is a classic bearing. In a plain bearing, a lubricated journal rotates in relative motion to an outer cylindrical housing part (Scheme 1A). The friction of this system is determined by the state of the friction gap that is described by the Stribeck curve (Scheme 1B).[5] In the first regime, the so-called boundary regime, the friction pair is barely separated and the high contact area of the rough surfaces lead to high friction. The second regime is the mixed regime, in which an increasing surface separation causes reduced contact of the asperities thus lowering friction. This regime can be envisioned as an intermediate state between the first and the third regime. The latter is referred to as hydrodynamic lubrication regime. The contact of the surfaces in this regime is negligible, since as the surfaces are completely separated by the lubricant in the gap. Scheme 1B shows three friction curves assigned to particular lubricants and plotted as a function of load and velocity. The solid and the dotted black curve represent two conventional lubricants that differ from each other by the value of their immutable viscosity. Interestingly, either one or the other of the conventional lubricants shows a better friction performance at a

certain sliding speed under the assumption of a constant load. High viscosity lubricants support the journal loading better at low sliding speeds whereas low viscosity lubricants perform better at high sliding speeds. A programmable lubricant that undergoes controlled change in viscosity at x_1 is represented by the red curve. Clearly, matching the viscosity to either one of the invariable lubricants, flattens the Stribeck curve and combines the advantages of both conventional lubricants over the whole range of velocity. In addition, it is conceivable that light-programmable viscosity is beneficial to compensate for undesired changes of a lubrication system due to aging.
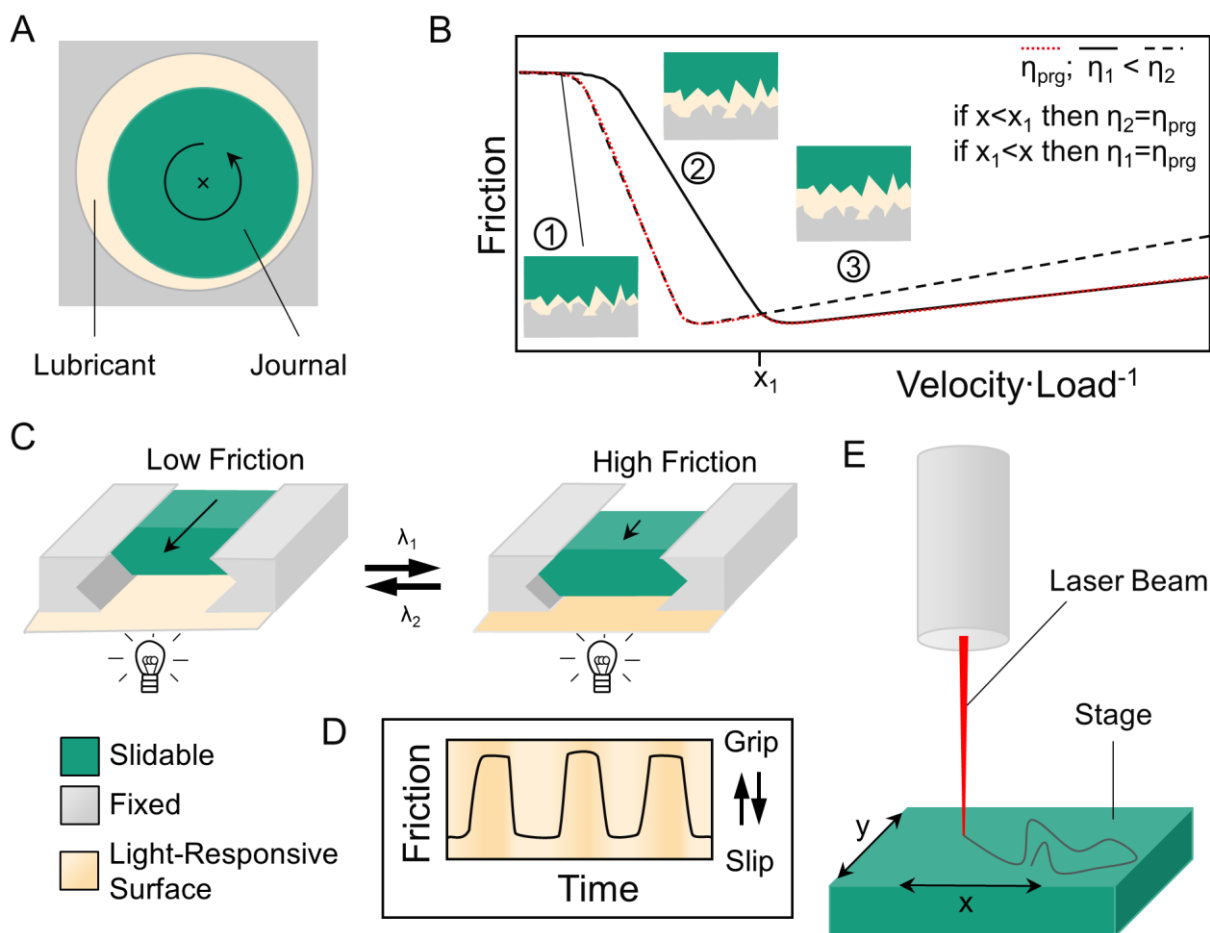
Scheme 1:   *Application scenarios for polymers featuring light-programmable friction properties. First, the fluid-lubricated friction between solid surfaces in a journal bearing (A) is described by the Stribeck curve (B). It depends on the viscosity of the lubricant and the load as well as the velocity of the rotating journal. The second describes a photo-responsive microactuator system (C) for improved positioning stages for example applied in a lithography process (E). The graph (D) describes the variation of friction over time between the 'slip' and 'grip' states.*

The second scenario illustrated in Scheme 1C describes a photo-switchable microactuator. It is composed of a slidable element in contact with a surface made of a light-responsive material. The light source located under the switchable surface requires the aforementioned use of optically transparent materials. During the positioning process, the slidable element moves to a specific position. At this stage, the surface is ideally slippery to avoid heat losses and material

wear. Once the selected position is reached, the sliding element must stop immediately to ensure flawless positioning precision. Consequently, the grip to the programmable surface assists the system in the braking process and can thus improve the positioning time or precision. A perfect photo-programmable material for such an application must respond quickly and, moreover, be capable of undergoing many programming cycles between two states with very different coefficients of friction without showing signs of fatigue. Scheme 1D exemplifies the time course of the friction coefficient between a 'grip' and a 'slip'-state. Such microactuators are important, for example, for working stages that could be used in laser writing processes (Scheme 1C). In these processes, the laser spots are relatively small compared to the manufactured structure, so that fast and at the same time precise work stages are advantageous.

1.3 Rheology

Rheology[6] is the study of flow behavior. The rheological characterization of lubricants is relevant because, as described in Chapter 1.2, certain parameters such as viscosity determine the frictional performance of a lubricant. The method is based on the principle of analyzing the response of a material to an applied mechanical force. Material responses can be described as a combination of two behaviors, elasticity and viscosity.

Ideal elastic behavior follows Hook's law (1) and is usually represented by a spring. The shear stress τ is proportional to the shear strain γ.

$$\tau_G = G \cdot \gamma \tag{1}$$

However, it has to be noted that polymer materials, such as rubber, exhibit non-linear behavior. As soon as the deflection exceeds a certain value, plastic deformation occurs so that the material cannot reversibly return to its initial state.

Ideal viscous behavior follows Newton's law (2) and is usually represented by a Newtonian fluid in a dashpot. The shear stress τ is proportional to the shear rate $\dot{\gamma} = \frac{d\gamma}{dt}$ of the fluid.

$$\tau_\eta = \eta \cdot \dot{\gamma} \tag{2}$$

However, most polymeric materials, such as polymer melts, do not exhibit linear flow behavior. Their shear stress typically depends on the shear rate (Figure 1A). Structurally, this can be explained by the disentanglement and the orientation of polymer chains along the direction of motion as respective shear rates and forces increase. Consequently reduced viscosity or 'inner friction' appears, since oriented chains slide past each other more easily. This case is referred to as shear thinning. Figure 1C shows an example of several shear thinning curves for narrowly distributed PDMS polymer melts of different molar masses. According to the empirical Equations (3), curves with higher viscosity at zero shear assign to higher molar masses.

$$if \ M < M_C \ then \ \eta_o = k_1 \cdot M$$
$$if \ M > M_C \ then \ \eta_0 = k_2 \cdot M^{3.4} \tag{3}$$

In contrast, other materials such as aqueous solutions of starch show an increase of viscosity with increasing shear rate. This phenomenon is called shear thickening.

In addition, the viscosity of materials can change over time when a shearing is applied (Figure 1B). If the viscosity decreases with shearing time, it is called thixotropy, while an increase over time is referred to as rheoplexia. These effects originate from a breaking of chemical bonds or from increasing intermolecular interactions over time, respectively.
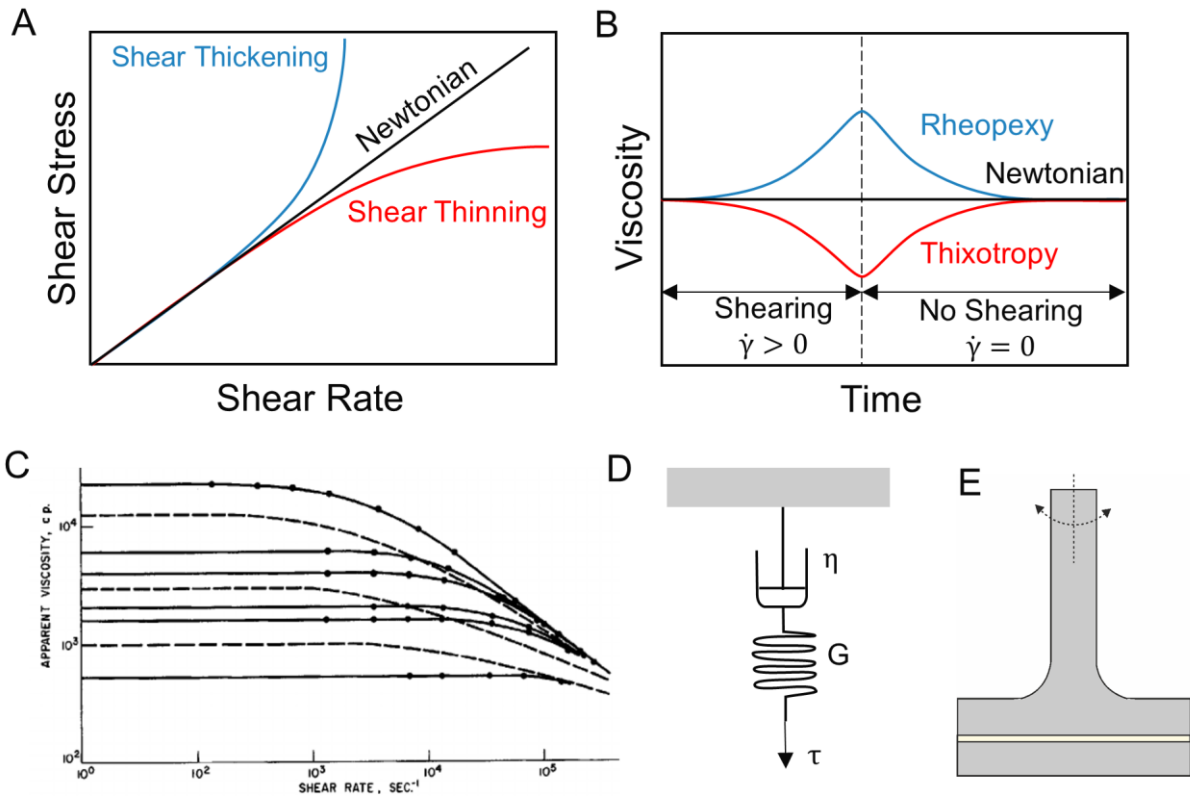
Figure 1: Shear rate-dependent (A) and time-dependent (B) flow behavior of Newtonian and non-Newtonian fluids. (C) Series of shear thinning curves of PDMS melts of different molar masses. Reprinted from ref[7] with permission with permission from John Wiley & Sons https://doi.org/10.1002/pol.1970.160081106 (25.11.21). Copyright © 1970 WILEY-VCH Verlag (D) A Maxwell-model composed of a dashpot and a spring in a series. (E) A rheometer in plate-plate geometry.

Polymers exhibit both elastic and viscous properties and are accordingly described as viscoelastic materials. A low shear stress model proposed by Maxwell for this purpose consists of a spring and a dashpot connected in series (Figure 1D). Both elements consider only linear responses and are subjected to the same stress (4). The shear deformation, on the other hand, is composed of the individual components (5).

$$\tau = \tau_G = \tau_\eta \tag{4}$$

$$\frac{d\gamma}{dt} = \frac{d}{dt}(\gamma_G + \gamma_\eta) = \frac{d\tau}{dt}\frac{1}{G} + \frac{\tau}{\eta} \tag{5}$$

In the case of a sudden shear strain the time dependence for stress-function is given by

$$\tau(t) = G\gamma_0 \cdot e^{\left(-\frac{t}{\lambda}\right)} \ and \ \lambda = \frac{\eta}{G} \tag{6}$$

in which λ is the relaxation time. The deformation leads to an increase in shear stress, which slowly decreases with the relaxation time.

The viscoelastic properties of a material are typically measured by a rheometer. In one example of a typical test setup, the material is placed between two round plates (Figure 1E). A defined shear rate is then applied and the shear stress is measured via the torque. Alternatively, a defined shear stress can also be applied while the necessary shear rate is measured.

In case of oscillating deformation (7), the response of the shear stress (8) results with the same frequency. However, there is a material-dependent phase shift of the response function expressed by the phase angle δ, originating from the viscous response part.

$$\gamma(t) = \gamma_0 \cdot sin\,(\omega t) \tag{7}$$

$$\tau(t) = \tau_0 \cdot sin\,(\omega t + \delta) \tag{8}$$

According to the addition theorem, the response function can also be described as the sum of two wave functions.

$$\tau(t) = \gamma_0 G'(\omega) \cdot sin(\omega t) + \gamma_0 G''(\omega) \cdot cos(\omega t) \tag{9}$$

$$with\; G'(\omega) = \frac{\tau_0}{\gamma_0} \cdot cos(\delta) \;\; and \;\; G'' = \frac{\tau_0}{\gamma_0} \cdot sin(\delta) \tag{10}$$

The first term of the wave function (9) describes a material response in phase with the applied frequency, which corresponds to the elastic response. Accordingly, G' is called the storage modulus. The second term of the wave function (9) is shifted by 90° and describes the viscous behavior of the system. Accordingly, G'' is referred to as the loss modulus. The ratio between $\frac{G''}{G'} = \tan(\delta)$ is called the loss factor. This ratio describes the state of a material, since fluids have a larger loss modulus (G'' > G') and gels and other solids have a larger storage modulus (G' > G''). G' and G'' are the real and imaginary part, respectively, of the complex modulus G* according to

$$G = G' + iG'' \tag{11}$$

1.4 The Mechanism of RAFT and Photochemical Initiation

The reversible addition-fragmentation chain transfer (RAFT) polymerization is a classic method of controlled radical polymerization.[8] It follows a first-order kinetic and allows the synthesis of polymers with a narrow molar mass distribution and defined end groups.

Unlike the other typical controlled radical polymerization methods, ATRP[9] and NMP[10], which rely on reversible deactivation of radicals, RAFT is based on rapid transfer reactions of radicals. RAFT requires no transition metals, is tolerant to a wide range of functionalities, and provides access to different polymer architectures, such as random copolymers or block copolymers. Accordingly, RAFT is a useful tool for the synthesis of many different polymer materials including stimuli-responsive polymers.[11] This section introduces the mechanism of RAFT polymerization, highlighting in particular the photochemical initiation possibilities of this method. The synthesis of polymer brushes by RAFT is discussed in the following Section 1.5. The mechanism of the RAFT-polymerization is shown in *Scheme 2*. The polymerization (ii) is initiated by a radical source (i). The radical generation can be induced by thermal decomposition of azo compounds or by photochemical processes, which is described later in this section. The propagating polymer chains reacts with the chain transfer agent (CTA) in a pre-equilibrium (iii). The formed intermediate adduct can be cleaved, leading to a dormant polymer chain bound to the CTA (macro-CTA) and an R-group radical. This radical can reinitiate to form another propagating polymer chain (iv). The main equilibrium of the RAFT mechanism is the shuttling of radicals by the macro-CTA between different polymers chain termini (v). The addition and fragmentation rates of the equilibria (iii and v) are higher than the chain propagation rate (ii), so that a similar degree of polymerization is obtained for all chains at each time of the process.

The terminal thiocarbonylthio group of the obtained polymers is very versatile as shown more in detail in Scheme 3. For example, it can be used as macro-CTA in a subsequent RAFT polymerization for the synthesis of block copolymers. Moreover, it can be converted into a thio group that in turn can react as nucleophile.

i) $\quad$ Radical Source $\longrightarrow$ $I^{\bullet}$ $\xrightarrow{\quad M \quad}$ $P_1^{\bullet}$

ii) $\quad P_n^{\bullet}$ $\xrightarrow{\quad M \quad}$ $P_{n+1}^{\bullet}$

iii) $\quad P_n^{\bullet} +$ [thiocarbonylthio structure with S, S–R, Z] $\rightleftharpoons$ [intermediate radical P_n–S, S–R with Z] $\rightleftharpoons$ [P_n–S, =S with Z] $+ R^{\bullet}$

iv) $\quad R^{\bullet}$ $\xrightarrow{\quad M \quad}$ $P_1^{\bullet}$

v) $\quad P_n^{\bullet} +$ [thiocarbonylthio structure S, S–P_m, Z] $\rightleftharpoons$ [intermediate radical P_n–S, S–P_m with Z] $\rightleftharpoons$ [P_n–S, =S with Z] $+ P_m^{\bullet}$

vi) $\quad P_n^{\bullet} + P_m^{\bullet}$ $\longrightarrow$ P_{n+m} or $D_n + D_m$
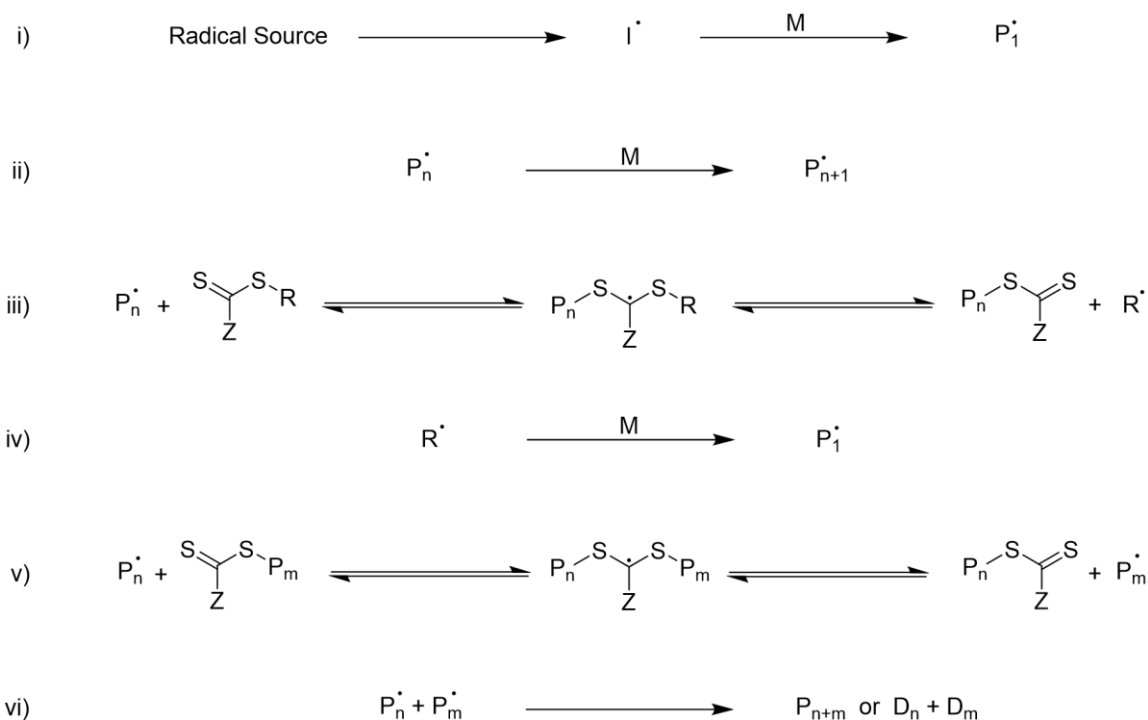
Scheme 2: *Mechanism of RAFT polymerization. i) radical initiation of a polymer chain ii) radical polymer chain propagation iii) pre-equilibrium of RAFT iv) reinitiating reaction of the R-group radical v) main equilibrium of RAFT vi) termination reaction leading either to biradical recombination or disproportionation.*
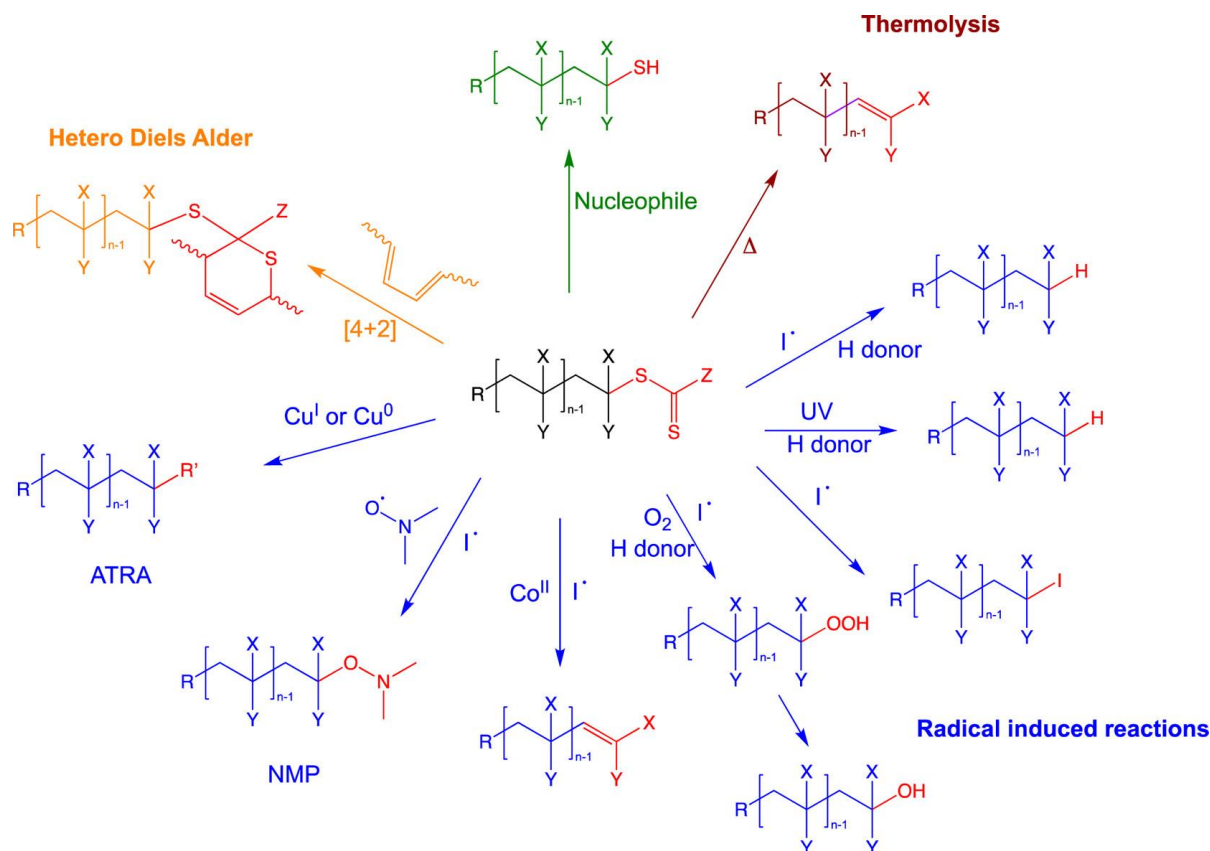
Scheme 3: *Common routes of thiocarbonylthio-group modification. Reprinted from ref[8] with permission of the ACS https://doi.org/10.1021/acs.macromol.7b00767 (22.11.2022). Copyright © 2017 American Chemical Society; further permissions related to the material excerpted should be directed to the ACS.*

Several mechanisms for photo-initiated RAFT polymerizations are known. According to the first possibility, the CTA can activate the polymerization directly without the need for an additional photoinitiator or catalyst. In this case, the CTA is an iniferter, meaning that it acts as both initiator and chain transfer agent.[12] Hartlieb recently reviewed photoinitiated RAFT polymerizations summarizing different CTA structures and initiation wavelengths. As an example, the review describes that CTAs bearing a trithiocarbonate group enable polymerizations using UV or VIS light.[13] The second photoinitiation mechanism, known as PET-RAFT, involves the excitation of a photocatalyst and a transfer process to the initiating species. It is debatable whether this is an energy or electron transfer. A recent review by Allgrezza and Konkolewicz, for instance, shows arguments for both routes and concludes that likely each catalyst system has unique characteristics.[14] In this regard, the paper mentions $Ir(ppy)_3$, $Ru(bpy)_3^{2+}$, ZincTTP and Eosin Y as common PET photocatalysts. PET-RAFT is an interesting and sustainable polymerization method due to its good catalyst recyclability, selectivity, spatio-temporal polymerization control and oxygen tolerance.[15] The oxygen tolerance is based on the fact that PET systems consume molecular dissolved oxygen by converting it into singlet oxygen, which subsequently reacts further with solvent molecules or reducing agents.[15] This requires the oxygen diffusion to outweigh the oxygen consumption, so that a small interface with the air and sufficient photocatalyst concentration are advantageous. Nevertheless, an appropriate setup offers the technically desirable advantage of eliminating the need for elaborate oxygen removal methods, thus saving effort and energy.

1.5 Polymer Grafting for the Synthesis of Polymer Brushes

In polymer grafting, polymer branches are introduced into the backbone of a preformed polymer precursor or into a composite material. The method thus enables the synthesis of surface-bound polymer brushes. Among other applications, polymer brushes are considered to form effective lubricating surfaces.[16] The application of polymer brushes as lubricants is discussed in more detail in Chapter 1.6.2.2. The following section provides a brief introduction to the synthesis of surface-bound polymer brushes and highlights mechanistic considerations for surface-initiated RAFT polymerization.

Two basic strategies facilitate the synthesis of polymer brushes, the grafting-to and the grafting-from approach (Scheme 4). Grafting-to involves the selective anchoring of terminal polymer domains to the surface of a material. The binding strength of the polymer to the surface depends on the type of attachment. It can be based on physical interactions[17] or on the formation of chemical bonds. A review by Zdyrko and Luzinov summarizes grafting-to methods for the immobilization of polymers on various inorganic and polymeric substrates and gives many examples of applied chemical reactions such as click chemistry, esterification, amidation, epoxide reactions and silanization.[18] In general, the grafting density achievable by grafting-to is kinetically limited due to the necessity of the diffusion of the reactive groups of the sterically demanding polymer chain to the substrate. A diffusion barrier builds up during the grafting process, as already immobilized polymer chains overlap and stretch.[19]
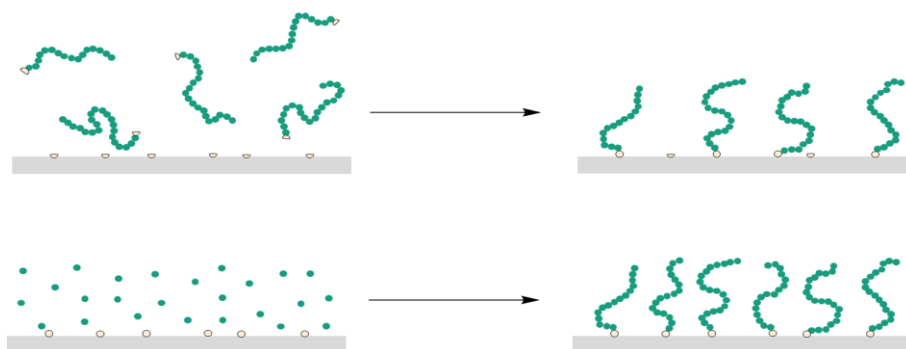
Scheme 4:   Grafting-from (top) and grafting-to (bottom) approach for the synthesis of surface-anchored polymer brushes.

Grafting-from, on the other hand, is a bottom-up process with which a higher graft density can be achieved. In this process, the polymer is obtained from a monomer solution by surface-initiated polymerization. Controlled radical polymerization methods are suitable for this purpose, as they provide access to different polymer architectures, facilitate thickness control and enable a uniform polymer layer. Compared to other controlled and living polymerization

types, the radical approach exhibits high compatibility with a wide range of functional groups in organic as well as aqueous media. Accordingly, ATRP, NMP and RAFT are established processes for the synthesis of polymer brushes.[20]

The mechanism of RAFT is described in Chapter 1.4. In surface-initiated polymerization by RAFT, the CTA is immobilized on the surface of a respective substrate. For this purpose, the CTA may be attached through two different ways. In the case of binding via the Z-group (see *Scheme 2*), the polymer chain grows in solution, so the method suffers from steric shielding by dormant surface-bound polymer chains, similar to what was described previously for 'grafting-to'. The alternative is to attach the CTA via the R group. However, this creates the problem that the CTA detaches during polymerization. It could be shown that the CTA detachment leads to the entrapment of radicals and a broadening of the molar mass distribution. However, the 'CTA-shuttled RAFT' approach overcomes this problem, which makes the linkage via the R group attractive. The method uses additional solubilized CTA so that radical transfer between the surface-bound radical and the solubilized reaction side is increased.[21]

1.6 State of Art

1.6.1   Photo-Reversible Structures and Programmable Polymers

Recently, light-responsive polymeric materials have received special attention for the development of novel programmable materials. Their advantages in terms of friction applications and the benefits of implicating light as an external trigger are discussed in Sections 1.1 and 1.2. Light-responsive polymers usually contain certain structural motifs that can undergo reversible photochemical reactions from a stable into another, metastable state. In this context, the energy barrier of the metastable state determines the kinetic inhibition of the thermal back reaction. The photochemical reactions lead to the formation of new covalent bonds and to changes of certain molecular properties such as polarity. These switching mechanisms are used in photochemical building blocks of responsive materials in such a way that they enable switchable macroscopic properties. Examples are described in Sections 1.6.1.1, 1.6.1.2 and 1.6.2.1. Ideally, photo-responsive building blocks in programmable materials react rapidly, selectively and with full conversion under ambient reaction conditions. The most common structures and their reaction mechanisms that sufficiently satisfy these conditions are shown in Scheme 5.

All the reactions depicted are, in principle, reversible under the application of certain wavelengths. The first class is based on conjugated π-systems that undergo reversible cycloaddition under the influence of electromagnetic radiation (Scheme 5A). Since anthracene esters, a representative of this class, are one of the main focuses of this work (see Chapter 2.1 and 3.1), these structures are reviewed in more detail in the first Subchapter 1.6.1.1. The other focus (see Chapter 2.2 and 3.2) is on materials that utilize the photochromism of spiropyran (SP) and merocyanine (MC) (Scheme 5B), which is described in the second Subchapter 1.6.1.2.

Another prominent photo-reversible moiety, which, however, will not be further addressed in this thesis, are azobenzene derivatives (Scheme 5C).[22,23,24] These molecules can isomerize between the cis and the trans form, which affects both the spatial demand and the polarity of the molecule. In addition, the trans isomer complexes selectively with cyclodextrins (CD), while the cis isomer does not form such a complex for steric reasons.[25,26–28] A fourth class of light-switchable structures are diarylethenes (Scheme 5D). Light of certain wavelengths triggers their intramolecular cyclisation and reversion, respectively, leading to a three-dimensional

rearrangement of the substituents. Diarylethenes are popular for the design of programmable materials due to their fast photoresponsibility, thermal stability and fatigue resistance.[29,30]
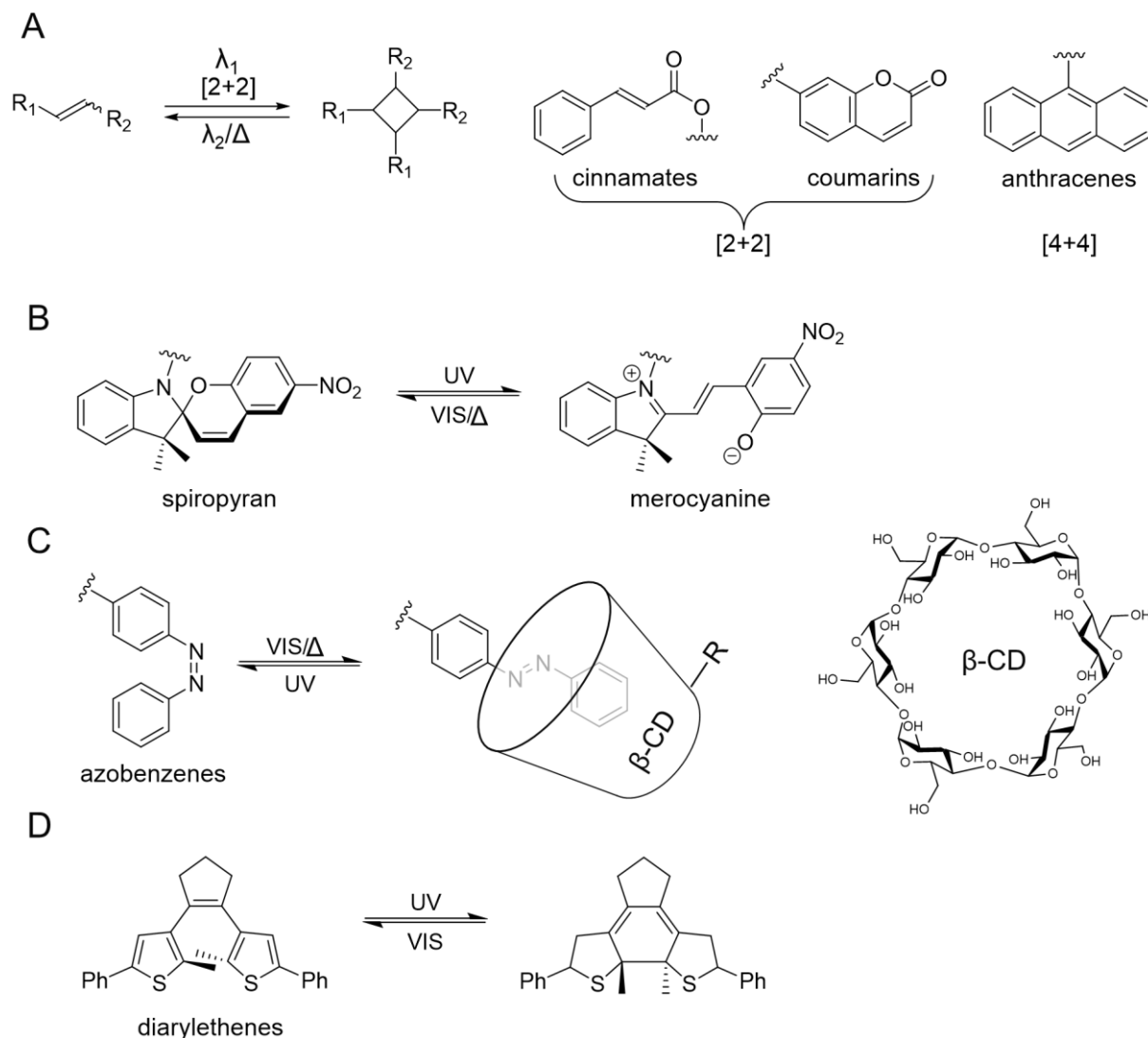
Scheme 5: *Commonly employed light-responsive building blocks. (A) π-Systems, for example, cinnamates, coumarins and anthracenes undergo reversible cycloaddition and –reversion reactions. (B) The photochromism of the SP and MC isomer. (C) Cis//trans-isomerization of azobenzenes and the trans-selective complexant β-CD. (D) Intramolecular cyclisation of diaryl ethenes.*

1.6.1.1 Cycloaddition Type and Functional Silicones

Photochemical cycloaddition reactions are an efficient and versatile method for linking macromolecules.[31] Cinnamates[32,33,34,35], coumarins[36–38], anthracenes[39–41] and others[42,43] are capable of covalently and reversibly linking chemical structures, thus enabling light-programmability of functional materials. The exposure of these motifs to light of a particular wavelength induces an intermolecular reaction via a [2+2] or [4+4] cycloaddition mechanism and hence leads to corresponding photodimers (Scheme 5A). The conjugation size of the π-systems as well as their substituents influence the electronic energy gap of the π-π*-transition and thus determine the excitation wavelength.[43,44] The respective photodimers exhibit a smaller π-system and show altered physiochemical properties such as solubility[45,46] and absorption wavelength. Consequently, cycloreversion requires light of lower wavelength.[35] Alternatively, the cleavage of photodimers can be achieved by heat[39,47] or mechanical stress.[33,48]

Radiation of cinnamates is usually accompanied by undesirable side reactions such as cis/trans-isomerization.[49] Another disadvantage for the use of cinnamates and coumarins is the low wavelengths required for the photoreaction, which can lead to a number of even more uncontrolled side reactions and thus even compromise the reversibility of the dimerization. Anthracene derivatives, on the other hand, have a smaller energy gap and dimerize accordingly at higher wavelengths. The exact excitation wavelengths and dimerization kinetics can also be influenced by the substituents.[41] Higher excitation wavelengths are considered more practical for the development of programmable materials, as the selective excitation energy reduces the occurrence of side reactions. Furthermore, there are readily available light sources such as LEDs for the excitation wavelengths of anthracenes. Zheng at al. report good programmability of anthracene-modified polymers by demonstrating 14 photoprogramming cycles without fatigue.[50] The publication also shows another typical characteristic of the photochemical programming of anthracene dimers. The conversions of the photochemical back reactions are only about 15%, meaning that the reaction is far from complete. This can be explained by the fact that radiation with UV-C causes not only photochemical cleavage but also simultaneous dimerization, since both species absorb at this wavelength. As a result, a quasi-stationary equilibrium is established.[51]

Polydimethylsiloxanes (PDMS) are a suitable platform for the preparation of functional materials based on cycloaddition reactions due to their good UV transparency and chemical inertness. Previous reports on light-programmable silicones including the feature of photo-programmable cycloaddition focus on network formation and evaluate such materials for self-

healing material,[52] surface pattering,[32,53] biomedical applications,[38] elastomers with adjustable moduli,[54] and as thermoplastic elastomer[37] or vitrimer.[39]

1.6.1.2 Spiropyran and Functional Copolmers

Spiropyran (SP) exhibits unique switchable physiochemical properties and, accordingly, has emerged to be a popular function for the design of photo-switchable polymers.

Ultraviolet light (UV) triggers the ring opening of the SP isomer by heterocyclic cleavage leading to the merocyanine (MC) isomer (Scheme 5B). The MC isomer consists of an extended π-system in which the central double bond conjugates the indole structure to the substituted benzene ring. In this form, the compound absorbs and emits visible light and shows broad peaks with maxima around 550 nm and 650 nm, respectively.[55,56] In contrast, the SP isomer exhibits two separate aromatic systems that absorb only in the UV range letting the SP structure appear colorless and show almost no fluorescence.[57] Typically, the SP isomer is thermodynamically more stable. Accordingly, ring closure occurs spontaneously. Nevertheless, it can be accelerated by visible light (VIS) and heat. The SP isomer is neutral and therefore significantly differs from the zwitterionic MC isomer by a decreased dipole moment ($\Delta \mu \approx 40$ C·m^{-30}).[58] The zwitterionic structure promotes attractive forces to metal ions[59] and other MCs[60]. For example, SP containing macromolecules show light-switchable chain configuration and solubility due to the light-assisted switching between SP and MC isomer and the resulting interactions.[61,62] In addition, photoisomerization leads to a change of the molecular volume[63] and promotes the weak basicity of the MC isomer. The pK_a value of the conjugated acid (HMC$^+$) is around ~2.2.[64]

In general, the isomerization of SP is triggered by multiple stimuli and possesses strong system dependence.[65] Typical influences include ring substituents,[57,66,67] adjacent groups,[68,69] solvent polarity,[55,70] pH,[56,59,68,71–73] temperature,[56,71–75] metal ions,[59,72] and mechanical force.[67,76,77] The versatility of the SP motif is evident from the stimuli-responsive properties of SP based materials and their applications.[78] For example, SP polymers are developed for imaging techniques,[57,79] as colorimetric thermometer,[70] for self-assembling micelles,[62,80] switchable wettability,[60,81] controlled cell adhesion,[82] triggered drug release,[71,83] light-switchable membrane permeability[84] or as photoactuators for microfluidic valves.[85,86]

Note: The sole term 'spiropyran' (SP) is used within this chapter including both photoisomers. The particular isomers are referred as either 'SP isomer' or 'MC isomer'.

SP polymers can contain the photo-responsive function as a dopant, at the chain end, in the main chain or in the side chain. The integration of SP in the side chain gives access to polymers with a high content of functional building blocks. Such polymers are obtained by post-polymerization modification, or alternatively, by direct polymerization of the corresponding monomers. Free radical polymerization is a direct and facile method for the syntheses of SP copolymers as reported for example of acrylates, methacrylates, styrenes and acrylamides.[68,69,86,87] SP monomers were employed for the controlled polymerization techniques such as NMP[74] and ATRP.[59,88]

Reports of RAFT copolymerization of SP monomers demonstrate their use as acrylates[73,75] and methacrylates.[56,72,76,82,89–92] However, these reports often demonstrate a low SP content[56,72,76,82,89,90,92] and relatively high dispersities[76,89] (Đ $\gtrsim$ 1.4). A possible explanation for this is the influence of steric hindrance due the relatively large SP monomer. In reports showing better control (Đ ($\lesssim$ 1.3) and SP methacrylate block lengths up to 100, a long spacer was introduced between the polymerizing methacrylate group and the photo-switchable SP moiety.[73,91] However, compared to a typical RAFT polymerization, these report used rather high amounts of radical initiator or only achieved conversions of about 50-70%.

Although the different physiochemical properties of SP and MC are well known, to my best knowledge, the influence of the different isomers on the radical polymerization has hardly been studied. Only Ziółkowski et al. propose the inhibition of an UV initiated photopolymerization by the MC isomer.[86]

1.6.2   Programmable Friction

Developed switchable materials demonstrate the current application potential for programmable friction systems to reduce heat and wear losses (see Chapter 1.1 and 1.2). The reported systems can be classified according to various criteria, such as the external trigger, the material system, the operating principle and others. The following chapter describes and categorizes known systems, which follow a similar approach as the materials in focus of this thesis (see chapters 2-4). Accordingly, the first Subchapter 1.6.1.2 addresses systems that change their frictional behavior under the influence of light. The second Subchapter 1.6.1.2 discusses responsive polymer brushes that permit programmable lubrication under the influence of various external stimuli. To the best of my knowledge, light-programmable polymer brushes, which according to the categorization would fit into both chapters, have not been described yet. However, it is anticipated that such systems could be designed. This work aims to develop a concrete proposal for this. Accordingly, Chapter 2.2 describes the concept and advantages of light-programmable polymer brushes.

1.6.2.1   Light-Programmable Friction

The application of light has many practical advantages for the design of a programmable friction system (Chapter 1.2). In this regard, Chapter 1.6.1 introduced the most common chemical moieties applied in the design of light-programmable materials. In this chapter, an overview of the reported systems that enable light-programmable friction is given by categorizing them according to their working principle (Scheme 6). Material with programmable friction can change the nature of the surface, as shown by examples in the following Chapter 1.6.2.1.1. Furthermore, the viscosity of a lubricant can be switchable, as the literature reports in Chapter 1.6.2.1.2 show.
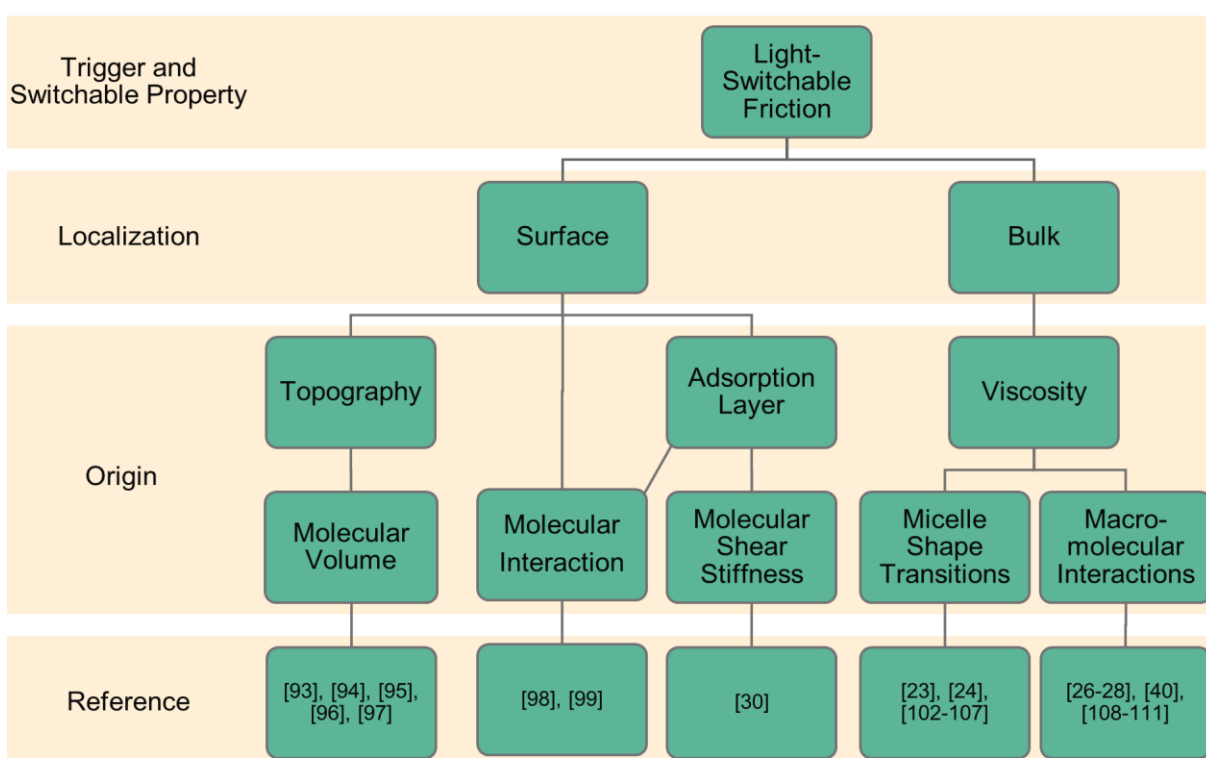
Scheme 6:   Overview on published systems that allow the reversible alteration of friction properties by light as external trigger.

1.6.2.1.1 Light-Switchable Surfaces

One concept of light-programmable friction in the literature is the light-induced change in surface topography. Liu, Broer et al. developed photo-responsive liquid crystal polymer coatings that enable a dynamic modulation of surface topography on a scale of about one micrometer.[93] Azobenzene crosslinkers permit a change of the chiral nematic order to facilitate directional stretching upon UV radiation (Scheme 7A). The structure of the switchable fingerprint textures depends on the surface treatment and spincoating conditions. The paper demonstrates how objects are held and released by the light-triggered emergence of the surface features within seconds.[94] The lower friction coefficient of the fingerprint structure compared to the flat surface is attributed to the reduced surface contact area. Appropriate surface patterning permits the fabrication of other topologies, which exhibit anisotropic properties. A friction pair composed of two surfaces, each with parallel lines of light-switchable features, exhibits angular-dependent friction (Scheme 7B). The discrepancy in the coefficient of friction before and after UV radiation depends on the relative orientation of the stripes of each sample and the direction of motion. In addition to the negative, light-induced changes in the coefficient of friction already mentioned, positive changes are also possible, as they occur in the case of orthogonal motion of a friction pair with an almost parallel oriented surface pattern. This is explained by interlocking effects.[95] A recent study of a liquid crystal polymer coating even demonstrates the targeted light-driven expansion of the polymer to perform a wave-like motion on the surface of the material. This highlights the high temporal and spatial resolution of the programming process and the fascinating possibilities of this light-programmable material.[96]

Xue et al. demonstrated light-switchable friction between an AFM tip and self-assembled azobenzene layers on a pyrolytic graphite substrate (Scheme 7C).[97] STM and the calculated adsorption energy of a DFT simulation model indicate light-triggered structural changes of the azobenzene layer. The system shows no fatigue after 12 photoprogramming cycles.

Another approach for the modulation of friction between surfaces is light-switchable attractive interactions between the molecules of the two shearing surfaces. Blass et al. demonstrated the light-responsive alteration of friction and adhesion forces between a functionalized AFM tip and a silicon wafer (Scheme 7D).[98] Both surfaces of the friction pair were equipped with immobilized β-cyclodextrine moieties that can be dynamically linked by a small guest molecule containing two azobenzene functions. The trans-isomer complexes with the CD-cavities of both surfaces and, dynamically linking them upon VIS radiation, whereas UV radiation shifts the isomerization equilibrium to the cis-isomer suppressing the complexation by steric

hindrance. Consequently, this paper shows higher friction of the described system during VIS radiation.
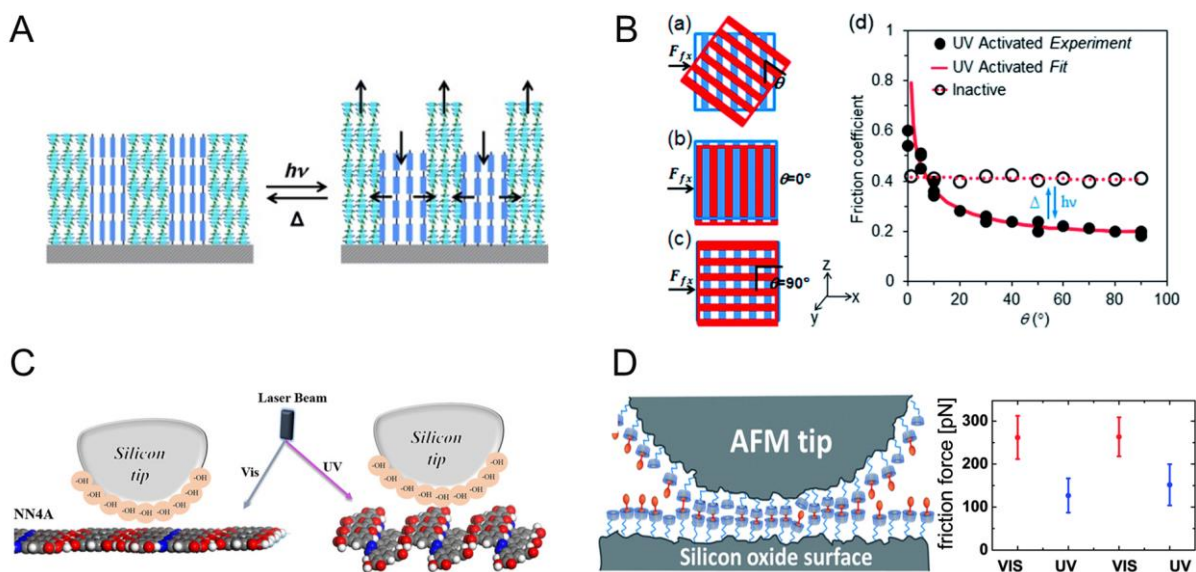
Scheme 7: *Examples of reported surfaces systems featuring light-switchable friction.*
(A) Azobenzene containing liquid-crystal polymer coating with chiral nematic areas stretch upon UV exposure. Reprinted from ref[93] with permission from John Wiley & Sons https://doi.org/10.1002/anie.201105101 (22.11.21). Copyright © 2012 WILEY-VCH Verlag.
(B) Angular-dependent friction force between a friction pair with two surfaces of parallel oriented light-switchable polymer features. Reprinted from ref[95] with permission from the Royal Society of Chemistry. https://doi.org/10.1039/C4SM01249F (22.11.21). Copyright © 2014 Royal Society of Chemistry.
(C) Scheme of configural changes of self-assembled azobenzene layer under influence of light in an AFM setup. Reprinted from ref[97] with permission https://doi.org/10.3389/fchem.2021.707232 (23.11.21). Copyright © 2021 Xue, Ma, Tian, Zeng, Tu, Luo, Wen and Luo.
(D) AFM-measurement of light-switchable dynamic complexation between surfaces with β-CD cavaties and an bifunctional azobenzene guest molecule. Reprinted from ref [98] with permission from the Royal Society of Chemistry. https://doi.org/10.1039/C4CC09204J (23.11.21). Copyright © 2015 Royal Society of Chemistry.

Recently, Perotti et al. reported the switchable friction between a TiO_2 surface and AFM tips under the influence of UV light.[99] According to ab initio simulations of TiO_2 surfaces, which show lower atomic orbital overlapping during UV exposure, the authors suggest quantum effects as origin of the phototribological behavior.

Tang et al. reported photo-switchable friction between a steel ball and a silica surface lubricated by solutions containing a small diarylethene derivatives.[30] Since the diarylethene solutions only show negligible viscosity changes upon radiation, the authors suggest adsorbed layers of the photo-switchable diarylethene molecules in the nanoconfinement between the surfaces responsible for the light-induced friction control. Simulations estimate different molecular shear stiffness of the diarylethene isomers and therefore support this explanation. Nevertheless, the work shows only small changes of the coefficient of friction.

Unfortunately, hard surfaces in frictional contact are prone to abrasion over time, which would lead to a gradual decline in the switchable friction properties of such systems. Other drawbacks compromising practical relevance of the presented literature examples are the relatively small changes in the friction coefficient upon the switching (usually less than an one order of magnitude). Furthermore, most of systems were evaluated in highly experimental laboratory setups like AFM and have thus not been tested in technologically relevant friction scenarios, for example, with lubricated technically relevant materials whose surface exhibit a certain roughness.

1.6.2.1.2 Photo-Responsive Fluids

Section 1.2 and Scheme 5B described that the coefficient of friction of a lubricated friction system depends on the viscosity of the lubricant. Accordingly, light-switchable viscosity can provide dynamic friction control. This chapter describes examples and basic operating mechanisms for fluids that can change their viscosity under the influence of light.

One class of light-responsive fluids are micellar systems. Typically, surfactant solutions form dynamic colloidal aggregates above the critical micelle concentration,[100] and a dynamic network with entangled wormlike morphology above a certain overlapping concentration.[101] The threshold value of these characteristic concentrations also depends on other parameters such as the chemical structure of the surfactants. Consequently, micelles containing light-responsive dopents or building blocks such as anthracenes[102], azobenzenes[24,23,103,104,105] or SP[106] allow reversible aggregation or morphological transitions, for example, between globular, cylindrical and worm-like structures under light radiation. Another type of micellular rearrangement proposed by Dong et al. is the variation of junction density within a micellular network formed by amphiphilic, telechelic and SP-terminated polymers.[107] Transition between all the described micelle structures can be accompanied by a change in rheological properties. Remarkably, for example, zero shear viscosity changes up to six orders of magnitude have been achieved with transitions of worm-like micelles.[103]

Another class of responsive viscosity modifiers are functional polymer solutions. The viscosity of a polymer solution depends on, inter alia, the molar mass, the polymer architecture and the solvent quality. Light-assisted interactions between polymer chains such as physical attraction or covalent links permit the alteration of these parameters and thus enable highly customized light-switchable rheological properties. This is reported for various polymer systems, for example, functional polymers that carry azobenzenes,[26,108] azobenzenes combined with complexing β-CD cavities,[27,28,109] SP,[110] coumarines[111] or anthracenes.[40]

Depending on the individual friction system of a potential technical application, the photo-responsive fluids described in this chapter may have certain disadvantages. For example, all mentioned systems are solvent-based, which means that depending on the solvent, volatility, toxicity, flammability, corrosion, or incompatibility with the friction pair material may be an issue. Furthermore, systems whose rheological properties are strongly influenced by dynamic, physical interactions are not expected to withstand high forces, which is important in many technical applications. For instance, wormlike micelles show pronounced shear-thinning[103,104] leading to significantly lower switchable viscosities at high shear stress.

1.6.2.2   Grafted Polymer Brushes

Lubrication with immobilized macromolecules is a well-established principle found in nature.[112] Compared to the friction of typical lubricants, which is described by the Stribeck-curve (see Chapter 1.2 and Scheme 1B), immobilized macromolecules show the great advantage of low and almost shear velocity independent friction forces at low sliding speeds.[113] The origin of this frictional behavior is explained by the osmotic pressure repulsion between the polymer brushes of both surfaces.[114] Accordingly, good polymer compatibility with the medium as well as high polymer densities are desired to accomplish a good tribological performance and reduce wear.[115] The variety of polymer classes such as hydrophilic neutral, polyionic, hydrophobic, or fluorinated makes it possible to find an individually suitable brushes system for different friction systems. For example, zwitterionic polymers are known for their exceptional lubricating performance in water-lubricated systems, as they exhibit high hydration and are insensitive to other environmental effects such as salts or pH.[116]

While Chapter 1.5 gives an overview of synthetic strategies for the preparation of graft polymer surfaces, this chapter deals with the programming of friction in polymer brushes, specifically addressing different stimuli. The implementation of programmability to the friction of polymer brush systems usually relies on the alteration of the polymer configuration triggered by responsive building blocks (Scheme 8). Switchable adhesion and friction of stimuli-responsive polymer coatings including polymer brushes have recently been reviewed by Yu et al.[117] In the following, a selection will exemplify the state of art.

High Friction   Low Friction
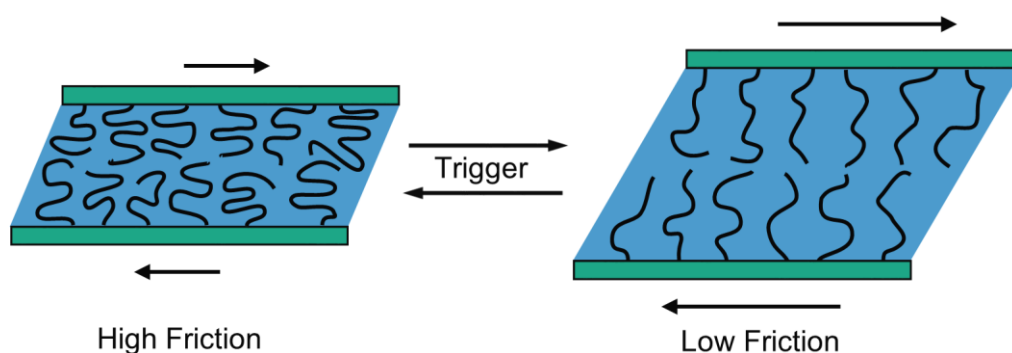
Scheme 8:   *Programming the friction between stimuli-responsive polymer brushes surfaces. Known triggers are temperature,[118,119] solvent,[120] ions,[121] pH[121] and an electric field.[122]*

One class of responsive polymers changes its configuration upon temperature changes, which can also be used to switch the friction properties. Chang et al. measured temperature dependent adhesion force between a PNIPAM gel and an AFM tip modified with PNIPAM brushes.[118] The paper examines the tribological effects of the thermally induced phase transition. A higher friction coefficient was measured in the case of the collapsed polymer and six programming cycles showed good reversibility of the process. Interestingly, Yu et al.

reported a friction and adhesion force maximum around the LCST between a gold colloid and PNIPAM brushes.[119] The brushes stretch due to long-range adhesive interactions, leading to an enhanced dissipative response of the polymer. However, the switching time of friction by temperature is limited by the heating and cooling rate of the system. In addition, the trigger does not allow spatial resolution as the heat is usually distributed in the system. In general, temperature as an external stimulus is considered to be of limited practicality for technical friction applications, since the friction process itself usually develops heat.

Another type of external signal that affects the polymer configuration and thus the friction of the polymer brushes can be chemical stimuli. Yu et al. demonstrate the solvent composition to influence the friction on PNIPAM brushes. Low friction is observed in case of the good and pure solvents water and ethanol. PNIPAM brushes in mixtures of both solvents, however, exhibit a co-non-solvency effect leading to local friction force maxima over the course of solvent composition.[120] Wei et al. show an extraordinary modulation of the friction coefficient by more than two orders of magnitude for multi-responsive polyelectrolyte brushes.[121] The polycationic brushes dehydrate and collapse, thus increasing the friction coefficient, in the presence of a series of counterions with increasing binding affinity. Similarly, polyanionic polymer brushes respond in the presence of quaternary ammonium or multivalent metal ions. Finally, the paper demonstrated that the friction of protonable PMAA brushes altered reversibly by pH changes over nine programming cycles. In contrast, zwitterionic polymer brushes changed their friction behavior only slightly in different counterion solutions.

Similar to the previously mentioned drawback of temperature switching, chemical stimuli do not allow spatial resolution and their switching time is associated with the rather slow action of the stimulus itself, in this case change of the chemical environment. Replacing a component of the friction system is a laborious as well as resource-inefficient process that is considered impractical for engineering applications. The reaction to certain chemical stimuli, such as metals, can also be unfavorable for applications where metal parts are subject to wear.

Zheng et al. demonstrate external electric fields as stimulus for programming of the friction performance of polyelectrolyte polymer brushes.[122] The charged side groups of the polymer, grafted onto an electrically conductive substrate, induce a collapse or stretching of the polymer according to the surface charge of the substrate. The kinetic friction factor is demonstrated to decrease or increase, respectively. The system works in polar as well as non-polar media. However, this concept is limited to conductive materials and requires the integration of electrical components to the surface.

2. Objective

Functional materials that enable the real-time adjustment of the frictional behavior of a mechanical component hold enormous potential for saving energy and improving the performance of established friction systems (see Chapter 1.1 and 1.2). A promising approach to realize this concept is the implementation of light-switchable materials, since light is readily available, cheap and simple to apply. Regulation of intensity, wavelength, exposure time and the use of optical equipment permit accurate spatiotemporal control of the trigger. This contribution on the development of novel photo-responsive polymers aims to advance their suitability for the alteration of friction properties. Photo-reactive moieties, highlighted in Chapter 1.6.1 translate an external light signal into switchable physiochemical properties. Consequently, the integration of a selected photo-responsive unit into a polymer material is anticipated to merge the responsive function with the basic friction behavior of a particular polymer material. This thesis focusses on the development of two novel respective polymer materials. In the first part, anthracene-functionalized silicon oils are investigated as programmable lubricants. The second part of the thesis deals with the synthesis and properties of spiropyran graft copolymers (SP) as switchable surfaces. For each part, a more detailed description of the objectives is given the following two Subsections 2.1 and 2.2.

2.1 Tunable Viscosity of Anthracene-Terminated Silicone Oils

Programmable lubricants permit the flattening of the Stribeck curve and thus the reduction of wear and heat losses as previously described in Chapter 1.2. The state of art deals with many solvent-based systems (Chapter 1.6.2.1.2), which, however, may limit the technical applicability due to corrosion, flammability, fugacity or lacking material compatibility. In this work, novel fluids based on polydimethylsiloxanes (PDMS) are investigated as light-programmable lubricants. This system is solvent-free. Additionally, it takes advantage of the good UV and VIS transparency of PDMS. PDMS is shear stable, non-toxic and chemically inert even at higher temperatures. It has a relatively low viscosity index and a pouring point between -40 and -70 °C.[123] Accordingly, PDMS meets the demands of technical oils and is particularly interesting for low-temperature applications. Other important properties include good dielectric stability, high compressibility, and low surface tension, which complement the previous characteristics and enable application potential of PDMS fluids as dielectrics, hydraulic and damping fluids, antifoams, lubricants, heat transfer fluids, and diffusion pump oils.[124]

The aim of this work is to synthesize linear PDMS chains with 9-anthracene-ester-termini by an esterification of hydroxyalkyl-terminated PDMS precursors (Scheme 9). The photo-responsive anthracene ester enables the formation of new links between polymer chains upon UV-A exposure. The resultant anthracene dimers increase the molar mass of the polymer chains and thus influence the rheological properties of the melt. The cycloreversion is achieved by UV-C or heat treatment and permits to reprogram of the rheological properties of the material.

The main objective of this study is to analyze the achievable rheological properties during in-situ programming of synthesized anthracene-terminated silicones (Chapter 3.1.1). For this purpose, various structural parameter such degree of functionalization (DoF), number of termini, degree of dimerization (DoD) and their influence on the reachable viscoelastic properties are investigated. The programming and rheological measurements, which are conducted in a few hundred micron wide rheometer gap, aim to give first insight into the applicability of the material as thin lubricating films. A sufficiently homogeneous material programming is desired to realize uniform material behavior. Therefore, different mixing conditions have to be tested. Another goal is to compare the reprogrammability of the rheological properties with different stimuli. For this purpose, photochemical and thermal

reversion will be explored. In this context, cyclic reprogramming also serves to reveal important long-term phenomena such as programming fatigue and photooxidative stability.
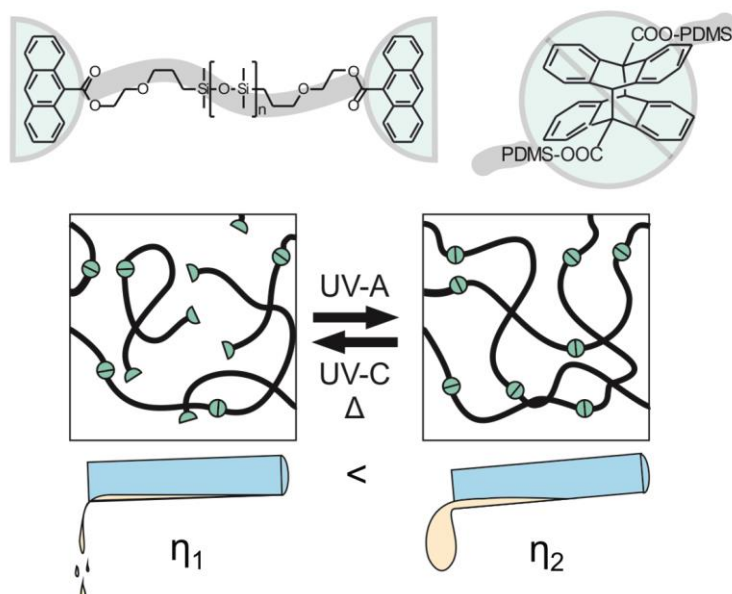
Scheme 9: Concept of light-switchable viscosity with bis(9-anthracene ester)-terminated PDMS. Reproduced in part permission from ref.[125] https://doi.org/10.1021/acsapm.0c00794. (22.11.21) © 2020 American Chemical Society.

The second part discusses formulations of the synthesized programmable lubricants (Chapter 3.1.2). The blending of a functional component with a standard oil is a popular concept in product development to customize particular properties of a product in a cost-efficient way. Following this approach, PDMS blends are also investigated in this thesis to evaluate the practicality of anthracene functionalized PDMS as an additive. Phase compatibility and the programming range of rheological properties, taking into account various parameters such as molar mass and weight fraction, are the focus of the work.

2.2 Light-Responsive Friction by Grafted Spiropyran Copolymers

The second approach of this thesis addresses the potential of light-tunable surfaces to improve friction, for example in micro-actuators (Chapter 1.2.). The strategy applied involves the implementation of photoswitchability in the nature-inspired principle of using polymer brush surfaces for lubrication.[112] A particular advantage of polymer brushes is that they enable low coefficients of friction even at the lowest shear rates.[113] So far, studies on the programmable friction of polymer brushes had only focused on other stimuli such as temperature, pH, ions or an external electric field (Chapter 1.6.2.2). However, these stimuli have individual disadvantages, such as slow switching times, no possibility of spatial programming or high effort of implementation.

In contrast, light is an alternative stimulus that unites aforementioned advantages (Chapter 2). The objective of this work is to develop light-switchable grafted polymer surfaces for the purpose of programmable friction. The concept is illustrated in Scheme 10. The copolymer consists mainly of a hydrophilic monomer, which is intended to promote swelling in a polar, environmentally friendly solvent such as water or DMSO. The minor comonomer contains the functional SP unit, which is aimed to introduce light-responsiveness to the system. The SP copolymer is designed to change the affinity to a solvent by light, thus undergoing a change of the configuration. As a result, the polymer swelling is expected to alter the frictional properties (Chapter 1.6.2.2).

RAFT polymerization is suitable for the synthesis of polymer brushes by the grafting-from approach (Chapter 1.5). However, literature reports indicate certain implications for the RAFT copolymerization of SP, as mostly only polymers with small contents of SP are reported and often higher dispersities were obtained (Chapter 1.6.1.2). These issues are addressed by performing a stepwise synthesis optimization up to the desired SPA copolymer brushes. An initial investigation into the solution polymerization of spiropyran acrylate (SPA) with the polar monomer 2-hydroxyethyl acrylate (HEA) in Chapter 3.2.1 intends to gain insight into the conditions required for the copolymerization of SPA. It evaluates the potential influence of the light-responsiveness and different monomer ratios on the polymerization. In the subsequent experiments, the optimized method is applied for the actually desired synthesis of polymer brushes. In this, the synthesis procedure is further developed to finally obtain grafted SP copolymers (Chapter 3.2.2). Finally, the analysis of the surface properties of the grafted copolymers attempts to evaluate the light-switchability and its dependence on the SPA content of the copolymer (Section 3.2.2.2.2).
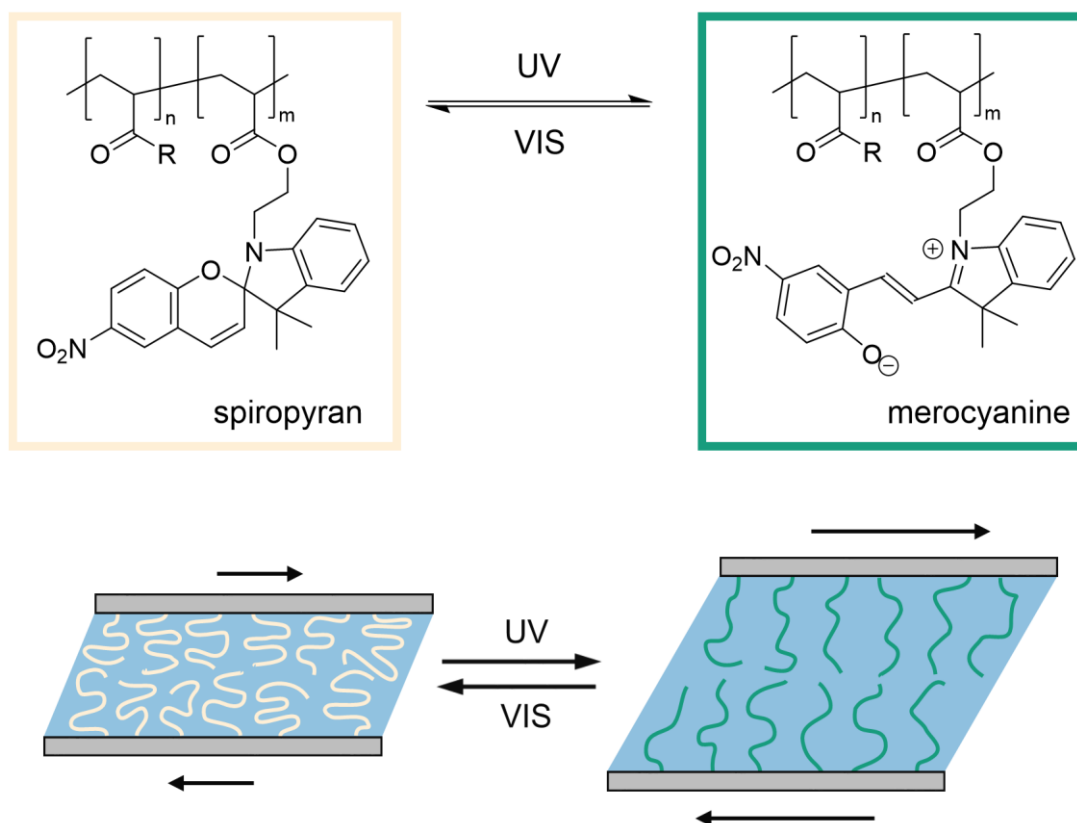
Scheme 10:   *Concept of light-switchable frictional behavior by configuration changes of grafted light-switchable spiropyran copolymers.*

3. Results and Discussion

3.1 Anthracene-Terminated Silicones

3.1.1 Mono- and Bifunctional PDMS

3.1.1.1 Synthesis and Dimerization

The development of programmable oils for technical applications demands an easy and cost-efficient synthesis route. Accordingly, 9-anthracene ester-terminated polydimethylsiloxanes (PDMS-As) were synthesized by a simple one-step modification of commercially available hydroxyalkyl-terminated PDMS (Scheme 11). Monofunctional PDMS-A$_1$, bifunctional PDMS-A$_2$ and their mixtures already cover a large part of the scope of programmable properties, as the average number of anthracene groups per chain determines the programming range. While PDMS-A$_1$ can only dimerize due to the absence of a second anthracene ester-functionalized chain end, PDMS-A$_2$ can theoretically undergo unlimited chain extension following the rules of a step-growth polymerization. In this regard, the programming effect should be much more pronounced for PDMS-A$_2$ than for PDMS-A$_1$. A complete functionalization with anthracene esters is desired in any case to maximize the range of programmability.
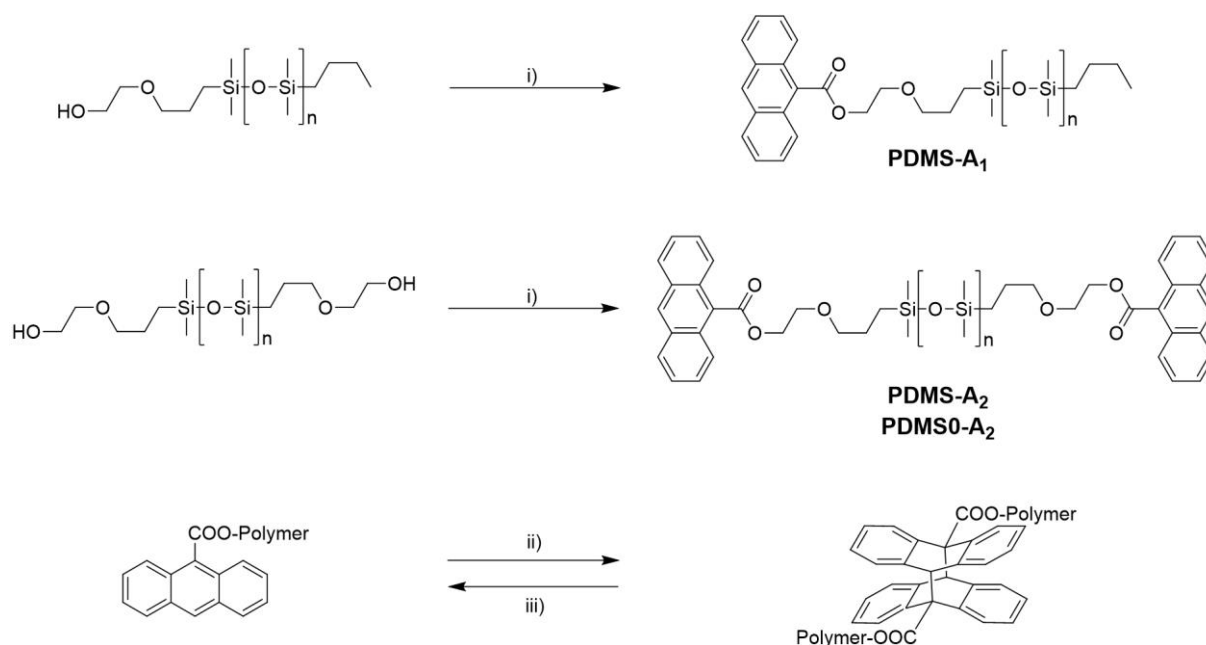
Scheme 11: *Synthesis (top, mid) and light-triggered coupling (bottom) of anthracene-functionalized linear PDMS chains. i) 9-Anthracenecarbonyl chloride, CHCl$_3$, 20 h, 60 °C; ii) UV-A (λ = 365 nm) and iii) UV-C(λ = 254 nm) or heat.*
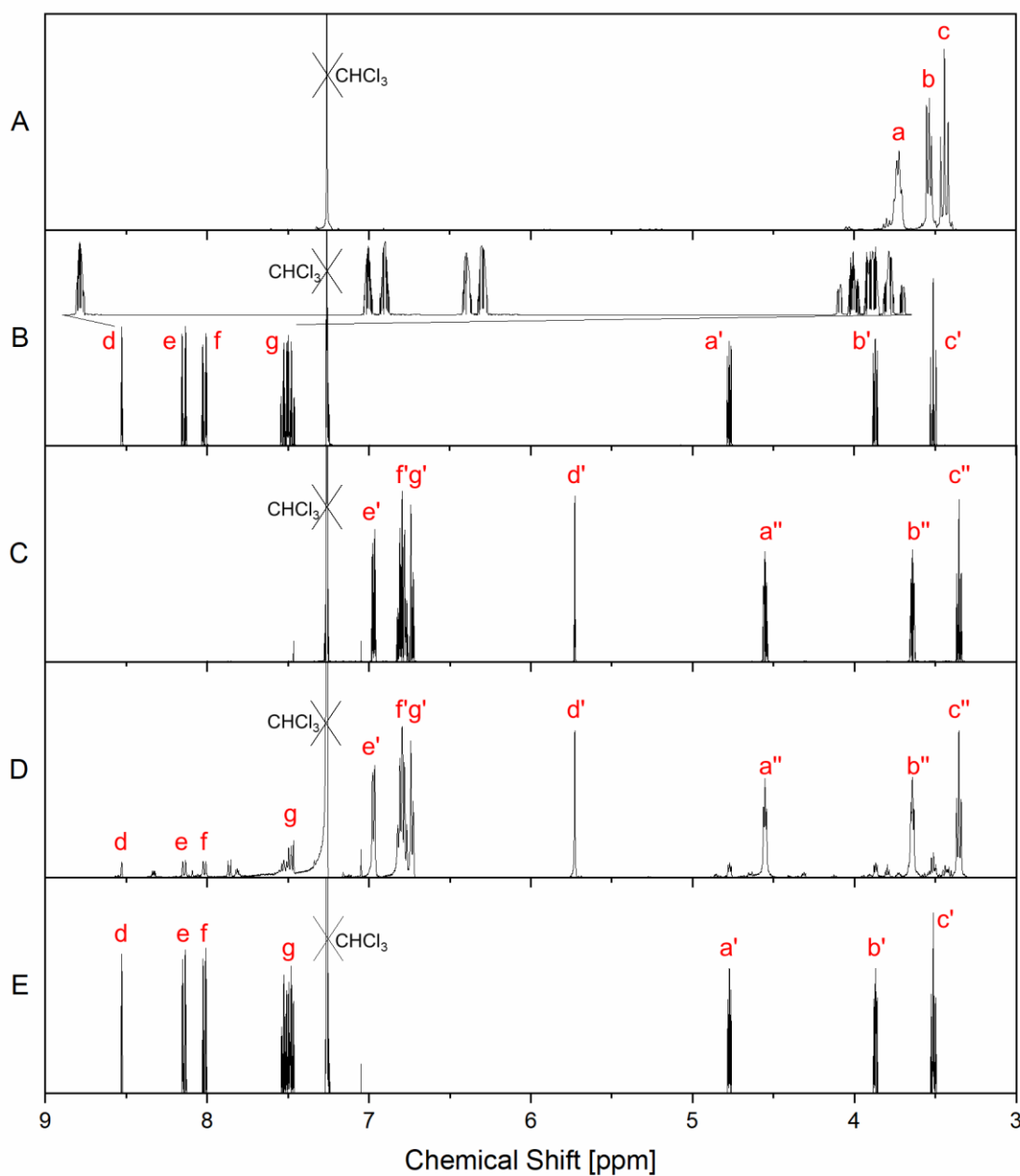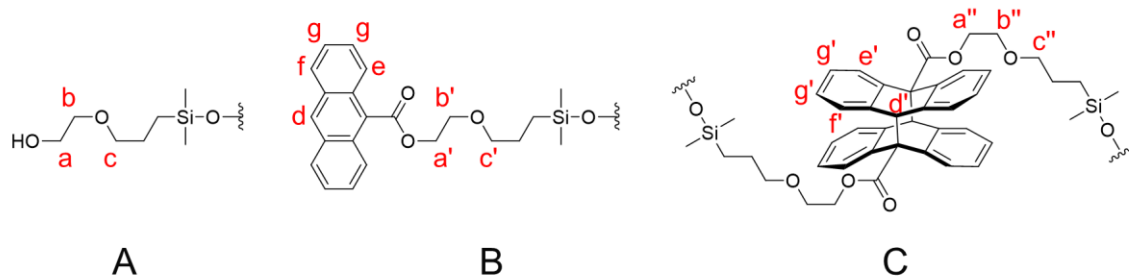
Figure 2: *¹H-NMR spectra of hydroxyalkyl-terminated PDMS (A) and 9-anthracencarboxylic acid ester-terminated PDMS before (B) and after (C) UV-A radiation and either after subsequent UV-C (D) or heat (E) treatment.*

The esterification of hydroxyalkyl-termini was performed using 9-anthracenecarbonyl chloride in an acidic condition and typically yielded to a degree of functionalization DoF ≥ 94 % as calculated by Equation (12) using NMR spectroscopy (Figure 2). The synthesis using stoichiometric amounts of pyridine base in pre-experiments only yielded low functionalization ratios. While esterification reactions of acid chlorides and alcohols are usually carried out under basic conditions, 9-anthracenecarbonyl chloride reacts poorly in the presence of tertiary amines such as pyridine or trimethyl amine.[126] Previous studies also report incomplete esterifications of only 87.4 % for 9-anthracenecarboxylic acid using N,N'-diisopropyl carbodiimide, 1-(3-(dimethylamino)propyl)-3-ethylcarbodiimide, or bis(2-oxo-3-oxazolidinyl)-phosphinic chloride as a coupling reagent.[50]

The radiation of sessile PDMS-A_2 drops, followed by the subsequent analysis of the material by ^{1}H-NMR spectroscopy gives information on the conversion of anthracene groups into the respective dimers (Scheme 11). Successful dimerization was found after UV-A radiation (Figure 2). Relevant signals attributed to aromatic and adjacent methylene protons shift upfield due to the reduced aromatic conjugation length. The singlet peak at 5.73 ppm is assigned to the bridgehead protons and indicates the formation of head-to-tail conformers. Sterically unfavored head-to-head conformers are not observed. A maximum degree of dimerization (DoD) of 95 % is found after radiation with UV-A as estimated using Equation (13) (Figure 3). The maximum conversion to dimers is connected to the programming range as it determines the upper limit of a viscosity increase. However, a complete conversion is not expected for PDMS-As. With increasing DoD, the material becomes so viscous that the mobility of the terminal end groups is restricted. At the same time, the concentration of unreacted anthracene end groups decreases. Consequently, the probability of two anthracene moieties meeting one another decreases to an extent that the reaction comes to a halt at some point. Subsequent UV-C radiation cleaves anthracene dimers to a certain extent reaching a minimum DoD of 88 % (Figure 3). In fact, the exposure of anthracene esters and their dimers to UV-C light promotes cleavage and dimerization simultaneously, leading to the establishment of a quasistationary equilibrium.[51]

$$DoF = \frac{\dfrac{I^d + I^e + I^f + I^g + I^{a\prime} + I^{b\prime}}{13}}{\dfrac{I^d + I^e + I^f + I^g + I^{a\prime} + I^{b\prime}}{13} + \dfrac{I^a + I^c}{4}} \qquad (12)$$

$$DoD = \frac{I^d + I^e + I^f + I^g}{(I^d + I^e + I^f + I^g) + (I^{e\prime} + I^{fg\prime} + I^{d\prime})} \qquad (13)$$
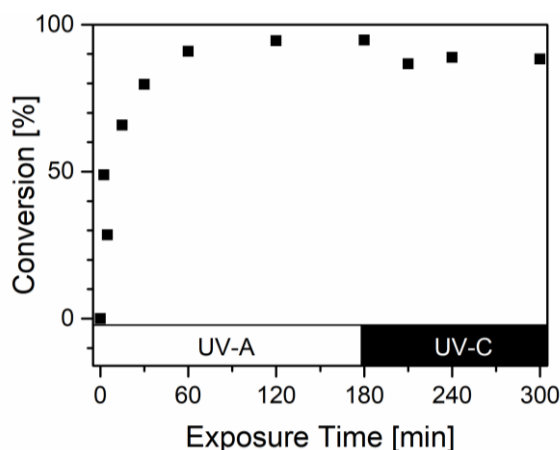
Figure 3:   The conversion of PDMS-A_2 to anthracene dimer extended PDMS during the exposure to UV-A and UV-C light analyzed by ^{1}H-NMR spectroscopy.

Full reversibility is only achieved by thermally induced cycloreversion. PDMS-A_2 shows no significant decline of reversibility after 10 cycles of photochemical programming when the exposure time in total is limited to a few hours, as indicated by the relative change of peak height at $\lambda_{max} = 362$ nm using UV/VIS spectroscopy (Figure 4). This result is in accordance with an earlier report on an anthracene-terminated eight-arm PEG-based polymer.[50] Prolonged exposure to UV light, however, does have an impact on the structural integrity, as also observed in the following Section 3.1.1.2 and discussed in detail in Section 3.1.1.3.
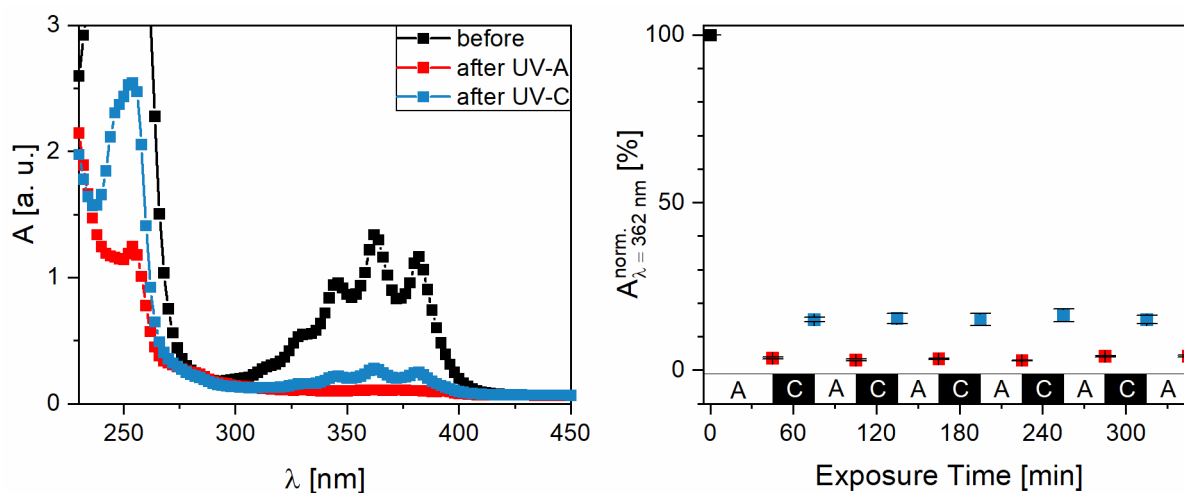
Figure 4:   UV/VIS spectra of PDMS-A_2 before and after subsequent UV-A and UV-C radiation.

In summary, anthracene ester-terminated PDMS are obtained and dimerize, both with high conversions. The kinetics and the effective extent of cycloaddition/cycloreversion of PDMS-bound anthracenes have a huge impact on the performance of the material as a programmable lubricant. At the same time, they depend on many experimental parameters, such as light intensity, sample geometry, the concentration of functional groups, mobility of the chain

termini, and mixing conditions. Consequently, these aspects have to be assessed, which is part of the following section.

3.1.1.2   Rheological Properties

3.1.1.2.1 Photochemical Programming

The dimerization and cleavage between chain ends of PDMS-As is demonstrated and quantified in the previous section. These reactions are the key to switch the molar mass and consequently program the viscoelastic properties of the polymer melt. The alteration of viscoelastic properties is analyzed under oscillatory shear and in the presence of UV light. The influence of mechanically induced chain degradation is excluded in all experiments by performing frequency sweeps (not shown) and control experiments without UV radiation but with otherwise unaltered conditions (Figure 6, right). The used rheometer setup allowed the characterization of oil films in plate-plate geometry while UV radiation was enabled from the top (Scheme 12). Notwithstanding, the evolution of a viscosity gradient within the film may
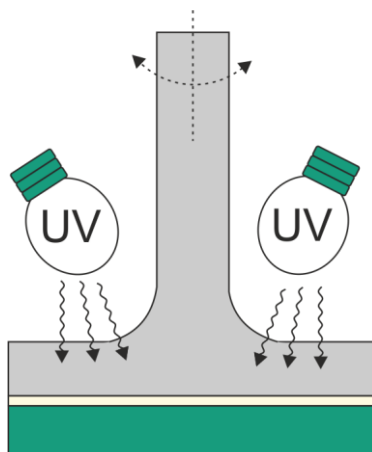
Scheme 12:   *The rheological properties of a silicone oil film analyzed by a rheometer in plate-plate geometry. The UV-transparent upper plate and shaft, which are made of quartz glass, enabled in-situ radiation from above.*

occur during our measurements since the oil layer between the plates attenuates the incoming light beam. PDMS-A_2 possesses local absorption maxima at 254 and 365 nm, the latter being lower than the first one. After dimerization, the absorption band in the UV-A region disappears while the absorption observed in the UV-C region only diminishes (Figure 4, left). Consequently, stronger intensity attenuation along the light path is expected for UV-C radiation. This issue was tackled by repetitive intermediate mixing periods in which the plates constantly rotate at a given shear rate between the oscillatory shear modes. The applied mixing procedure maintains the homogeneity of the sample. Different mixing conditions, however, lead to different programming kinetics, as displayed in Figure 5. In the first experiment, the shear rate $\dot{\gamma}$ was comparatively low at 50 s^{-1} during all intermediate mixing steps. In the second experiment, it initially started at a higher value of 500 s^{-1} and decreased it stepwise to 50 s^{-1},

as marked by four time blocks. During the programming process, the viscous properties dominate in both experiments (i.e., G'' > G'), and the initial loss modulus of 1.87 ± 0.07 Pa increases by approximately 2 orders of magnitude until it finally levels off. Different maxima of loss moduli (142 and 223 Pa) are reached in dependence on the applied mixing conditions. Although storage moduli G' increase at least two decades up to 7.0 and 13.4 Pa, the full range cannot be quantified precisely due to the initial absence of significant elastic behavior. In the case of the initially faster mixing, an accelerated increase of moduli is observed as represented by the higher slopes that level off earlier to reach a maximum for the respective moduli.
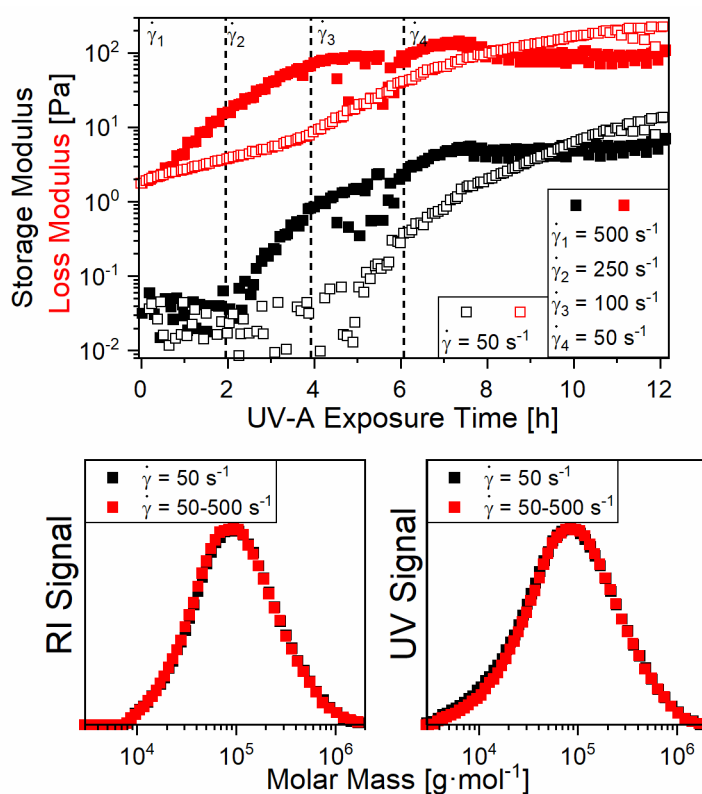
Figure 5:   *Influence of constant* $(\dot{\gamma} = 50\ s^{-1})$ *and stepwise decreasing shear rates* $(\dot{\gamma} = 500/250/100/50\ s^{-1})$ *during the intermediate mixing steps on the evolution of storage and loss moduli of PDMS-A_2 in the presence of UV-A light and SEC traces of the silicon oil after the experiment.*

For the dynamic mixing protocol, the detachment appears in the $\dot{\gamma}_3$ block and after 7 h in the $\dot{\gamma}_4$ block, while for the slow mixing, the same effect only appears after 11 h (Figure 5). The occurrence of the detachment issue is linked to a minimum level of viscosity. Since a sufficiently high viscosity is reached earlier for the dynamic mixing protocol, the detachment occurs earlier. It is noted, however, that the detachment occurs spontaneously, meaning that the exact moment at which the detachment occurs is rather unpredictable. During a detachment period, the contact between oil and plate is slowly restored each time during the respective recording of dynamic moduli after the mixing step. Restoration, however, does not

seem to occur to a full extent within the applied time frame of the oscillation measurement. Thus, detected values remain underestimated, meaning that the detachment phenomenon renders an exact comparison of the maxima for the different mixing protocols nonsignificant. Yet, the reduction of the mixing speed at high viscosity aids to prevent the contact loss between sample and plate and further avoids slippage of the mounted upper quartz glass plate, which is necessary to measure reliable moduli in the oscillatory experiment. The dependence of dynamic moduli on the mixing conditions is explained by the following reason. The mechanical response of a sample, which is heterogeneous in the orthogonal dimension with respect to the deformation, is mainly influenced by the part with the lowest resistance. Homogenization by rotational shear consequently leads to a faster increase of observed moduli. However, with a low shear rate, mixing occurs too and the values of moduli eventually catch up to the ones observed for the dynamic mixing, in fact, even exceeding them in the end. Substantial differences in molar mass distribution are not the cause for these final differences, as evidenced by SEC measurements after applying the two different mixing protocols (Figure 5). The only reasonable explanation therefore is remaining structural inhomogeneities within the material hosting gap of the rheometer.

The evolution of dynamic moduli as well as the dynamic viscosity of PDMS-A$_2$ was plotted as a function of the conversion (DoD) of the anthracene ester units (Equation (13), Figure 6, left). First, moduli and viscosity increase only moderately up to conversions of around 80 %. Only after that, by reaching conversions higher than 90 %, a strong increase in the values is observed. This is in good agreement with the expectation of for this polyaddition-type reaction.
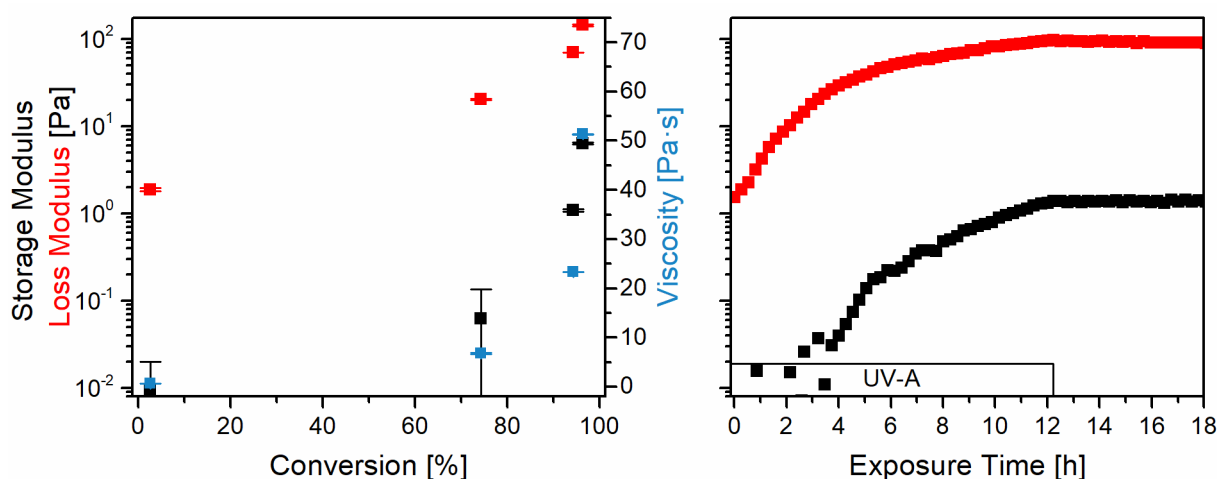
Figure 6: *Evolution of the storage modulus, the loss modulus and the dynamic viscosity of PDMS-A$_2$ as a function of conversion of the anthracene ester termini into dimers during radiation with UV-A light (left) and of the dynamic moduli during and after exposure to UV-A (right).*

As expressed by the Carothers' Equation (14), high coupling degrees are only reachable with high conversion of the reactive chain ends.

$\bar{X}_n$ represents the number average degree of coupling and ρ the conversion of the anthracene ester groups (DoD). At 50 % conversion, the average coupling degree is settled at only 2, at 80 % at 5, and at 90 % at 10. Consequently, strong changes in the rheological properties of PDMS-A$_2$ are only observed at high conversions of the dimerization reaction.

$$\bar{X}_n \ = \ \frac{1}{1-\rho} \tag{14}$$

In the next step, dynamic moduli were measured over four cycles of alternating UV-A and UV-C radiation, and zero shear viscosities were determined after each illumination period to study the programming of material properties with respect to its reversibility (Figure 7). Again, the first period of UV-A exposure leads to a significant increase in dynamic moduli. As confirmed by SEC measurements, this is indeed the result of a strongly increased molar mass (Figure 9) as a consequence of the chain extension process upon dimerization of the anthracene ester termini. With the strong increase in molar mass, the question arises whether entanglements start to have an influence on the overall mechanical properties of the material and on the reactivity of the light-responsive chain ends. As shown in Figure 8, however, the loss modulus is always higher than the storage modulus while no plateau modulus is
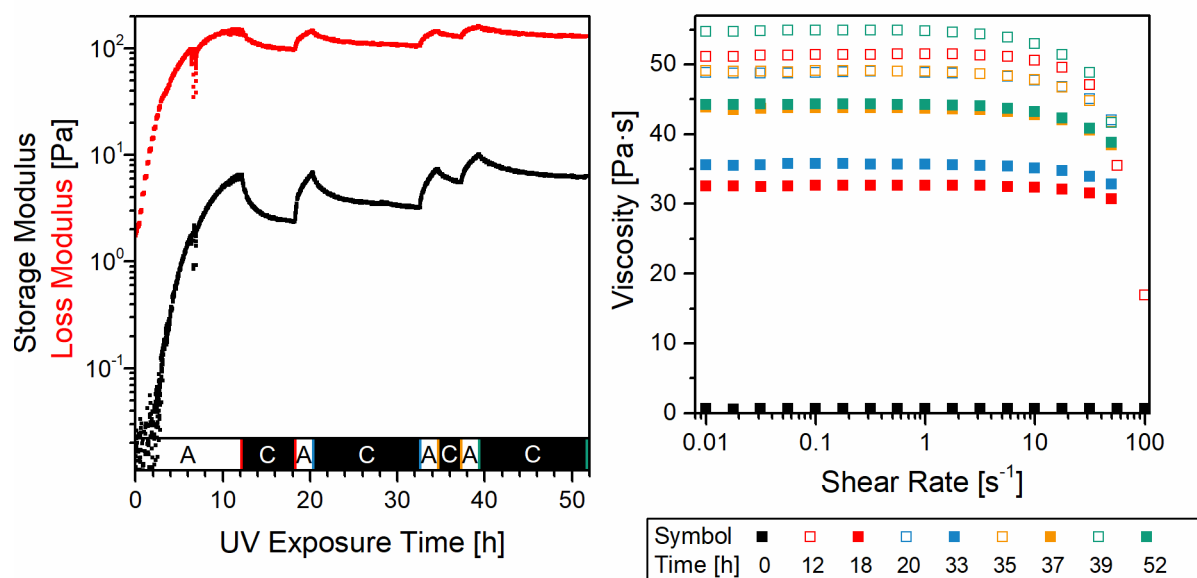
Figure 7: Alteration of storage and loss moduli of PDMS-A$_2$ by sequential UV-A and UV-C radiation (left) and the dependence of the viscosity on the shear rate after each programming step (right).

reached even at high frequencies, indicating that the influence of chain entanglements is negligible.[127] After the initial UV-A period, dynamic moduli are repetitively decreased and increased within a certain range by repeated, consecutive UV-C and UV-A exposure. The influence of photoprogramming is higher on the storage modulus compared to the loss modulus. The chance of a PDMS chain to break upon back reaction depends on the number of anthracene dimers in the backbone. Longer polymer chains contain more dimers, which
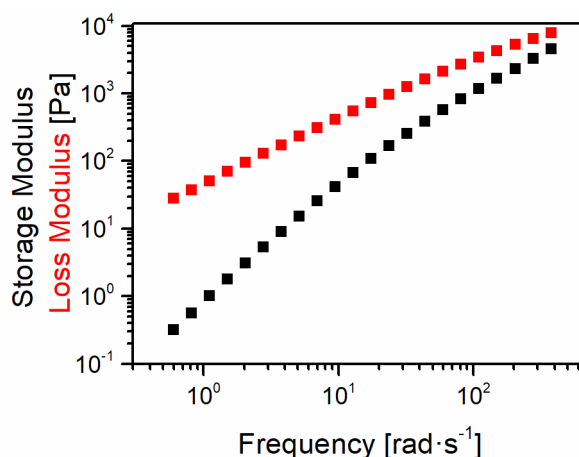
Figure 8:   *Dynamic moduli recorded as a function of frequency for PDMS-A$_2$ after the first cycle of UV-A radiation (see Figure 7 and Table 2).*

increases their chance to undergo cleavage. As the storage modulus has a stronger dependency on the fraction of long chains, the programming effect is more pronounced for the storage modulus. For example, in the first cycle of UV-C exposure, the storage modulus reduces by 62 ± 1 % compared to the loss modulus and the zero shear viscosity only decreases by 32 ± 2 and 36.93 ± 0.09%, respectively. Another finding is that dynamic moduli show a general tendency to increase with the number of cycles (Table 1). The reaction times need to be rather long for the used light sources. As a consequence the maximum conversion after the first UV-A radiation period is not reached. Thus, the chain extension and in turn the increase of moduli can still continue to reach higher levels upon the restart of UV-A radiation. In addition, increasing moduli as a function of cycles are likely to be influenced by the dependency of the molar mass of the anthracene-bearing PDMS chains on the dimerization kinetics. Following this hypothesis, anthracene esters attached to short chains are more mobile due to the dependency of the diffusion on the hydrodynamic radius of the polymer and find a reaction partner faster than comparatively long chains. A hint that this is indeed the case is given by the slopes of the curves for the dynamic moduli at the beginning of each UV-A period. The cleavage of a part of the anthracene dimers within a UV-C period

Table 1: *Rheological properties of PDMS-A$_2$ after each programming cycle corresponding to data shown in Figure 7. Dynamic moduli were averaged over the last 12 min of each radiation cycle and zero shear viscosity was measured after each radiation cycle.*

Cycle		t [h]	G' [Pa]	G" [Pa]	η_0 [Pa·s]
0	-	0.0-0.2	0.0095 ± 0.01	1.88 ± 0.08	0.5794 ± 0.0005
1	UVA	12.0-12.2	6.4 ± 0.1	145 ± 4	51.31 ± 0.04
	UVC	18.1-18.3	2.39 ± 0.02	98.0 ± 0.8	32.57 ± 0.03
2	UVA	20.2-20.4	6.7 ± 0.1	146 ± 2	48.83 ± 0.03
	UVC	32.4-32.6	3.23 ± 0.02	106.0 ± 0.6	35.70 ± 0.04
3	UVA	34.5-34-7	7.37 ± 0.06	144.40 ±0.05	49.02 ± 0.02
	UVC	37.1-37.3	5.54 ± 0.02	128 ± 1	43.70 ± 0.03
4	UVA	39.2-39.4	10.02 ± 0.1	160 ± 1	54.80±0.03
	UVC	51.5-51.7	6.27 ± 0.07	130 ± 1	44.23 ± 0.02

should occur independently of the molar mass of the dimer bearing PDMS chain and of the exact position of this dimer within the chain. Consequently, each cleavage step always generates a fraction of short chains even though the average molar mass remains high due to the low extent of cleavage. In this scenario, the initial slope of the curve at the start of a UV-A period is always high even though it starts at a higher level of moduli each time. Finally, these short chains can meet the anthracene termini of very long chains and extend them further upon renewed UV-A exposure. With the long chains alone, a chain extension occurs very slowly due to the decreased mobility of the reaction partners in this case. In summary, the repeated partial cleavage of the anthracene dimers within the UV-C radiation periods causes a situation in which the length of the chains extends further and further and ultimately leads to ever increasing moduli with continuing radiation. The comparison between the molar mass distributions analyzed by UV detected SEC of this experiment and a similar experiment that was stopped after the first cycle of UV-C radiation at 18 h is shown in Figure 9. A negative shift of the skewness is found for the curve recorded after four radiation cycles. Additionally, the molar mass distribution shows a shoulder at a higher molar mass after four cycles, which is not as obvious after one cycle of photoprogramming. The absorption of UV-light results predominantly from the anthracene dimers and not from the backbone of the polymer. As previously discussed, the dimer concentration is dependent on the precursor length and shifts to higher molar masses. Consequently, the shifted skewness indicates increased incorporation of short precursors to chains of higher molar masses. The observed skewness trend supports our hypothesis that extension of long chains by shorter species is responsible for ever-increasing dynamic moduli with the number of cycles.
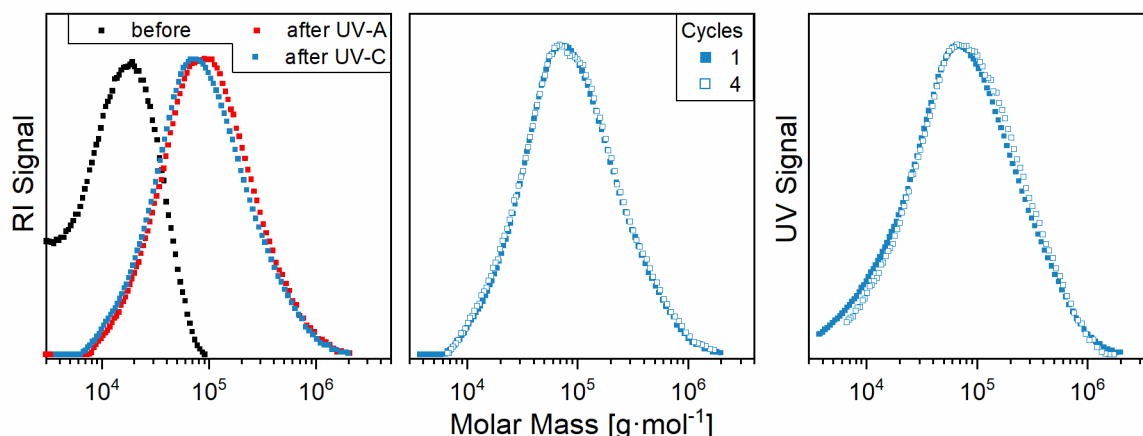
Figure 9:   *SEC traces of PDMS-A$_2$ subjected to rheological analysis under UV-radiation. Evolution of molar mass weight distribution upon a first full switching cycle (left) and comparison of molar mass distributions of samples subjected to one and four UV-A/UV-C cycles (middle and right).*

Another feature, which is observable in the rheometer traces of the cycling experiments, is that the programming range gets smaller from cycle to cycle, meaning that the changes in dynamic moduli during each radiation period decrease over the course of the experiment. Following the reaction by NMR spectroscopy reveals that this decline of programming range is linked to a loss of anthracene functionality, as indicated by a change in the pattern of relevant signals (Figure 13A and B) upon prolonged UV exposure. This effect is further accompanied by the occurrence of small, insoluble gel particles upon NMR sample preparation, pointing to a partial, irreversible crosslinking during UV treatment. It seems, therefore, that irreversible damage to the structure occurs upon prolonged O$_2$ and UV-light impact as separately discussed in Chapter 3.1.1.3. It is noted, however, that a limitation in exposure time can easily prevent the damage over several cycles, as indicated by UV/VIS measurements (Figure 4).

The change of dynamic moduli and zero shear viscosity for the monofunctional PDMS-A$_1$ was analyzed over two cycles of alternating UV-A and UV-C radiation (Figure 10 left and Table 2). PDMS-A$_1$ bears a single anthracene unit per chain. Consequently, only one coupling step per chain is possible upon dimerization of the anthracene in contrast to PDMS-A$_2$, where coupling was not limited to this one step. The initial loss modulus of 0.83 ± 0.07 Pa reaches a plateau at 2.55 ± 0.5 Pa within 3 h of UV-A exposure. Accordingly, a change in shear viscosity from 0.2583 ± 0.0006 to 0.847 ± 0.001 Pa·s is observed. Measured storage moduli below 10^{-1} Pa indicate no significant elastic behavior. SEC traces recorded after performing the two programming cycles in the rheometer exhibit a bimodal molar mass distribution with the major fraction showing a maximum at the double molar mass compared to the minor fraction (Figure 10, right). The latter represents uncoupled PDMS-A$_1$ with unreacted anthracene ester end groups, while the first one is attributed to chains that are coupled by the dimerization reaction. Keeping in mind the small extent of cleavage of anthracene dimers upon UV-C impact

(Figure 4; 88 % of all anthracenes remain in the dimer state), the low molecular weight shoulder appears rather large. This indicates that even before UV-C exposure, not all chains had been coupled, even though UV-A treatment leads to almost 95 % conversion. The remaining discrepancy is suggested to be the result of an incomplete functionalization of the PDMS chain ends with anthracene moieties.
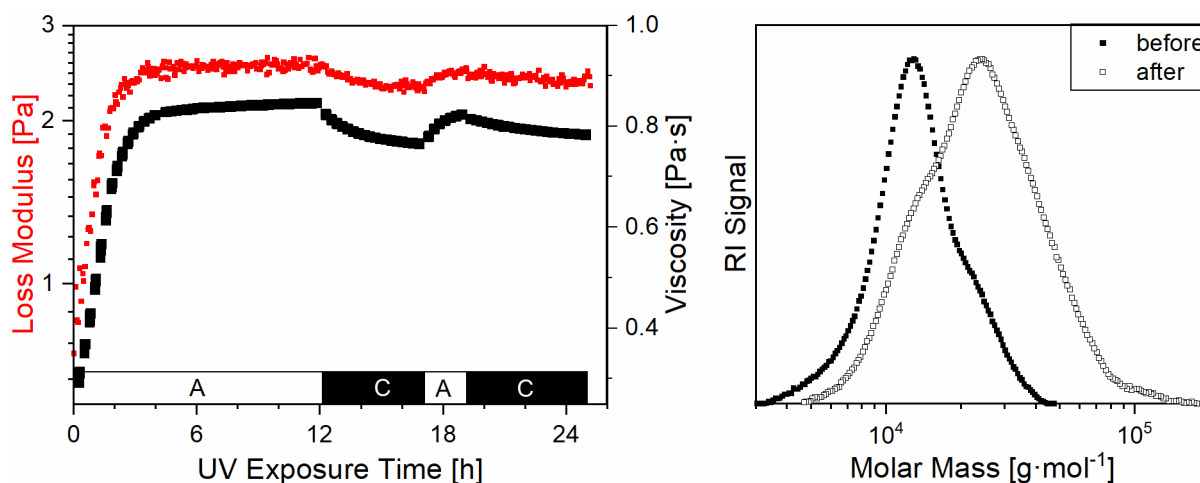
Figure 10: Alteration of storage modulus and viscosity of PDMS-A$_1$ by sequential UV-A and UV-C radiation (left). Corresponding SEC traces before and after the radiation (right).

Table 2: Rheological properties of PDMS-A$_1$ after each programming cycle corresponding to data shown in Figure 10. Dynamic moduli were averaged over the last 12 min of each radiation cycle and zero shear viscosity was measured after each radiation cycle.

Cycle		t [h]	G' [Pa]	G" [Pa]	η_0 [Pa·s]
0	-	0.0-0.2	0.04 ± 0.06	0.83 ± 0.07	0.2583 ± 0.0006
1	UVA	11.9-12.1	0.02 ± 0.08	2.55 ± 0.05	0.847 ± 0.001
	UVC	16.9-17.1	0.00 ± 0.01	2.29 ± 0.02	0.7625 ± 0.0006
2	UVA	18.9-19.1	0.00 ± 0.02	2.46 ± 0.01	0.8243 ± 0.0003
	UVC	25.0-25.1	-0.02 ± 0.03	2.37 ± 0.04	0.7826 ± 0.0006

A complete functionalization of polymer chain ends is a typical issue of post-polymerization modification. NMR, which is used to verify the success of end group functionalization, unfortunately, is not sensitive enough to the remaining few percent of functionalization. A dimerization conversion slightly below 100 % together with a slightly incomplete chain-end functionalization also explains why the molar masses reached for the bifunctional PDMS-A$_2$ are not higher. According to the principles of step-growth polymerization, a very large molar mass increase is only achieved at very high conversion (i.e., level of coupling), which the current system does not provide. Upon 3 h of UV-C exposure of PDMS-A$_1$, the storage modulus and zero shear viscosity decrease by 15 ± 4 and 14.4 ± 0.3 %, respectively. As

expected, a significantly smaller range of programmability compared to PDMS-A_2 is observed, as further chain extension is excluded after coupling of two chains. This, on the other hand, leads also to faster completion of the UV-triggered programming. Furthermore, the programming range decreases in the second cycle similar to that observed for the bifunctional PDMS-A_2. As noted before, this is the result of structural damage of the anthracene units upon prolonged UV exposure. The different programming ranges of PDMS-A_1 and PDMS-A_2 give an opportunity to control the change of mechanical properties of the material independent of the duration of UV exposure. For this, mixtures of both batches can simply be mixed. PDMS-A_1 functions as a stopper that limits the maximum achievable chain extension. Figure 11 (left) displays the evolution of loss moduli with UV-A and subsequent UV-C exposure for mixtures of PDMS-A_1 and -A_2 with different mixing ratios. As expected, the mixtures reach values that are intermediate between those of the pure materials. SEC results (Figure 11, right) are in line with this observation.
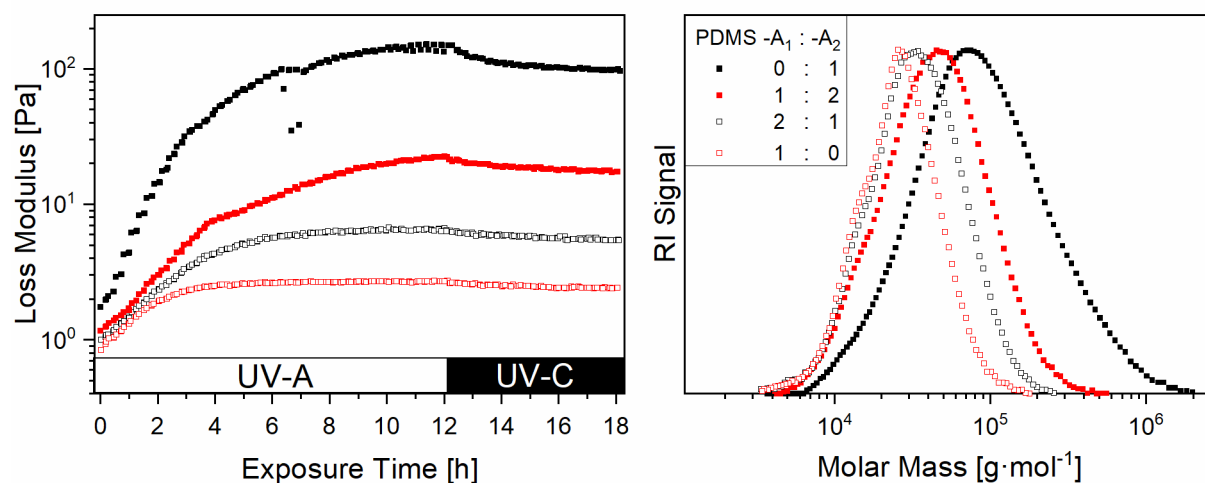
Figure 11: Alteration of the loss moduli of mixtures of PDMS-A_1 and PDMS-A_2 at different mixing ratios (by weight) upon sequential UV-A and UV-C radiation (left), and corresponding SEC traces (right).

3.1.1.2.2 Thermal Programming

Although photochemical reprogramming demonstrates reversible alteration of rheological properties, the conversion of the dimer cleavage limits the reprogramming range. Thermal treatment is an alternative for the reprogramming of dimerized anthracene functionalized silicone oils. An analysis of heated PDMS-A$_2$ before and after UV-A treatment by an oscillatory experiment is demonstrated in Figure 12 (right). In contrast to light exposure, temperature change has an intrinsic influence on the viscoelastic properties of all polymer melts. Consequently, the heating of PDMS-A$_2$ without any previous UV radiation shows a characteristic decrease in the loss modulus. Also, the heating of a UV-A-treated PDMS-A$_2$ shows the typical temperature dependency of the loss modulus below 130 °C. The subsequent decrease of the slope above 130 °C indicates the onset of cycloreversion that additionally contributes to the reduction of the loss modulus upon heating. During an isothermal step at 180 °C, the loss modulus reaches a minimum as cycloreversion is completed. After cooling to 20 °C, the loss modulus is almost the same as that found for the material before UV-A radiation, which shows the complete reversibility of the programming by heat. Repetitive programming of PDMS-A$_2$ using a sequence of UV-A radiation and heating to 180 °C followed by cooling to RT demonstrates this reversibility over at least three cycles (Figure 12; left). ^{1}H-NMR spectroscopy also confirms that the signals of the anthracene ester are fully restored, meaning that the anthracene units are still intact after a programming cycle (Figure 2E). Thermal reprogramming, therefore, represents a valuable alternative to UV-C treatment. The programming is faster and covers a larger range and additionally demonstrates good reproducibility regarding observed moduli over all three cycles. Structural damage is not observable, which is in line with the fact that PDMS is known for its good thermostability.
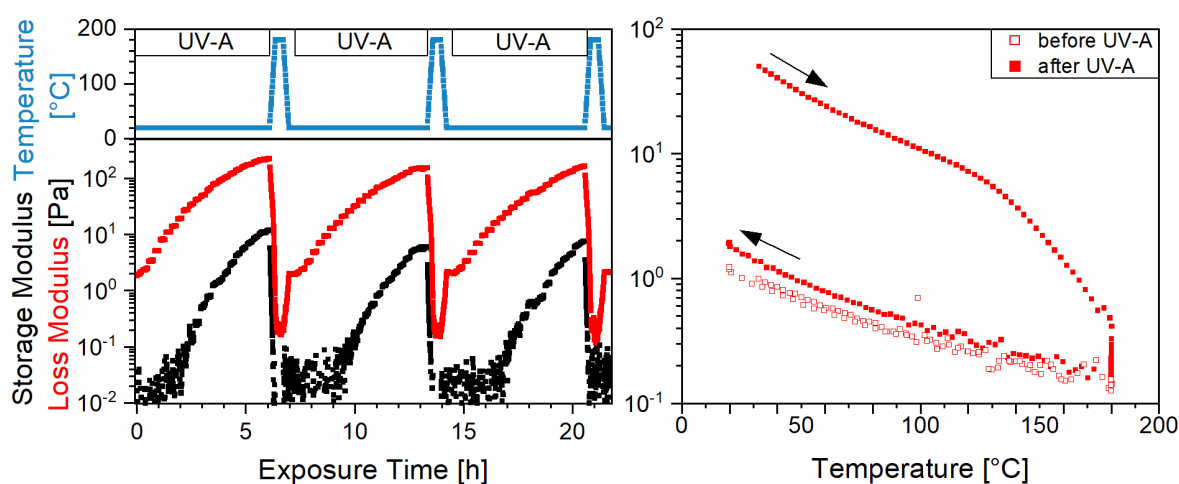
Figure 12:   *Alteration of storage and loss moduli of PDMS-A$_2$ by sequential UV-A radiation and temperature treatment (left). Loss modulus as a function of temperature for PDMS-A$_2$ after and and prior to UV-A treatment.*

3.1.1.3 Photooxidative Stability

The rheological experiments presented in Chapter 3.1.1.2.1 reveal limits regarding the reprogramming of the functionalized silicone oil under the influence of long-term UV exposure. The basic anthracene structure is altered upon prolonged UV-A or UV-C exposure as indicated by multiple new signals in the aromatic region of the ^{1}H-NMR spectrum shown in Figure 13. Further signals appear in the region 4-5 ppm. Typically, the methylene group adjacent to the aromatic ester appears around this of chemical shift. Accordingly, the spectrum shows that side reactions take place near the pre-polymer terminus. One side reaction pathway is identified as the oxidation of anthracene indicated by the signals a and b, which assign to the byproduct anthrachinone. Consequently, this side reaction is expected to disappear when oxygen is excluded. A respective experiment investigates whether material damage occurs when the radiation of the functionalized silicon oils with UV-A or UV-C is carried out under an inert argon atmosphere. The corresponding ^{1}H-NMR spectra show no new signals after illumination (Figure 13C and D). In the case of a long UV-A exposure under argon, the complete solubility of the sample further confirms that no material damage occurs. However, samples radiated with UV-C light under argon contained insoluble gel particles in $CDCl_3$. The gel formation clearly indicates a formation of crosslinks, and thus another kind of undesired side reaction. The solubility issue of the corresponding sample explains why no signals indicating a side reaction are evident in the corresponding ^{1}H-NMR spectrum.

The suppression of side reactions involving singlet oxygen is another approach to improve the long-term stability. Anthracene derivatives undergo [2+4] cycloadditons with singlet oxygen yielding endoperoxides (Scheme 13). Depending on substituents on the aromatic ring, endoperoxides can either undergo cycloreversion into anthracene and oxygen by C-O cleavage or form hydroxyl-ketones and quinones by irreversible O-O cleavage.[128] Endoperoxide formation can be kinetically reduced by additional steric hindrance through substituents in the 9- or 10-position or by electron withdrawing substituents.[129] It is also conceivable that singlet oxygen quenchers such as HALS[130] may prevent reactions between oxygen and anthracene.
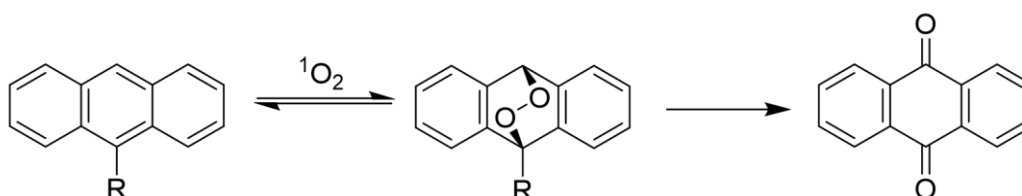
Scheme 13:   *The oxidation of anthracene derivatives leading to anthraquinones via the reversible formation of an endoperoxide intermediate.*
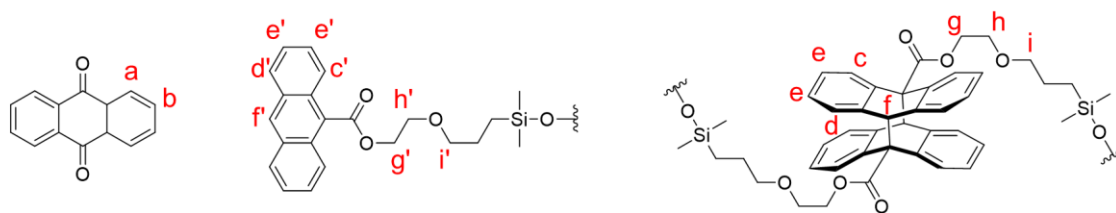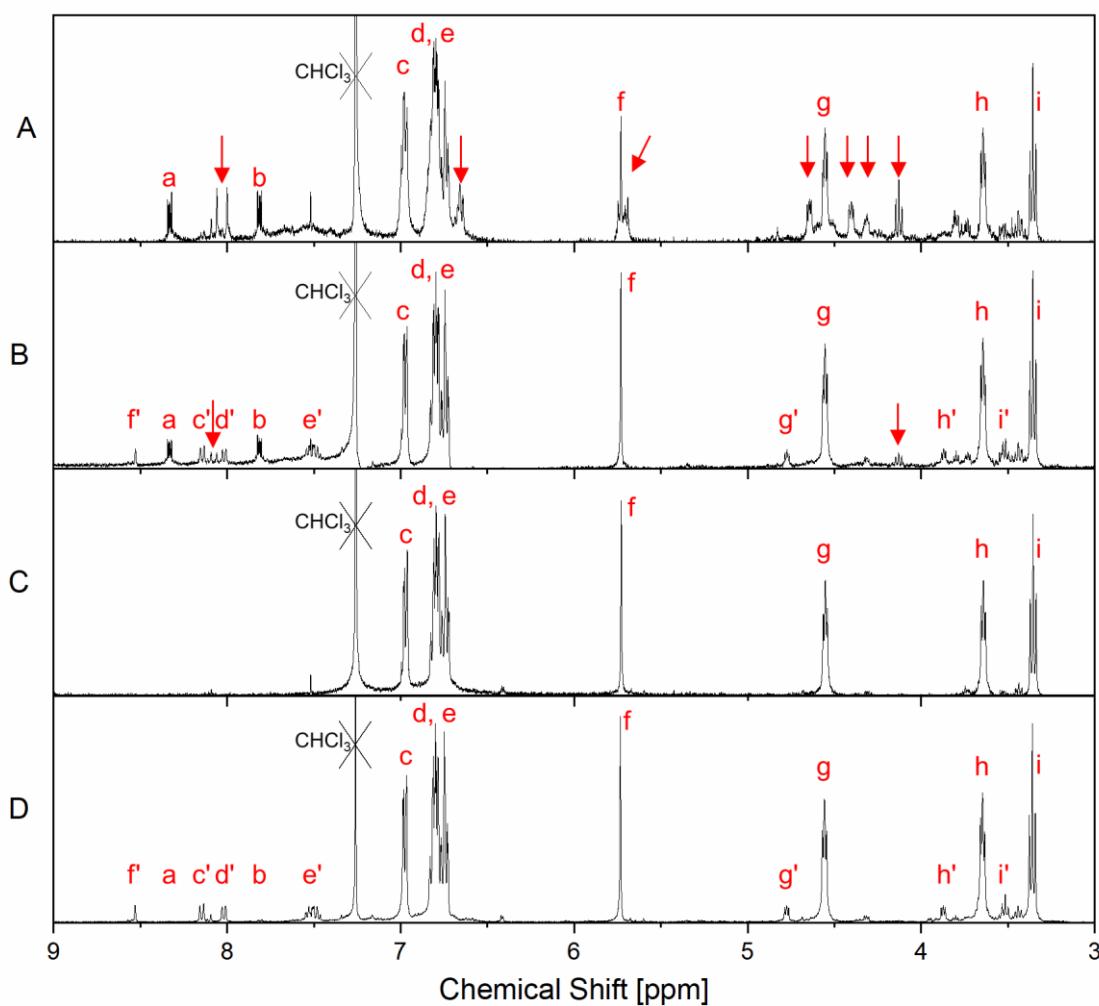
Figure 13: *^{1}H-NMR of PDMS-A$_2$ after 36 h of UV-A (A) or UV-C (B) radiation at air, and after UV-A (C) or UV-C (D) radiation under argon atmosphere. The signals a and b (assigning to anthrachinon) and red arrows indicate occurrence of undesired side reactions.*

To test this approach, blends of PDMS-A$_2$ with a PDMS copolymer carrying HALS units in the side chain were investigated (Figure 14). The PDMS backbone of the copolymer acts as a phase mediator and enables the solubility of the HALS moiety. The radiated mixtures were analyzed by ^{1}H-NMR spectroscopy. Here, the ratio between signals representing the anthracene esters and anthraquinone calculated according to Equation (15) shows that no significant decrease in oxidation occurs in the presence of HALS (Figure 13). Contrary to the intention, higher oxidation rates are found for increasing higher weight fraction of PDMS-HALS. Since the unfavorable results do not contribute to the intended material development, this approach was not pursued further in this thesis.

In summary, radiation under exclusion of oxygen leads to better material stability only in the case of UV-A. The radiation under inert atmosphere with UV-C as well as the use of HALS as singlet oxygen quencher could not prevent side reactions completely. Accordingly, the photochemical reprogramming of the system so far shows limitations and is therefore only suitable for applications in which the exposure time or the number of reprogramming steps is limited.

$$Oxidized\ Anthracene\ Units = \frac{I^a + I^b}{(I^a + I^b) + (I^c + I^{de})} \qquad (15)$$
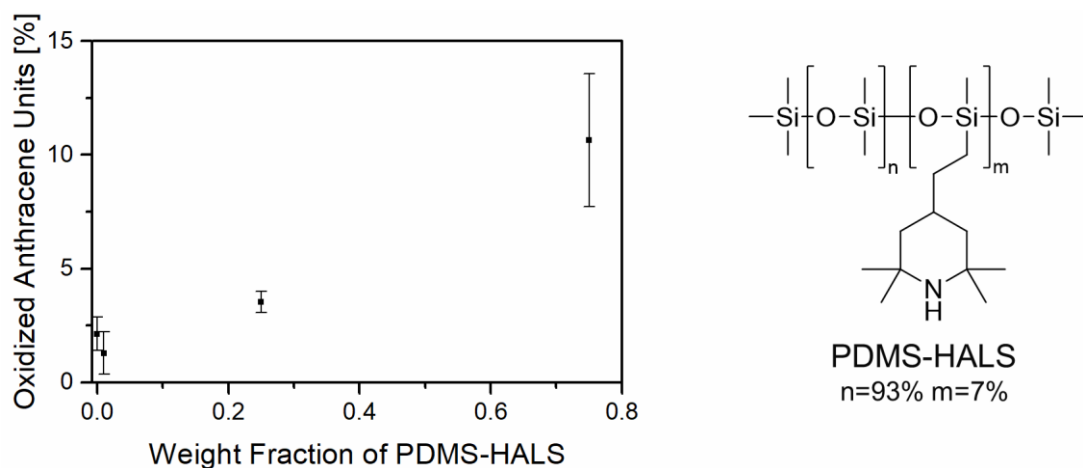
Figure 14: *Oxidation of anthracene units in mixtures of PDMS-A$_2$ and PDMS-HALS (right) after 36 h UV-C exposure.*

3.1.2   Mixtures with Native PDMS

Lubricants are often formulated from various components. Typically, additives are mixed into the base oil to accomplish an improvement of certain properties, such as frictional performance or long-term stability, and thus improve the lubricant in a cost-effective manner. Following this concept anthracene-functionalized silicone oils are assessed as additives for the implementation of switchable viscosity to a standard PDMS base oil.

It is expected that anthracene-functionalized PDMS must show good phase compatibility with the base oil in order to apply the principle of viscosity control by changing the molar mass to the entire mixture. Accordingly, the occurrence of phase separation is undesirable. In addition, it can be expected that phase separation affects the effectiveness of the photoprogramming process by scattering the light away. The additional light attenuation in the material in case of insufficient mixing may, for example, further support the programming of inhomogeneous material behavior. While the polymer backbone of the additives tested (PDMSX-A_2) is similar to the base oil (PDMS) and promotes phase compatibility, the anthracene ester termini are chemically different which could possibly lead to phase separation. Accordingly, it is first considered whether a certain concentration of anthracene domains affects miscibility. For this purpose, various linear anthracene-functionalized PDMS polymers are investigated. The polymers used differ in their molar mass and consequently in their volume ratio between PDMS backbone and anthracene ester domain. After an analysis of the miscibility, the second part of this chapter compares the performance of the switchable viscosity of the anthracene-functionalized polymers of different chain lengths.

Two of the tested additives, PDMS0-A_2 and PDMS-A_2 are synthesized as discussed in Section 3.1.1.1 and depicted in Scheme 11. The bis(hydroxyethoxypropyl)-terminated PDMS precursors, PDMS0-$(OH)_2$ and PDMS-$(OH)_2$, respectively, differ from each other by the molar mass. Two more additives, PDMS2-A_2 and PDMS3-A_2 are chain-extended from PDMS-$(OH)_2$ by urethane links, prior to the introduction of terminal anthracene esters (Scheme 14). Isocyanate coupling is a facile synthetic possibility to provide precursors with higher initial chain length which reduces the volume ratio between the anthracene ester and PDMS backbone in the final additive. This approach appeared to be necessary, as PDMS-$(OH)_2$ of higher molar mass was not commercially available and its synthesis exceeded the scope this work. When comparing the structure of PDMS-A_2 with PDMS2-A_2 and PDMS3-A_2, it should be kept in mind that the number of PDMS block termini is the same in all three cases, but part of the PDMS backbone is replaced by urethane bridges. Accordingly, the miscibility by urethane extension only leads to improvement if the urethanes also show increased phase compatibility compared to the anthracene esters or dimers. The strategy was nevertheless considered useful, as

literature references highlight the general, very poor solubility of anthracene dimers.[46] It was reported that the dimerization of anthracene esters in solution leads to in-situ precipitation of the dimers.[45] This observation could also be reproduced for the PDMS base oil by demonstrating the precipitation of crystals upon UV-A radiation of a saturated solution of 9-anthracenecarboxylic acid ethyl ester in the PDMS base oil (Figure 31 in appendix).
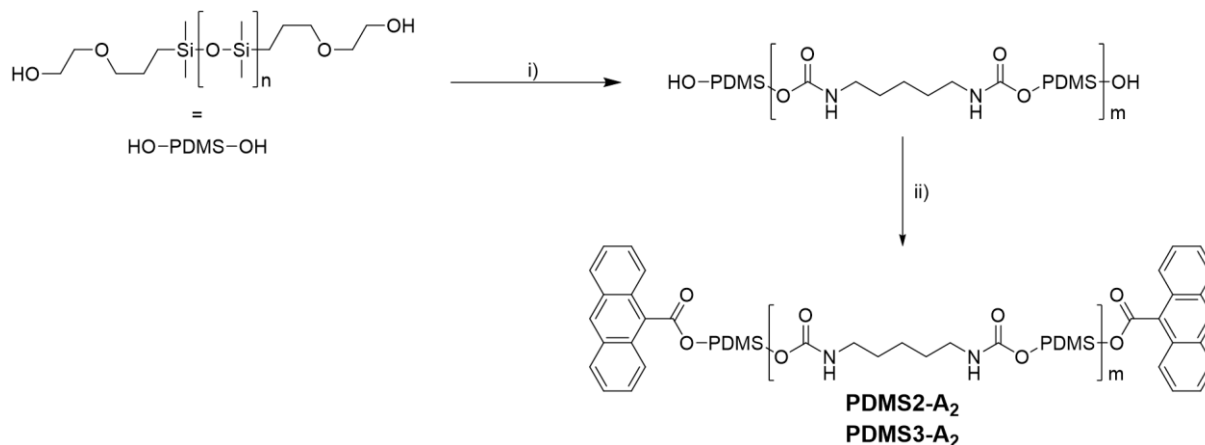
Scheme 14: Synthesis of anthracene-terminated PDMS2-A_2 and PDMS3-A_2 by chain extension via urethane formation and subsequent esterification. i) HDI, DABCO, toluene, 5 h 70 °C ; ii) 9-anthracenecarbonyl chloride, 20 h, 60 °C.

The diisocyanate HDI is selected as coupling agent for the synthesis of PDMS2-A_2 and PDMS3-A_2 because it is relatively small, flexible and cheap. Urethane extension using DABCO as a base works well, as indicated by the higher molar mass of PDMS2-A_2 and PDMS3-A_2 compared to PDMS-A_2 (Table 3). More coupling reagent leads to more urethane links. Therefore, PDMS3-A_2 possesses the highest molar mass. The dispersities of PDMS2-A_2 and PDMS3-A_2 are lower compared to PDMS-A_2. Since all these pre-polymers are synthesized from the same precursor PDMS-$(OH)_2$ the narrowing of the molar mass must appear during the isocyanate linkage. This is attributed to preferential coupling of shorter polymer chains. The reacting hydroxyl groups are statistically more abundant on short chains. In addition, short chains have a smaller hydrodynamic radius and thus a higher mobility.

Table 3: Average molar masses and dispersities analyzed by SEC, and the ratio between terminal PDMS block functionalities (anthracene ester, urethane and alcohol) determined by ^{1}H-NMR spectroscopy of the anthracene-functionalized silicone oils PDMSX-A$_2$ and the PDMS base oil.

| | M_n | M_w | Đ | Anth. | Ureth. | Alk. |
	[kg·mol^{-1}]	[kg·mol^{-1}]		[%]	[%]-	[%]
PDMS0-A$_2$	3.9	7.6	1.9	99	-	1%
PDMS-A$_2$	7.6	17	2.6	95	-	5%
PDMS2-A$_2$	15	29	1.9	55	39	6%
PDMS3-A$_2$	17	36	2.1	35	61	4%
PDMS base oil	8.6	12	1.4	-	-	-

The ^{1}H-NMR spectra confirm the formation both of urethane links and anthracene esters (Figure 15). Signals are apparent originating from the methylene groups adjacent to the ester, ether, and urethane at the ends of each PDMS block. The ester modification causes a stronger deshielding of the surrounding methylene groups compared to the urethane causing respective signals to appear at higher a chemical shift. The estimation of the ratios between the PDMS block termini is given by Equations (21) and (22). Table 3 presents the percentage of anthracene ester, urethane and the unmodified alcohol. An overall conversion of the hydroxyl groups of ≥ 94 % is reached for all PDMSX-A$_2$. Considering Carothers' Equation (14), this leads to the expectation that similar maximum molar masses are achievable at full dimerization for PDMS-A$_2$, PDMS2-A$_2$ and PDMS3-A$_2$.

$$Anthracene\ ester = \frac{a}{a+b+c}; \quad Urethan = \frac{b}{a+b+c}; \quad Alkohol = \frac{c}{a+b+c} \qquad (16)$$

$$a = \frac{I^a + I^b + I^c + I^d + I^h + I^{kl} - I^i}{13} \quad b = \frac{I^g + I^j + I^{op} - I^i + I^q}{8}, C = \frac{I^i}{2} \qquad (17)$$
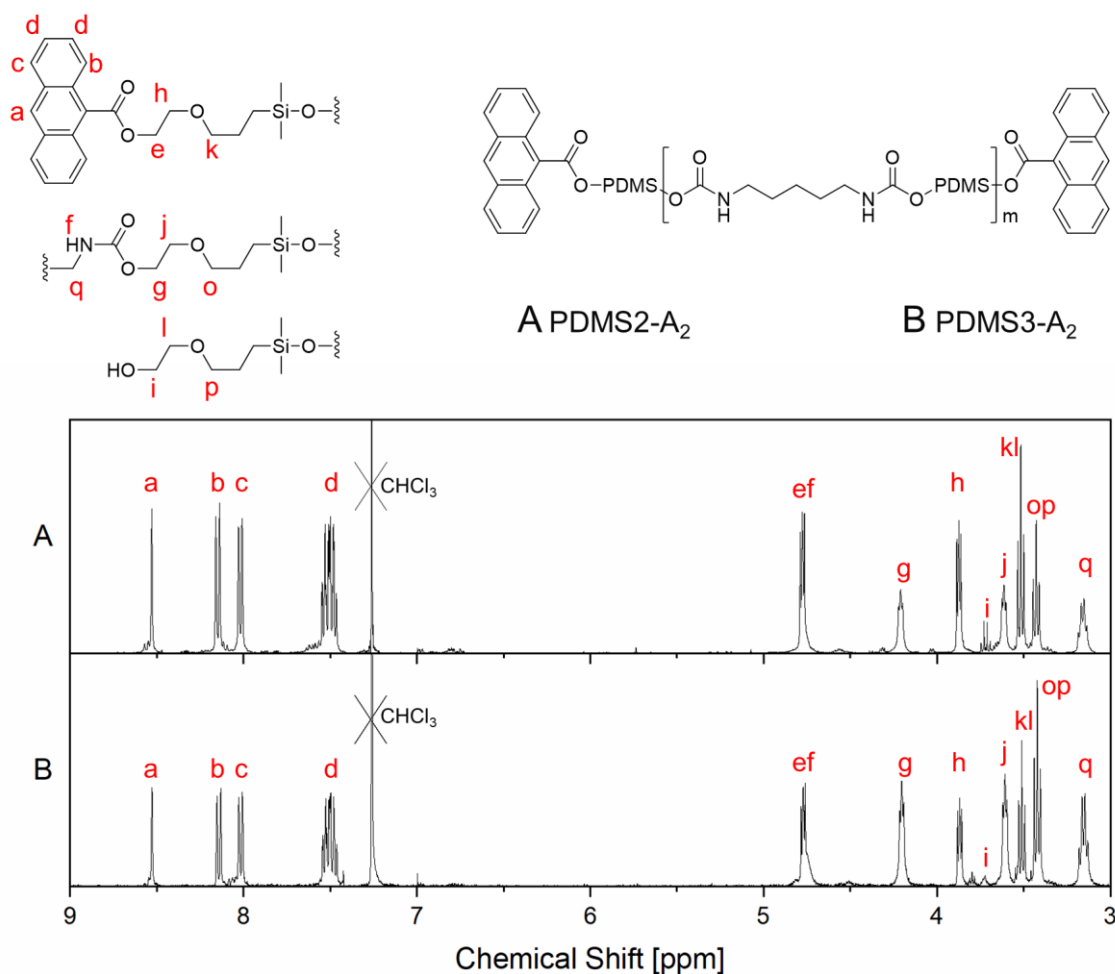
Figure 15: ^{1}H-NMR spectra and assignment of signals to the termini of PDMS2-A$_2$ and PDMS3-A$_2$.

The fluorescence microscope (FM) images of blends consisting of the anthracene functionalized PDMSX-A$_2$ and the PDMS base oil in different mass ratios are shown in Figure 16. Associated BF images are appended as Figure 32. The pure PDMS base oil is confirmed non-fluorescent by a control experiment. In principle, the fluorescence intensity increases with the concentration of the fluorophore anthracene ester. This allows to make general qualitative statements about the anthracene density within an image. However, the occurrence of artifacts due to uneven excitation illumination must be considered. This is particularly visible in the lower right corner of some images, especially in the images A0 and A1. The comparability between the images has certain limitations. The fluorescence intensity of the images is affected by the thickness of the oil film under investigation. This could be controlled to some extent by maintaining the same preparation protocol for all samples, but variations still occur. Nevertheless, there is a clear trend of intensity decrease in row A from left to right comparing the different PDMSX-A$_2$. This trend is consistent with the increase in molar mass and the resulting decrease in anthracene concentration (see Table 3). The decrease in intensity is also visible within a column, as is common when diluting a dye in a

non-fluorescent medium. PDMS0-A_2 mixtures phase separate at all tested ratios (column 0B-E). The phase of the smaller fraction appears as micron-sized droplets, which show higher fluorescence intensity. Furthermore, it is visible that the continuous phase shows some fluorescence. This can be explained by the partial miscibility of PDMS0-A_2 and may also be enhanced by light scattering effects or a luminous background out of focus. However, the partial miscibility of PDMS0-A_2 is to be expected on the basis of a preliminary experiment showing the miscibility of 9-anthracenecarboxylic acid ethyl ester in PDMS base oil (Figure 31 in appendix). For the anthracene-functionalized silicone oils, it can be expected that the phase compatibility with the continuous PDMS phase improves with increasing length of the PDMS chain to which the anthracene units are attached. Correspondingly, the blends of PDMS-A_2 and the base oil shown in columns 1B-E support this interpretation. The increasing PDMS chain length of PDMS-A_2 compared to PDMS0-A_2 further improves the miscibility with the base oil. Here, only a few, smaller and anthracene-rich drops are visible. 33 % and 50 % PDMS2-A_2 as well as 50 %PDMS3-A_2 even mix without optically detectable phase separation. This indicates, that urethane links indeed improve the phase compatibility to some extend. However, higher urethane content and molar mass again lead to phase separation, as shown by the comparison of PDMS3-A_2 and PDMS2-A_2 blends. Interestingly, the phase separation of the tested urethanes is preferentially observed at low volume fractions. Another miscibility feature of the mixtures is connected to a decrease of miscibility upon anthracene dimerization. Figure 17 illustrates the response of 33 wt% PDMSX-A_2 mixtures over time and under exposure to UV-A light. PDMS0-A_2 represented in column 1 phase separates after the first UV-A radiation cycle. The newly-formed small drops connect to form bigger drops during the subsequent radiation cycles. The UV-triggered phase separation is not observed for PDMS-A_2 and PDMS2-A_2. In this case, the total anthracene concentration is lower and the longer PDMS blocks enable sufficient solubility for the newly formed and less soluble anthracene dimer end groups. However, the response of PDMS3-A2 shows that the light-induced phase separation occurs again above a certain molar mass or urethane content.
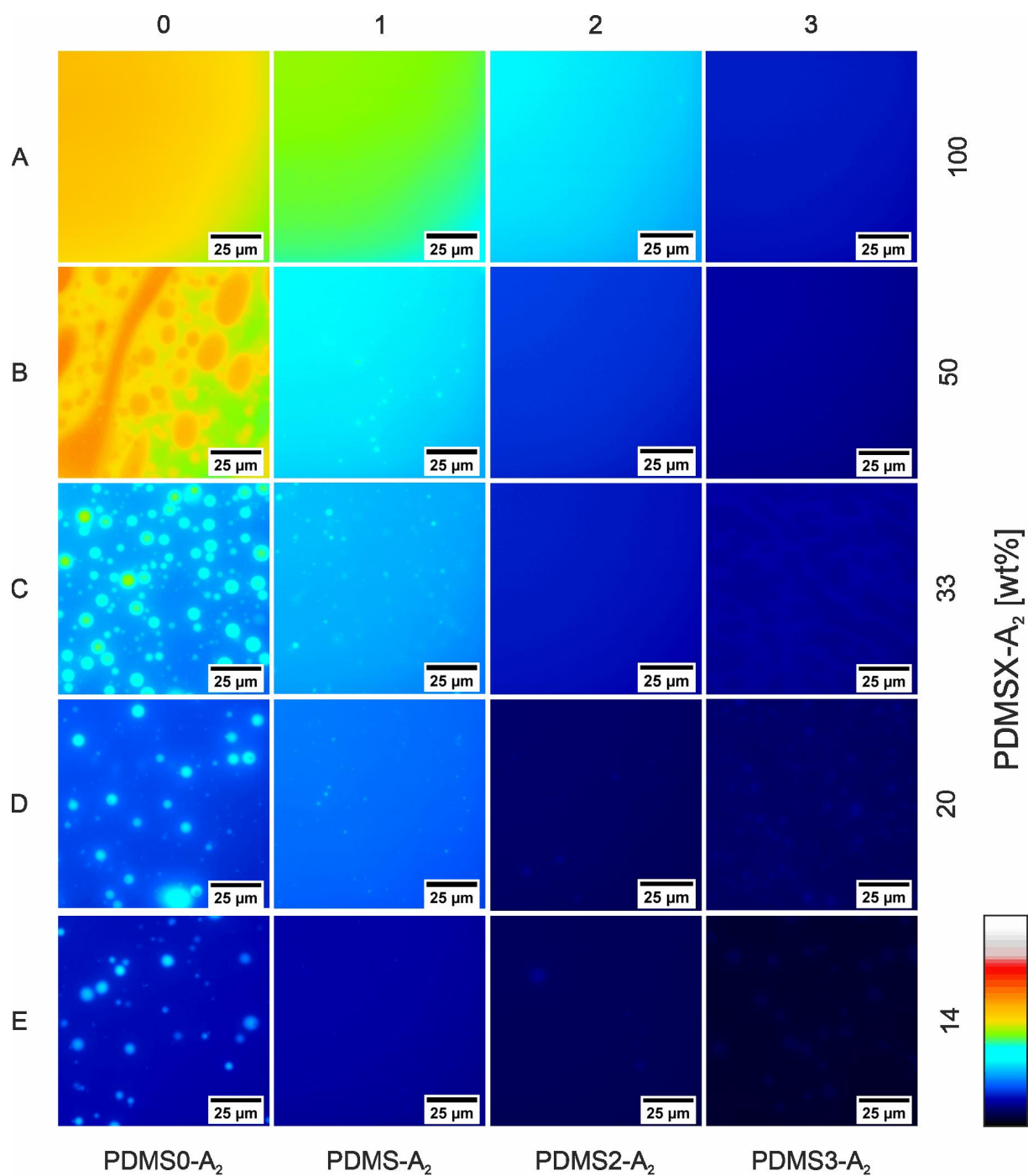
Figure 16: *FM images of mixtures of either PDMS0-A_2 (0), PDMS-A_2 (1), PDMS2-A_2 (2) and PDMS3-A_2 (3) with native PDMS in varying mass fractions (A-E). Associated BF images are shown in Figure 32 (appendix).*
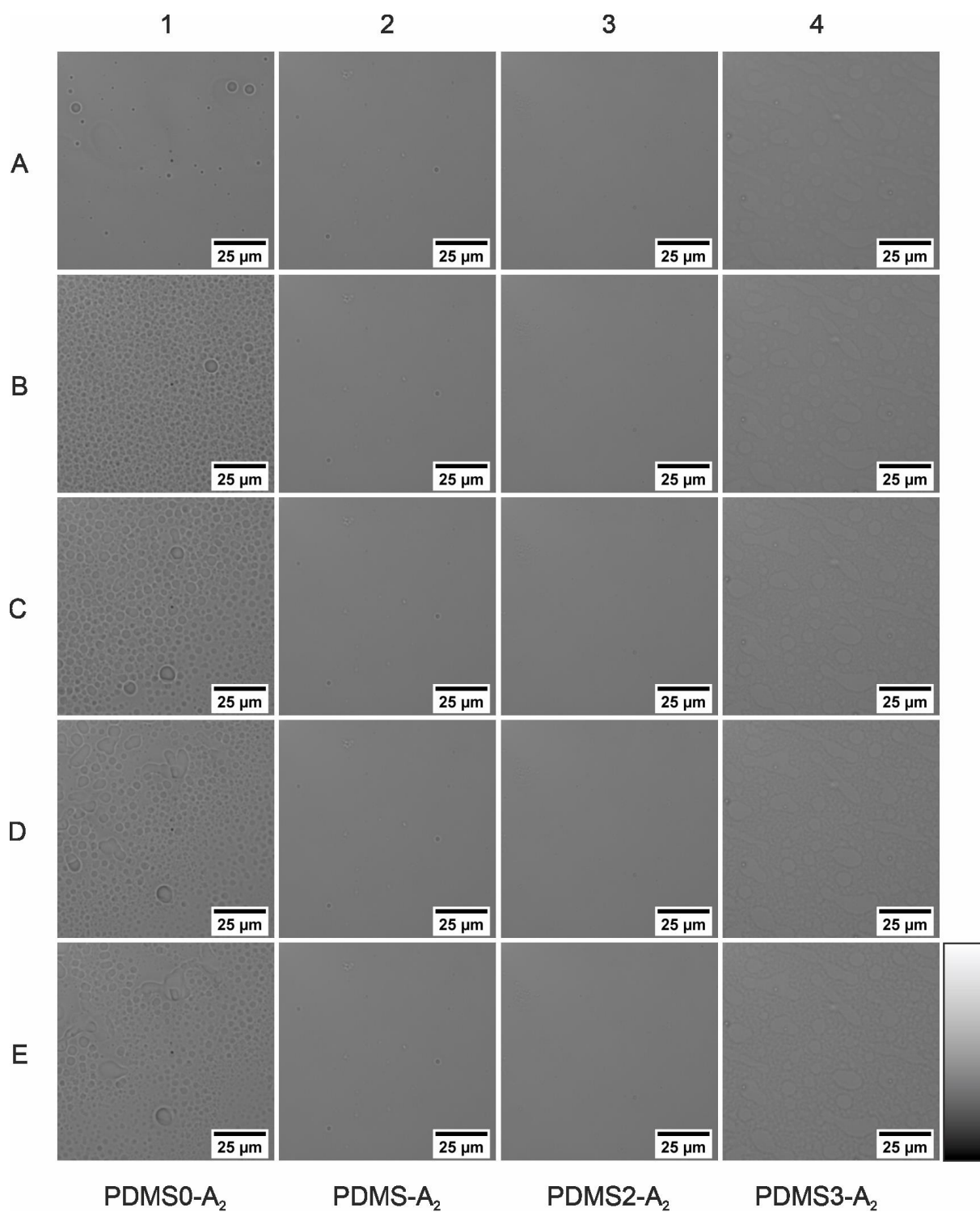
Figure 17: *BF images of mixtures composed of PDMS base oil with 33 wt% of either PDMS0-A$_2$ (0), PDMS-A$_2$ (1), PDMS2-A$_2$ (2) or PDMS3-A$_2$ (3) before (A) and after (B-E) four radiation cycles with UV-A light. The radiation cycles were performed every 15 s. Associated fluorescence microscopy images are shown in Figure 33 (appendix).*

Figure 18A demonstrates the rheological properties of mixtures of PDMSX-A$_2$ and the PDMS base oil. It shows the evaluation of loss modulus under UV-A exposure and respective flow curves before and after the photoprogramming (Figure 18A and B). The molar mass distribution by SEC analysis of the samples after each rheometer experiment is depicted in Figure 18 C. It must be noted that the rheometer setup for this series of experiments is equipped with more powerful light sources than those used in the previously discussed experiments in Section 3.1.1.2. Accordingly, the measurements of the silicone oils PDMS2-A$_2$ and PDMS3-A$_2$ are not comparable with these of the previous section. For PDMS-A$_2$, which was studied with both setups, the new setup leads faster programming and improved programming range. This generally shows the optimization potential of photoprogramming by tuning the intensity, wavelength and light source arrangement.

The rheological properties of PDMS0-A$_2$ mixtures are not studied in detail. Preliminary tests with samples of undiluted PDMS0-A$_2$ showed a compositional gradient during programming. This can be attributed to the strong reduction in light intensity along the light path due to absorption caused by the high anthracene concentration. Reliable rheological measurements on these samples could not be performed with our setup. In addition, PDMS0-A$_2$ is likely to be unsuitable as an additive for PDMS base oils. As mentioned earlier, it exhibits pronounced phase separation with a discontinuous phase consisting of large droplets (Figure 16). Since the continuous phase, in turn, predominantly determines the rheological properties of the material, an inefficient response to light is to be expected in this case.

The initial loss moduli of the PDMSX-A$_2$ mixtures increase respectively with, first, the fraction, and second, the molar mass of the respective additive. (Figure 18A) Both parameters increases the overall molar mass of the mixture. Accordingly, also the viscosity increases with both of these parameters (Figure 18B). The comparison between the loss modulus curves of the pure PDMSX-A$_2$ indicates, that the maxima approximately reach the same programming range of about 2-3 magnitudes. This matches to the similar estimated number of unreactive end-groups, which limiting the maximum achievable molar mass as described earlier (Table 3, Equation (14)). In contrast to the two other samples, the loss modulus of PDMS3-A$_2$ reaches no plateau after 90 min. This also contributes to the discrepancy between observed maxima. Moreover, it reveals the different programming kinetics being apparent from the slopes of the curves. Another hint of different programming kinetics is visible within the first 45 min by comparing PDMS-A$_2$ and PDMS2-A$_2$. The programming time is longer as the urethane content increases. The underlying mechanism needs to be studied more in detail to understand if interactions of the urethane group such as hydrogen bridges influence the chain mobility or the reactivity of the anthracene esters.
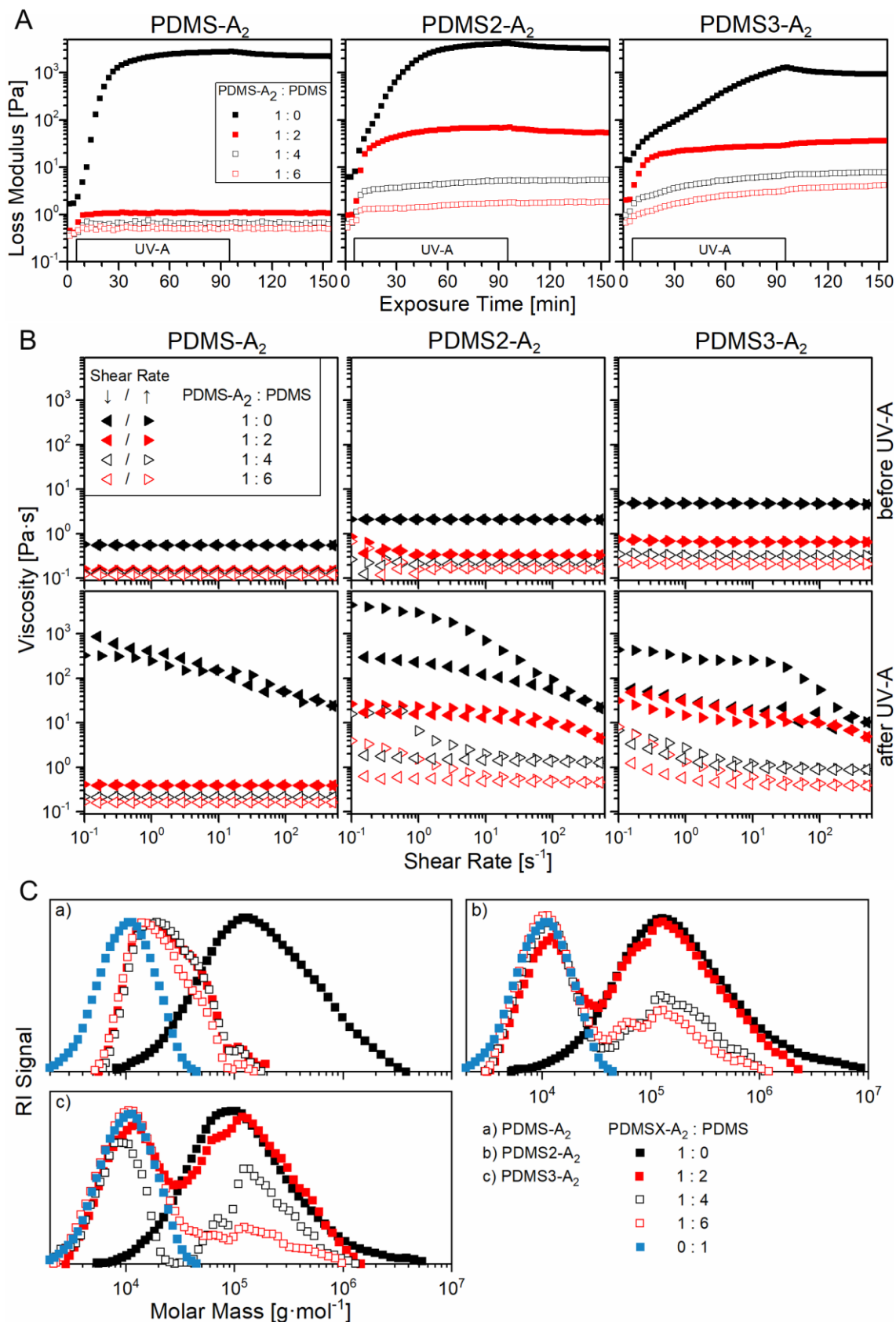
Figure 18: *The evaluation of the loss modulis upon UV-A radiation (A), respective flow curves (B) before (top) and after (bottom) UV-A radiation and SEC traces of the samples after the rheometer experiment (C) for mixtures of PDMS-A$_2$, PDMS2-A$_2$, PDMS3-A$_2$ with a PDMS base oil in the ratios 1:0, 1:2, 1:4, 1:6.*

All curves show a slight drop of the loss modulus after the radiation is switched off. This effect levels off within 30 min and different but constant loss moduli are reached for each sample. Mechanical chain decay of linear chains is not a suitable explanation for this finding, since in this case a continuous decrease or at least reaching the same constant value for all curves is expected. Another explanation is that inhomogeneities occur during photoprogramming. These can be caused by non-uniform illumination intensity, which was observed mainly at the edge of the glass plate. These inhomogeneities could then slowly decrease as a function of time due to mixing. Another hypothesis to explain this effect is, that occurring side reactions (see Section 3.1.1.3) lead to mechanically degradable crosslinks. Indeed, small, highly elastic and slightly jellylike inhomogeneous pieces of material were found in a few samples of the mixtures, indicating crosslinking processes during the test.

The range of programmability of the loss modulus and viscosity of the mixtures is found to be significantly smaller compared to the undiluted additives. The programming observed for the most mixtures does not exceed more than one magnitude. The highest programming ranges are found for the 1:2 mixtures of the blends of the urethane extended additives PDMS2-A_2 and PDMS3-A_2. This is also supported by the flow curves. Shear thinning behavior appears at viscosities above $\gtrsim 10^1$ Pa·s. Pseudoplastic behavior is typical for polymer melts as the chain orients along the direction of the shear force in dependency of the applied force (see Section 1.3). Some curves show a hysteresis, occurring rather randomly than in relation to the level of viscosity, the shear rate or the urethane content. The repetition of single measurements (not shown) emphasized the randomness of the appearance of these artefacts. This leads to the conclusion that they are caused by sample inhomogeneities and do not represent time dependent viscosity.

The molar mass distribution of the mixtures after radiation confirms the assumption, that the range of programmable rheological properties is connected with a fraction of higher molar masses chains. This high molar mass fraction after radiation appear as a broad peak showing a maximum around 10^5 g·mol^{-1}. It is found in pure and undiluted functional additives, its fraction decreasing accordingly to the extent of dilution. Only a small high molar mass fraction is found for mixtures of PDMS-A_2, which is evident by shoulders of the corresponding peaks. The observation is in line with the relatively low programming range. Nevertheless, dimerization is completed after the applied radiation time in all cases, as confirmed by ^{1}H-NMR analysis (Table 4).

Table 4:   *Conversion of the dimerization (DoD) of the samples after the rheometer experiment for mixtures of PDMS-A$_2$, PDMS2-A$_2$, PDMS3-A$_2$ with the PDMS base oil in the ratios 1:0, 1:2, 1:4, 1:6 analyzed by ^{1}H-NMR spectroscopy.*

PDMSX-A$_2$	PDMS base oil	DoD
[wt fraction]	[wt fraction]	[%]
1	2	0.96
PDMS-A$_2$ 1	4	0.95
1	6	0.96
1	2	0.95
PDMS2-A$_2$ 1	4	0.97
1	6	0.96
1	2	0.96
PDMS3-A$_2$ 1	4	0.93
1	6	0.95

This suggests, that the formation of chain-extended, high molar mass polymer is suppressed in the case of PDMS-A$_2$ mixtures, even though the course of dimerization is comparably advanced. A possible explanation is a dilution effect promoting the formation of macrocyclic structures.[131] Assuming that the light triggered reaction only occurs in the continuous phase, and considering the fact that the anthracene containing additive concentrates in the discontinuous phase, enhanced ring formation is a plausible explanation. In addition, the lower chain length of the PDMS-A$_2$ may contribute to the increased cyclization probability. Cyclisation side reactions may also explain the shoulder visible in the SEC data of mixtures of PDMS-A$_2$ by a local maximum around $4\text{-}5 \cdot 10^5$ g·mol^{-1}.

This initial evaluation shows that silicone oils functionalized with anthracene ester can act as an additive, providing a simple possibility to impart programmable viscosity to a PDMS base oil. It is evident that the molar mass of the anthracene-functionalized PDMS should exceed a certain threshold to prevent micron-scale phase separation. To accomplish this, urethane prepolymerization has proven to be a facile strategy to reduce the anthracene content. This was confirmed by an improvement in the programming range of rheological properties. The analysis highlights the factors that could further improve the limitations of the current system. On the one hand, anthracene ester synthesis could be optimized to achieve higher degrees of functionalization. Furthermore, material stability could be improved by applying oxygen-free conditions and light intensity distribution could be optimized to ensure more uniform programming. An improvement in phase compatibility can be achieved by synthesizing PDMS blocks with higher molar mass. Finally, it should be considered whether a suitable choice of

light sources in terms of wavelengths or modification of the chromophore improves the switching properties.

3.1.3 Summary of Chapter 3.1

The first part of this work demonstrates how the viscosity of a PDMS-based lubricant material is programmed within a certain range by UV-light-triggered dimerization of anthracene ester groups attached to the ends of the respective polymer chains. While dimerization by treatment with UV-A is nearly complete leading to a strong increase of viscosity, the backreaction by UV-C converts only around a tenth of dimers leading to a smaller but still significant decrease of viscosity. Moreover, prolonged UV exposure and oxygen presence during the rheological experiments damage the anthracene moieties, causing a decline of programming range over repeated switching cycles. However, potential to overcome this issue is indicated as these sidereactions are not observed upon long term UV-A exposure in the absence of oxygen. Furthermore, thermal cleavage is demonstrated as an alternative reprogramming method that fully restores initial rheological properties of the material. Slightly incomplete functionalization of PDMS chain termini with anthracene moieties (DoF) as well as the incomplete dimerization upon UV-A radiation (DoD) limit the maximum achievable molar mass since the chain extension of the bifunctional PDMS chains follow the rules of step-growth polymerization. Nevertheless, the range of programmable viscosity of the analyzed PDMS-based lubricant is demonstrated to exceeds two orders of magnitude. The fine-tuning of the programmable rheological properties is achieved by either mixing mono- and bifunctional silicone oils or blending the bifunctinal silicone with a native PDMS base oil. Good phase compatibility between the functional additive and the base oil is given, when the ratio between the PDMS block to the chain termini or dimer domains exceeds a certain value as exemplarily demonstrated for a bifunctional linear silicone of a molar mass of $M_n \gtrsim 8$ kg·mol^{-1}. The strategy employed to simultaneously increase precursor molar mass and reduce anthracene ester and dimer domains through urethane pre-extension is shown to improve the range of programmable rheological properties. However, it increases the programming time of the blends.

The anthracene functionalized PDMS are useful for the intention to flatten the Stribeck curve, which is beneficial for selected lubrication applications. This in turn mitigates material and energy loss effects. This first contribution, of course, only serves as an initial assessment of the light-programmable PDMS in the context of a lubricant. Further material optimization and tribological measurements of the functional silicone oil are necessary to evaluate the potential of this material as a lubricant. An example of this is the evaluation of the material stability under high shear loads. The DoF may be improved by testing new esterification/functionalization strategies with the chromophore, and the DoD by modifying the chromophore and analyzing the best light specifications such as wavelength and intensity. The phase compatibility of the

mixtures, and presumably also their rheological performance, has the potential to be improved by individual synthesis of PDMS precursors with higher molar masses. Furthermore, future work should determine the influence of the triggered viscosity change on the possibility of altering the coefficient of friction for typical lubrication films a thickness of about $h \leq 10$ µm. In this context, it is expected that the thin films are beneficial to decrease the switching time and improve the homogeneity of the programming process.

3.2 Spiropyran Copolymers

In this work, the RAFT copolymerization of spiropyran acrylates (SPA) is used as grafting-from approach for the fabrication of light-responsive polymeric surfaces. The yielded responsive material is suggested to enable programmable friction. The grafting-from polymerization strategy profits from the controlled character of the RAFT method for two reasons. First, the growing polymers anchored on the surface of the substrate are close to each other and therefore benefit from a low density of surface radicals, thereby reducing radical side reactions. Second, RAFT typically yields polymers with a narrowly distributed molar mass. Both criteria are desired in order to obtain high polymer densities thus enable good frictional properties (see 1.6.2.2).

The SPA polymerization conditions are optimized in in two steps. The first part in Chapter 3.2.1 focusses on the polymerization of SPA in solution. It deals with the investigation of the influence of visible light on the polymerization process and the optimization of reaction conditions for a dissolved polymer system. The conditions evaluated there must then be complemented by further optimizations in the second Chapter 3.2.2, which consider mechanistic implications arising from the surface-bound polymerization centers of a grafting-from approach. Accordingly, the second part deals with synthesis conditions and surface analysis of the grafting-from process. The applied grafting-from technique uses additional dissolved sacrificial CTA (see Chapter 1.4). This method, better known as CTA-shuttled RAFT, improves the polymerization of surface-bound polymer by additionally mediation via transfer reactions with dissolved polymer.[21]

Note: The sole term 'spiropyran' (SP) is used within this section including both photoisomers. The particular isomers are referred as either 'SP isomer' or 'MC isomer'.

3.2.1 Light-Dependent Copolymerization

The copolymerization of polar monomers with spiropyran (SP)-containing monomers aims to match the affinity to polar solvents with the photoswitchability of the SP unit in the desired polymer. It should be noted that SP is non-polar and therefore the solubility of an SP-containing copolymer in a polar solvent is expected to decrease with increasing SP content. Furthermore, it is conceivable that the extent of a macroscopic property that can be switched by light depends on the SP content. Accordingly, the possibility to vary the SP monomer feed is an important tool to tune the properties of the obtained copolymers and an important aspect of the copolymer syntheses in this chapter. Literature, however, indicates challenges for the direct copolymerization of SP monomers at higher contents using RAFT polymerization (see Section 1.6.1.2). This section discusses specific challenges found for the copolymerization of spiropyran acrylates (SPA) and systematically analyses their origin in order to optimize the copolymerization conditions in solution.

The assessment of the homopolymerization of 2-hydroxyethyl acrylate (HEA) with and without presence of 11 mol% non-polymerizable spiropyran propyl ester (SPP) (Scheme 15, middle) shows whether challenges for SP copolymerization originate from the polymerization kinetics of the SP-functionalized monomer or are related to interactions of the bare SP moiety with the growing polymer chain. The experiment is conducted both under VIS radiation and in the dark, in order to additionally answer for the latter hypothesis whether the two photoisomers SP and MC interact differently with the growing polymer chain. UV/VIS spectroscopy confirms that the model spiropyran (SPP) compound is comparable to the SP monomer in terms of light-responsiveness (Figure 19).

Condition	SPP	SPA	VIS
i.i)	✗	✗	✗
i.ii)	✓	✗	✓
i.iii)	✓	✗	✗
ii.i)	✗	✓	✓
ii.ii)	✗	✓	✗

SPP

SPA

PHEA

i)

ii)

PHEA$_x$SPA$_y$
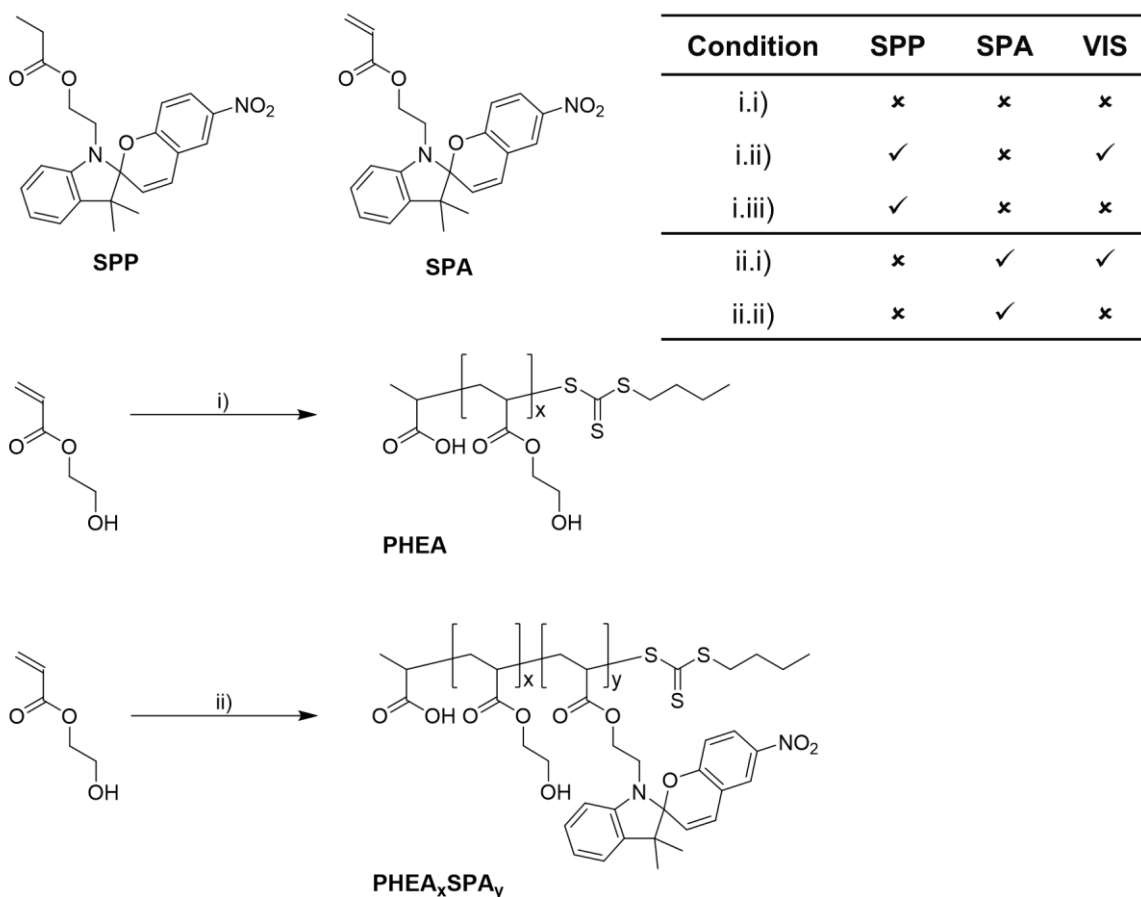
Scheme 15:   The homopolymerization of HEA (mid) and copolymerization of HEA with SPA (bottom) under the influence of SP moieties and VIS. Besides conditions mentioned in the table, all reactions were carried out with BTPA (CTA), AIBN, DMSO at 65 °C. SPA concents are varied between 5, 10 and 25 mol%.
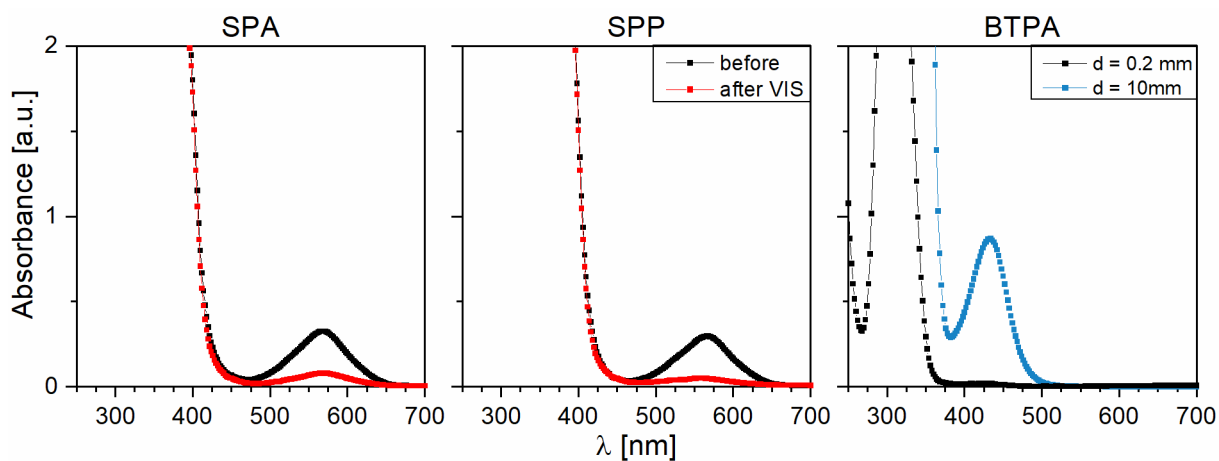
Figure 19:   UV/VIS spectra of SPA, SPP and BTPA.

Figure 20A shows the results of the ^{1}H-NMR analysis in a first order kinetic plot together with the associated SEC data at defined polymerization times. Three olefinic protons of the acrylate are apparent as signals a, b and c in Figure 21. Their intensity (I^a, I^b, I^c) relative to the intensity of an aromatic internal standard (I_{St}) during the polymerization enables estimation of the conversion X and monomer concentration $[M]_t$ at the known standard concentration $[St]$ as shown by Equation (18). Overlapping of signals c and o are corrected according to Equation (19).

$$X = 1 - \frac{[M]_t}{[M]_{t=0}} \; and \; [M]_t = \frac{I_t^a + I_t^b + I_t^c}{I_t^{St.}} \cdot [St.] \qquad (18)$$

$$I_t^c = I_t^{oc} - I_t^o = I_t^{oc} - \frac{I_t^g + I_t^h + I_t^i + I_t^j + I_t^k}{8} \qquad (19)$$

The homopolymerization of HEA in the absence of SPP reaches a conversion of 65 % after 6 h and has a reaction rate constant of $k_{HEA} = (49 \pm 1) \cdot 10^{-6}$ s^{-1}. In contrast, the HEA homopolymerization carried out in the presence of SPP and VIS reaches a comparable conversion of 76 % only after 48 h revealing a significantly reduced reaction rate constant of $k_{HEA/SPP} = (8.8 \pm 0.6) \cdot 10^{-6}$ s^{-1} (Figure 20A). The molar mass shows a linear increase with the conversion. However, final dispersity of Đ < 1.5 indicate only a moderate reaction control. Interestingly, no significant polymerization occurs in the presence of SPP, when the same reaction is carried out in the dark. This indicates indeed that the chromophore interferes with the polymerization in a photo-switchable manner. Considering, that VIS shifts the isomer equilibrium towards the SP isomer, the results suggested that it is the merocyanine isomer (MC) which interferes with the mechanism of radical polymerisation (Scheme 5B, Figure 19). The photoinifter-mechanism of BTPA (see Chapter 1.4), which may in principle also serve as explanation for the observed light dependency of the polymerization, is excluded to fully explain the light-depended polymerization results as described below. The absorption band of BTPA at 375-500 nm is attributed to the n→π* transition (Figure 19).[132] Previous studies demonstrated this transition to promote homolytic photocleavage thus conduct a polymerization upon exposure to blue light.[133] Consequently, BTPA photolysis in the presence of VIS may act as an additional radical source. However, this cannot explain the fact that the polymerization of HEA is inhibited in the dark. Experiments on free radical copolymerization, in which the photoinifer mechanism does not occur due to the absence of BTPA, support this conclusion. Also in this case, a monomer mixture containing 10% SPA and 90% HEA shows no conversion in the dark, but is polymerizable in the presence of VIS after 48 hours with 96% conversion.
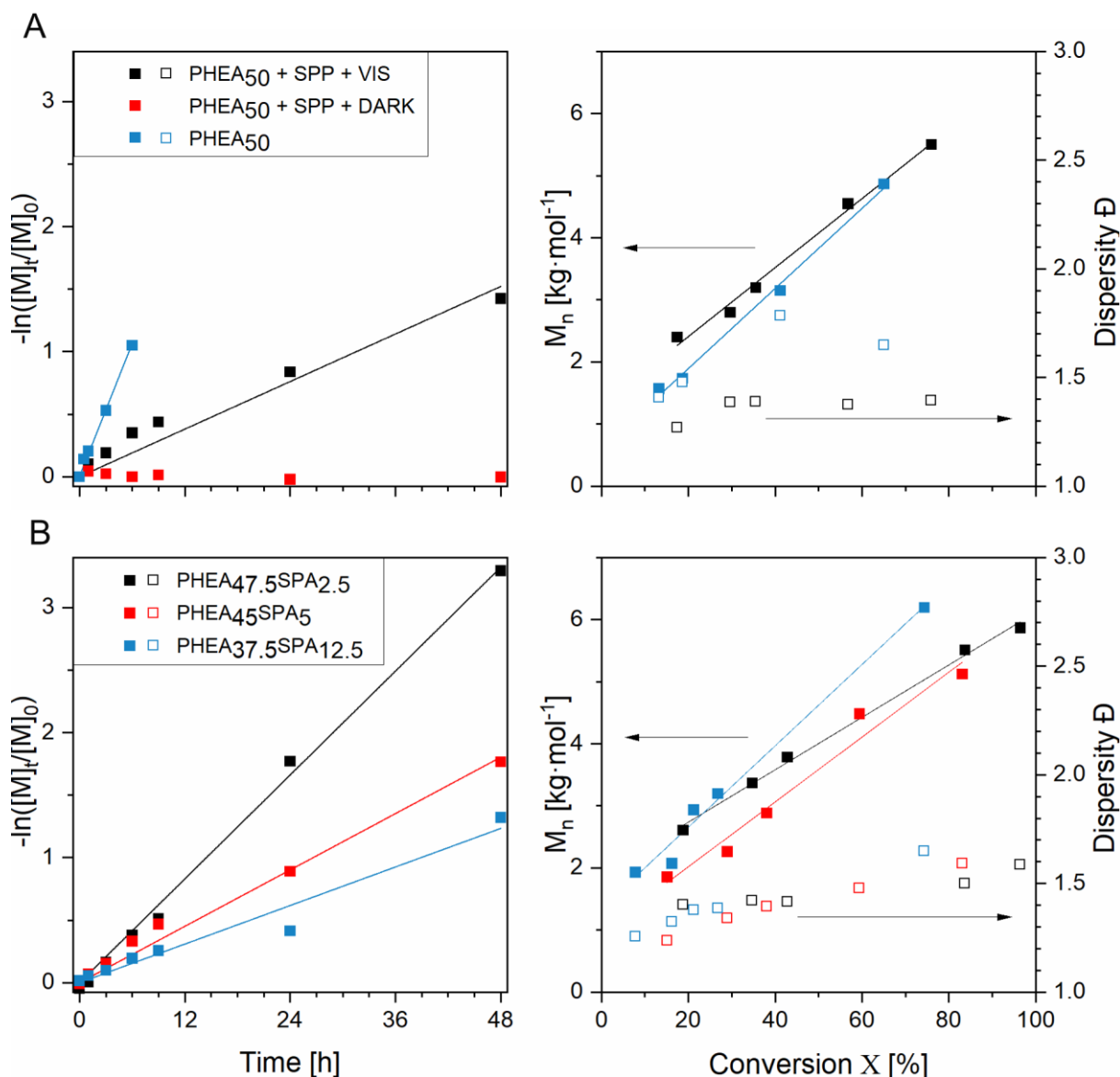
Figure 20:   *First order kinetic plots (left) and the dependence of experimental molar mass and dispersity on the conversion (right) for the homopolymerization of HEA in absence or presence of SPP and VIS (A), and the copolymerization of HEA and SPA at different ratios (B).*

The RAFT copolymerization of SPA with HEA leads to comparable results as demonstrated by the following set of experiments. Here, SPP is replaced by the SPA monomer (Scheme 15, Figure 20B). When VIS is switched on, good conversions of are reached within 48 h. The conversions slightly decrease with the SPA feed ratio, which is attributed to the dependency of the reaction kinetics on the SPA content. The first-order kinetic plots show a linear trend for all monomer compositions and the corresponding reaction rate constants are summarized in Table 5. They show that the reaction rates decrease with increasing SPA content. ^{1}H-NMR spectra of the purified polymers verify successful polymerization of SPA by the aromatic signals g', h', i', j', k' and o' attributed to the protons of the chromophore
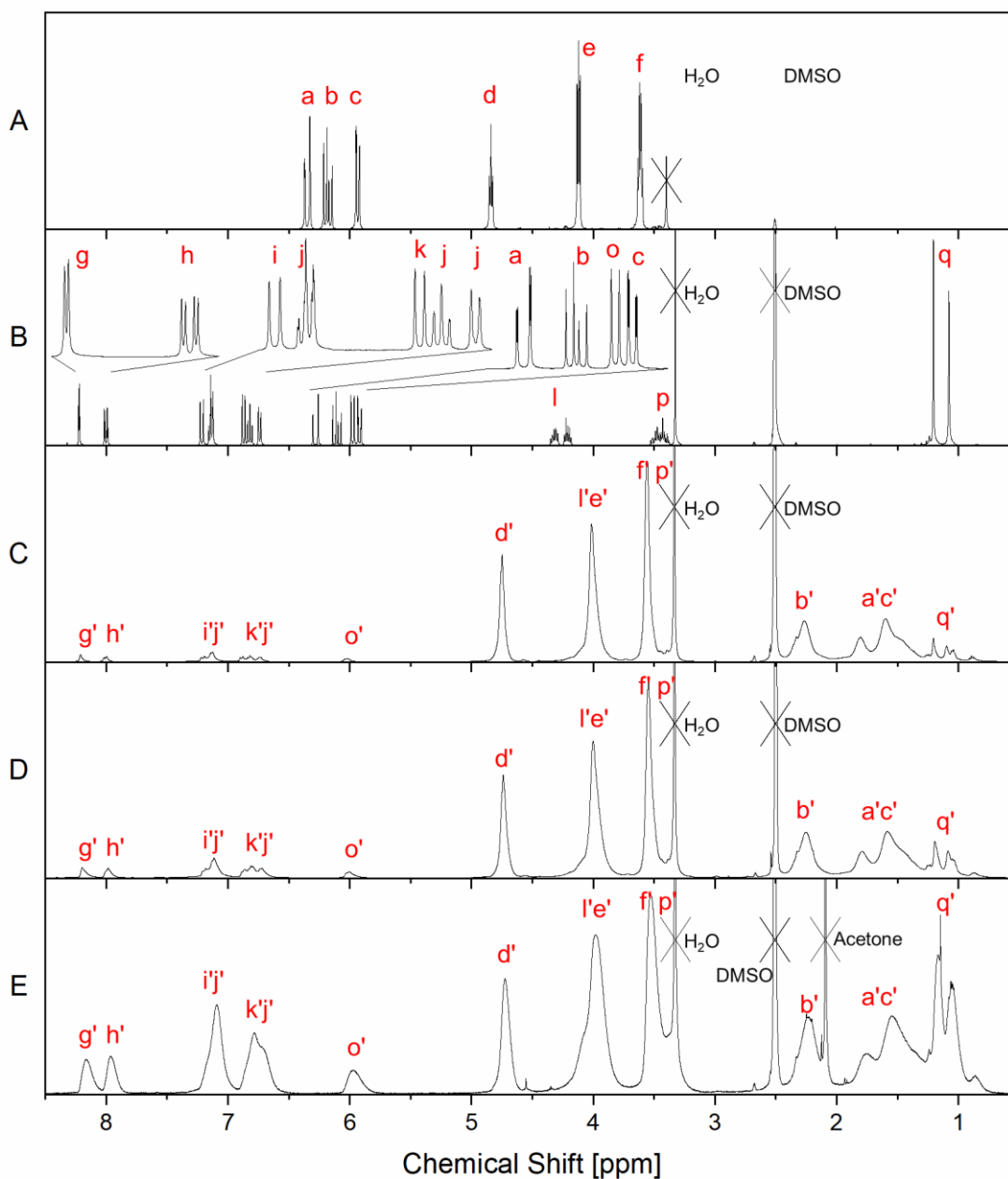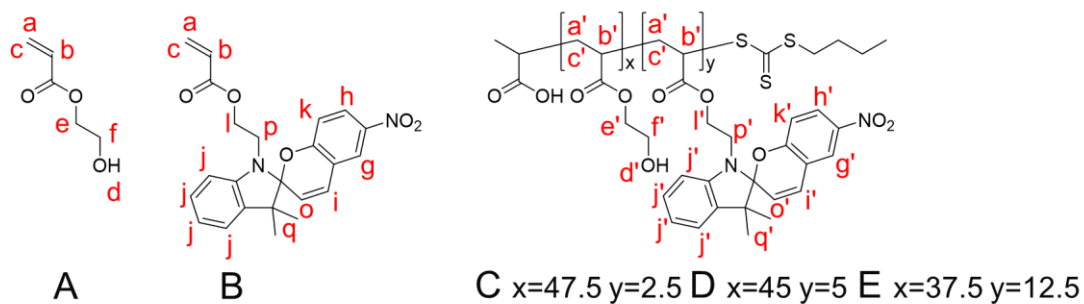
Figure 21: ¹H-NMR spectra of HEA (A), SPA (B), and PHEA$_x$SPA$_y$ copolymers (C-E) with monomer feed ratios of (C) x = 47.5 y = 2.5, (D) x = 45 y = 5, (E) x = 37.5 y = 12.5. The ¹H-¹H-COSY spectrum shown in Figure 34 (see appendix) supports the assignment of the signals for (B) SPA.

$$SPA_y = \frac{I^{g'} + I^{h'} + I^{i'} + I^{j'} + I^{k'} + I^{o'}}{I^{l'e'}} \cdot \frac{2}{9} \qquad (20)$$

Table 5:   Results of the thermally initiated RAFT copolymerization of HEA and SPA in solution and under the influence of VIS.

Monomer Feed		Polymerization		Purified Polymer			
HEA	SPA	k	$X_{t=48\,h}$	SPA_y	M_n	M_w	Đ
[eq.]	[eq.]	$[10^{-6}\,s^{-1}]$	[%]	[%]	$[kg \cdot mol^{-1}]$	$[kg \cdot mol^{-1}]$	
47.5	2.5	19.2 ± 0.4	96	4.7	7.2	10.5	1.45
45	5	10.4 ± 0.4	83	9.2	8.9	13.0	1.46
37.5	12.5	7.1 ± 0.5	74	24.5	7.3	10.6	1.45

(Figure 21). The SP content of the polymers calculated by Equation (20) is almost identical to the monomer feed ratio (Table 5). Figure 20 displays the linearly increasing molar mass with the conversion. SEC analysis of the purified polymers show the characteristic monomodal size distribution (Figure 22). Nevertheless, determined dispersities indicate only moderate reaction control (Table 5, Figure 20B). Tiny differences between the SEC results from samples of the reaction solution (Figure 20B) and the purified polymer (Table 5) are apparent and result from the purification step, in which dissolved molecules below the pore size of the dialysis membrane are removed.
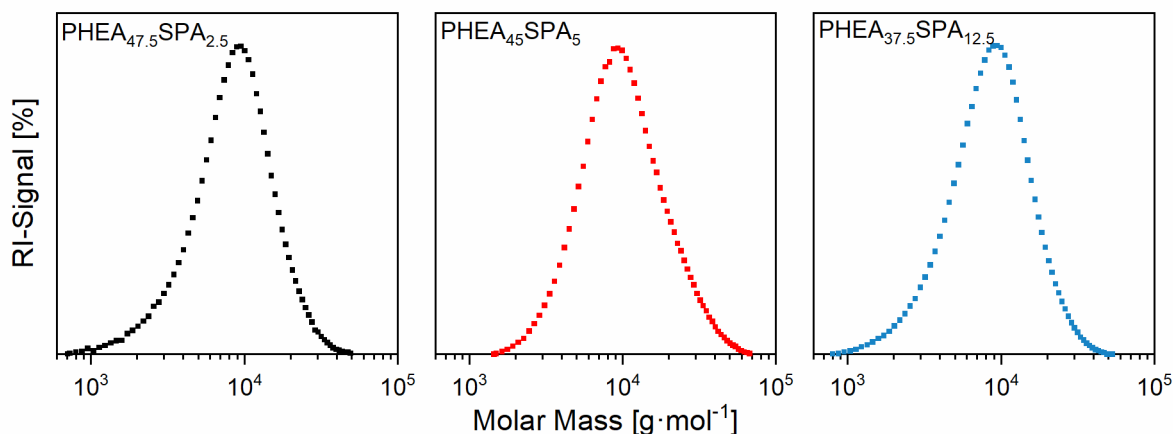
Figure 22:   SEC traces of PHEA$_{47.5}$SPA$_{2.5}$, PHEA$_{45}$SPA$_5$, PHEA$_{37.5}$SPA$_{12.5}$

A very different picture emerges for polymerizations carried out in the dark. Only very low conversions of < 25 % are settled after 48 h (Figure 35 in the appendix). Similar to the polymerization in the presence of SPP described above, the photoisomer equilibrium is suggested to be the cause of the light dependence of the polymerization. Also in this reaction, VIS shifts the equilibrium towards the SP isomer, as shown by the disappearing peak at 500-625 nm in the UV/VIS spectrum in Figure 19, and thus enables polymerization.

In conclusion, SP inhibits the RAFT polymerizations in the dark but not but not when radiated with VIS light. Additionally, the reaction rate of the copolymerization is linked to the SPA content. A suggested hypothesis to explain these observations is that, that radical side reactions occur between the growing polymer chain and either the aromatic nitro group or the aromatic hydroxyl function of SP.[134] Initial attempts were made to confirm this hypothesis. In a DFT simulation, the reaction energy of the attack of an acrylate radical at mentioned sites of the two spiropyran isomers was investigated (Scheme 18). The highest radical association energy is found for the radical attack at the aromatic oxygen atom of the MC isomer. This simulation result fits with the experimental observation that the inhibition occurs when the photoisomer equilibrium is shifted to the side of merocyanine in the dark. XPS studies of the O1s peak of SPP after heating with AIBN as a radical source aimed to find indications of structural changes in the case of radical side reactions with the SP moiety (Figure 36). They show that a shoulder appears at 531 eV. In this region, quinone structures are typically visible,[135] which may be an indication of such a side reaction. Nevertheless, it cannot be completely excluded that the differences between sample and control peaks are merely due to shifts between SP isomer and MC isomer resulting from sample preparation. The associated difference in binding energies at 533 eV may be due to the oxygen in the closed ether form of the SP isomer.[136] Likewise, the shoulder at 531 eV may be due to a higher fraction of negatively charged phenolic oxygen or a greater negative charge density on the oxygen of the nitro group in the MC isomer.[137] Accordingly, further investigations are necessary to clarify whether the concentration of the MC isomer and radical side reaction with this isomer are responsible for the light-dependent RAFT copolymerization of SPA.

The main objective of the investigation of this chapter, the development of a copolymerization protocol of hydrophilic monomers and a SPA monomer in high content, was achieved and can be tested accordingly for surface polymerizations in the following section.

3.2.2 Synthesis and Characterization Grafted Spiropyran Copolymers

The initial optimization of RAFT-based SPA copolymerization in solution, presented in Section 3.2.1, served to gain a general understanding of the system and establish basic criteria that must be met for successful polymerization of SPA. The next step in this section focusses on finding a suitable protocol for the surface-initiated RAFT polymerization to produce the desired SPA-containing brushes. For this, two different protocols are assessed in order to find the optimum process conditions: conventional thermally initiated RAFT (Chapter 3.2.2.1) and photo-induced electron/energy transfer (PET-)RAFT (Chapter 3.2.2.2).

The initial focusing on graft homopolymerization of selected polar monomers (without SPA) was made to improve the experimental throughput, since SPA strongly slows down the polymerization kinetics (see Chapter 3.2.1). In addition, SPA requires complex synthesis and purification, which so far is only capable of providing a small amount of pure monomer. In the next step, the grafting conditions determined in the series of homopolymerization experiments is evaluated with respect to the inclusion of SPA as a comonomer with the aim of eventually obtaining a photoresponsive polymer surface layer.

Both polymerization initiation methods discussed in Chapter 3.2.2.1 and Chapter 3.2.2.2 share the same surface modification protocol to yield CTA-equipped Si wafers as illustrated in Scheme 16. The wafers were chosen as model substrates due to their very smooth surface. It enables the detection of very thin organic layers by analytical methods such as AFM or ellipsometry. The surface of the wafer is activated with oxygen plasma. Silane chemistry using APTES is applied to anchor primary amines on the surface prior to the attachment of the CTA (BTPA) by EDC-coupled amidation. Two different modification protocols are applied that differ from each other in the silanization step. The first protocol treats the surfaces with APTES from a gaseous phase (CVD) and the second protocol uses solvent-borne chemistry. Finally, the grafting-from polymerization allows to synthesize the desired polymer layer. The different polymerization setups illustrated in Scheme 16 by A and B are explained in the following two subchapters.
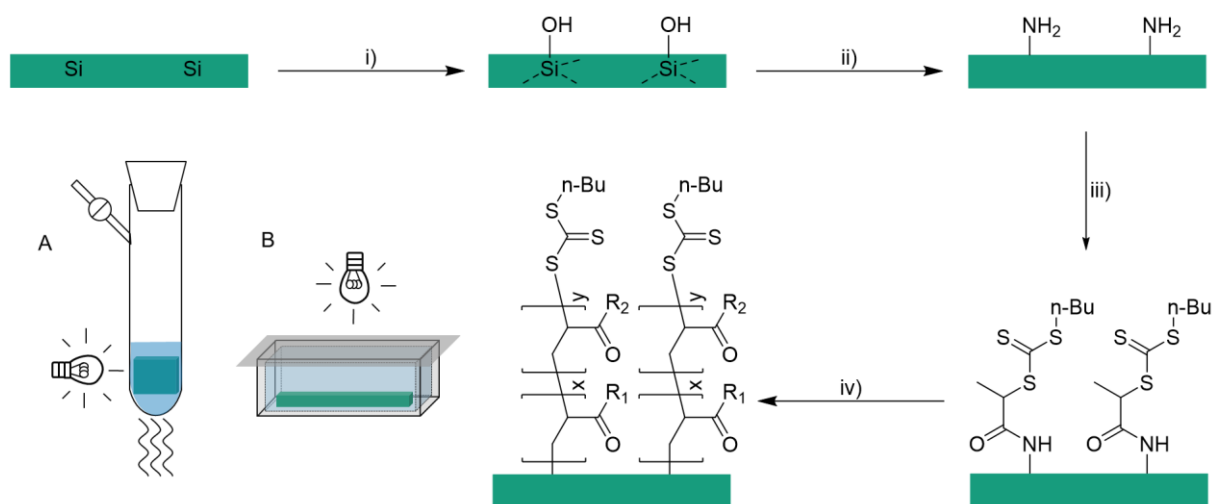
Scheme 16:   The synthesis of grafted copolymer from Si wafers by subsequent oxidation, amino-functionalization, amidation with CTA, followed by the CTA-shuttled RAFT copolymerization. i) O_2 plasma; ii) Either modification 1) APTES, NH_4OH, 70 °C, 2h (CVD) or modification 2) APTES (2 vol%), EtOH, RT, 20h; iii) BTPA, EDC·HCl, NEt_3, DMF, RT, 18 h; iv) Polymerization setup A) SPA/HEA, AIBN, BTPA, DMSO, VIS, 65 °C or setup B) SPA/HEA, EoY, AscA, BTPA, DMSO, VIS_{Green}, RT.

3.2.2.1 Thermally Initiated RAFT

Scheme 16 illustrates the grafting-from approach in which the CTA-modified substrate is submersed into the RAFT polymerization solution. The applied method is called CTA-shuttled RAFT and enables simultaneous growth of the polymer in solution and on the surface of the substrate. The dissolved CTA (BTPA) mediates the radical transfer between these reaction sites. The free polymer, being additionally formed when using this method, is accessible for wet analytical methods. It is resembles the immobilized graft polymer since controlled polymerization conditions are used. The applied polymerization conditions are derived from a process established by Akarsu et al. who demonstrate a successful grafting of TRISAM brushes from Si wafers and silicone stamps.[148]

Table 6 summarizes the conducted grafting-from experiments. It shows the variation of the following parameters aiming to optimize the synthesis of a grafted polar homopolymer. First, the functionalized CTA wafers, generated by the two different substrate modification protocols, are tested. Second, a selection of commercially available polar monomers is used, which are shown in Scheme 17. The third varied parameter is the targeted molar mass. For this, only the amount of dissolved CTA (n_{CTA}) is important, as the amount of surface-bound CTA is negligible. The following highly simplified model calculation verifies this claim. The whole surface area of the cuboid substrate (10×10×1 mm³, A_{total} = 240 mm) is covered with a circular model molecule (r=0.15 nm, A_{MM} = 0.071 nm). The amount of the model molecule is n_{MM} and it represents the surface-bound-CTA. The relative amount of surface bound CTA in the typical polymerization setup is very low as expressed in Equation (21). The real ratio of surface bound CTA is even lower, as the following assumptions overestimate the calculated value. No spaces between circular model molecules are considered, complete surface coverage is assumed, and the size of the model molecule is more in the range of a water molecule, so the actual size of the CTA is underestimated.

Table 6:   *Summary of varied parameters and results for the grafting-from polymerization using thermally initiated CTA-shuttled RAFT. Conversion and molar masses are determined by ^{1}H-NMR spectroscopy and SEC, respectively. [a] Estimated after a reaction time of 48 h. All other results are given after a reaction time of 20 h. [b] Polymerization conducted in DMSO, all other polymerizations are carried out in mixture of dioxane and H_2O.*

Modification	Feed		Polymer			
	M		X	M_n	M_w	Đ
		[eq.]	[%]	[kg·mol^{-1}]	[kg·mol^{-1}]	
1	TRISAM	200	97	32.7	43.1	1.33
2						
1	TRISAM	600	80	47.7	76.9	1.61
1	HEA[b]	50	94	6.1	8.4	1.37
1	HEA	200	98	37.3	52.9	1.41
1	HEA	600	91	28.4	56.8	2.00
1	NAM	200	99	7.3	10.7	1.31
1	DMAM	200	96	7.8	17.2	2.19
1	OEGA	200	93	9.1	14.5	1.59
1	TRISAM+ SPA	180+ 20	67[a]	12.5[a]	21.1[a]	1.68[a]

| TRISAM | HEA | NAM | DMAM | OEGA | SPA |
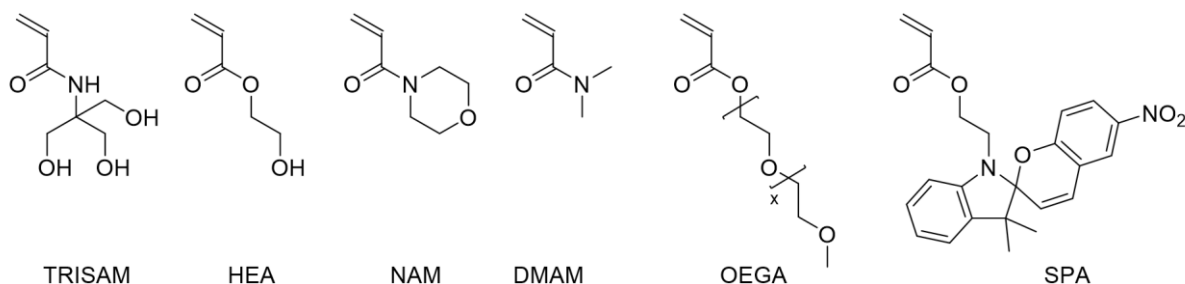
Scheme 17:   *Tested polar monomers for thermally initiated CTA-shuttled RAFT grafting-from polymerization. (see Table 6).*

$$\frac{n_{MM}}{n_{MM} + n_{CTA}} = \frac{\frac{A_{total}}{A_1 \cdot N_A}}{\frac{A_{total}}{A_1 \cdot N_A} + n_{CTA}}$$

$$= \frac{\frac{240\ mm^2}{0.071\ nm^2 \cdot 6{,}022 \cdot 10^{23}\frac{1}{mol}}}{\frac{240\ mm^2}{0.071\ nm^2 \cdot 6{,}022 \cdot 10^{23}\frac{1}{mol}} + 5 \cdot 10^{-5}\ mol} \approx 10^{-4} \tag{21}$$

The conversions of the conducted polymerizations shown in Table 6 are calculated by the ratio between the intensities of the olefinic monomer signals c, b and d to the aliphatic polymer signals c', b' and d' after the polymerization. Equation (22) expresses the determination according to the signals shown in the ^{1}H-NMR spectra of Figure 23. The methin proton of the polymer backbone (b') overlaps with the solvent peak (DMSO) in the samples of NAM (C) and DMAM (D) and is therefore not taken into account (Equation (23)).

$$X = \frac{I^{b'} + I^{c'} + I^{d'}}{(I^{b'} + I^{c'} + I^{d'}) + (I^b + I^c + I^d)} \qquad (22)$$

$$X = \frac{\dfrac{I^{c'} + I^{d'}}{2}}{\dfrac{I^{c'} + I^{d'}}{2} + \dfrac{I^b + I^c + I^d}{3}} \qquad (23)$$

The conversions of all homopolymerizations reach high values. Additionally, high molar masses are found in the SEC supporting the polymer formation. Good reaction control is found for the polymerization of TRISAM and NAM at M = 200 eq. as indicated by dispersities of ~ 1.3 (Figure 24, top). The dispersities of PHEA are rather low in the cases of HEA = 50 and 200 eq. However, the molar mass distribution for M = 200 shows a small shoulder at higher molar masses, which is either caused by in-situ transesterification or radical side reactions (Figure 24, top) and was previously reported to occur in aqueous solutions.[138] The probability of radical recombination or chain transfer decrease with monomer concentration and therefore preferably appears at very high conversion. All other polymerization results show monomodal molar mass distribution of the synthesized polymer. The targeted degree of polymerization of 600 in the case of TRISAM and HEA as well as the polymerization of OEGA and DMAM leads to rather high dispersities and indicates bad reaction control. In the case of OEGA and DMAM, it can be assumed that the solvent is not suitable for very good reaction control. The worsening of reaction control at higher targeted molar masses can be explained by the decreasing mobility of the macro-CTA due to attachment to the growing polymer chain, which correspondingly reduces the chain transfer reactions and thus leads to poorer reaction control.
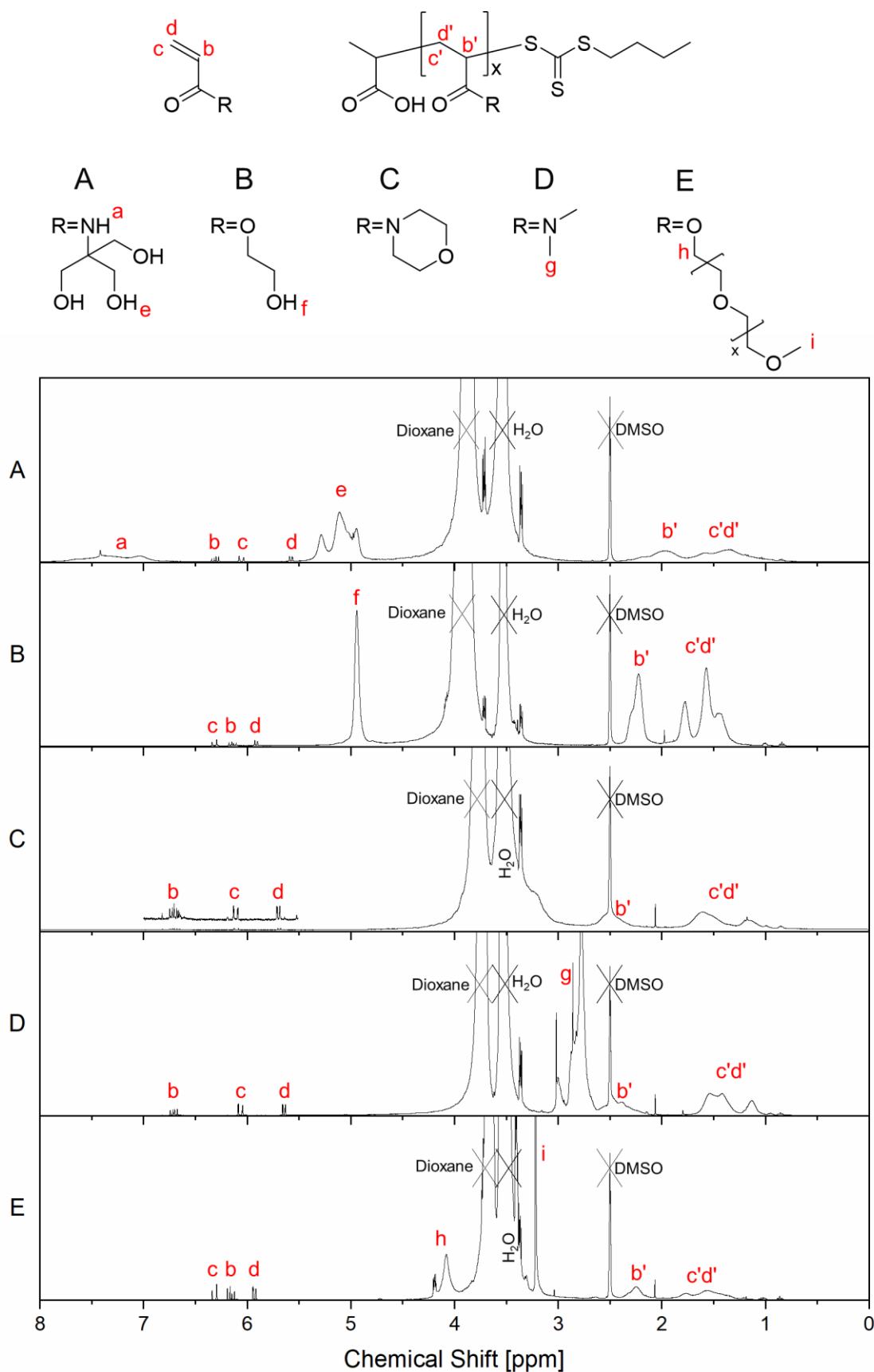
Figure 23: *1H-NMR spectra and corresponding chemical structures after CTA-shuttled grafting-from homopolymerization of TRISAM (A), HEA (B), NAM (C), DMAM (D) and OEGA (E).*

Figure 24 (bottom) summarizes the detected water contact angles (CA) of the wafers after each modification step including the polymerization. The CA of a fresh, oxygen plasma treated Si wafer shows a highly polar surface due to the polar oxide layer. Subsequent APTES modification increased the CA, indicating the successful binding of the silane and consequently amination of the surface (samples 2 and 13). The CA is higher for the surface after reaction with APTES in gaseous phase (sample 2, modification 1) compared to the silanization in solution (sample 13, modification 2). The CA further increases after amidation as indicated by samples 3 and 14. This demonstrates the successful binding of the rather hydrophobic CTA. The successful CTA modification is also apparent by the fact that grafting reactions from modified wafers can be carried out according to this synthesis protocol (see also Chapter 3.2.2.2). Since all the monomers used and the corresponding polymers are water-soluble and the CTA-modified surface is non-polar, a decrease in the CA value after polymerization is an indication of successful grafting. Polymerization of TRISAM resulted in a significant increase of surface polarity indicated by CAs < 30° (samples 4, 5 and 15). In the case of the grafting from surfaces according to modification protocol 1 (samples 4 and 5), the layer thickness analysis with AFM also clearly shows the presence of an organic polymer layer. Here, sample 5 shows a higher film thickness, which can be attributed to a higher molar mass of the bound polymer. Corresponding results of the SEC analysis are shown in Table 6. However, in the case of modification protocol 2 (sample 15), no polymer layer could be detected by AFM. The average measured layer thickness does not exceed the error margin of the method and shows a similar value as the substrate before polymerization (sample 3). Interestingly, both TRISAM polymerizations with targeted polymerization degree of 200 were carried out simultaneously and in the same reaction solution. Therefore, the difference between samples 4 and 15 can be clearly attributed to the nature of the surface. One possibility is that sample 14 has a lower CTA density and thus a poorer control is achieved on its surface. Since modification protocol 1 shows significantly poorer performance, the corresponding substrates were not used in any further experiments of this section. It should be noted that the inferior performance of modification protocol 1 is again confirmed by the results presented in Chapter 3.2.2.2. After polymerization with PHEA, PNAM, PDMAM and POEGA, little or no CA changes are observed, indicating corresponding changes in surface hydrophilicity. However, such a change is expected if a sufficiently dense layer of a water-soluble polymer is immobilized on the surface. AFM analysis confirms that there is no significant organic layer on the top of samples 6-11.

Further investigations are required to understand why polymer films are not detectable on the surfaces except for the polymerization of PTRISAM. It is possible that grafting itself does not occur, very low graft densities are achieved, or that the degree of polymerization on the surface is very low, i.e. that only oligomers are formed. The results could be explained by side reactions

at the surface and the failure of the shuttle mechanism. Interestingly, however, the polymer dispersities obtained with HEA and NAM indicate comparable good reaction control to that obtained after TRISAM polymerization. Nevertheless, no polymer layers are found on the wafer surface in these cases. In the thermally initiated grafting-from mechanism, the growing polymer chain must diffuse to the surface to initiate a growing chain on the surface. Therefore, it can be assumed that there must be good compatibility between the surface and the polymer, as well as a suitable solvent. It is therefore possible that compatibility issues explain why TRISAM is successfully grafted and the other monomers are not. Since TRISAM shows good grafting results and is thus suitable for the copolymerization experiments (see following paragraph), detailed tests with other solvents and polar monomers are unnecessary.
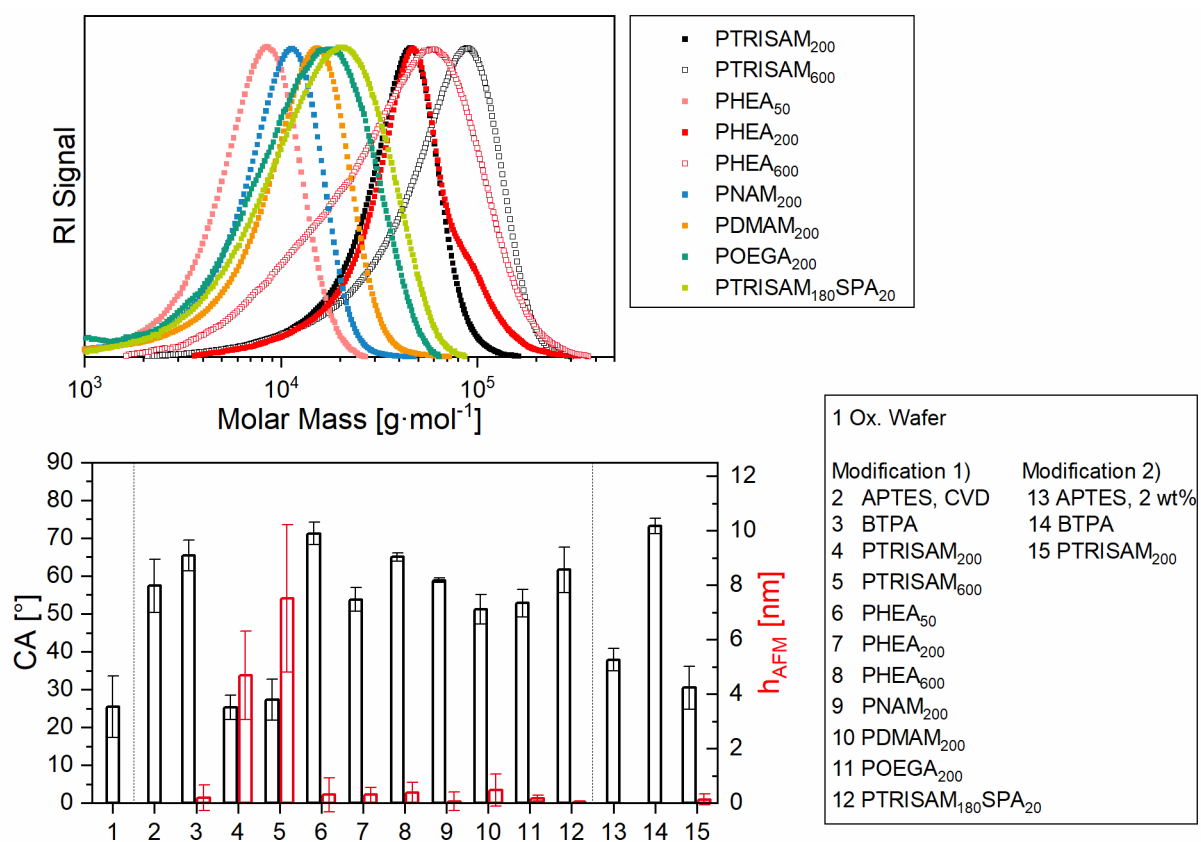
Figure 24:   *Molar mass distribution (top) and surface characterization including CA and film thickness (h) (bottom) after thermally initiated grafting-from RAFT polymerizations (Table 6).*

Graft copolymerization of SPA was tested using TRISAM as comonomer due to the good results discussed previously. Illumination during the polymerization was provided, considering the results described in Chapter 3.2.1. The conversion of each monomer as well as the overall monomer conversion was calculated according to the Equations (24) and (25) utilizing recorded ^{1}H-NMR spectra (Figure 25). It is based on the change in intensity of the olefinic acryl amide signals e and k and the olefinic acrylate signals f and l normalized to the non-superposed aromatic signals of the SP moiety a, b and d_2. The intensity of the superposed

peak ij is corrected by estimating the intensity of signal j to obtain signal i as shown in Equation (26).

$$X = 1 - \left(\frac{[M]_t}{[M]_{t=0}}\right) \tag{24}$$

$$[TRISAM]_t = \frac{I_t^e + I_t^k}{I_t^a + I_t^b + I_t^{d_2}} \cdot [St.] \; and \; [SPA]_t = \frac{I_t^f + I_t^i}{I_t^a + I_t^b + I_t^{d_2}} \cdot [St.] \tag{25}$$

$$I_t^i = I_t^{ij} - I_t^j = I_t^{ij} - \frac{I_t^a + I_t^b + I_t^{d_2}}{5} \tag{26}$$
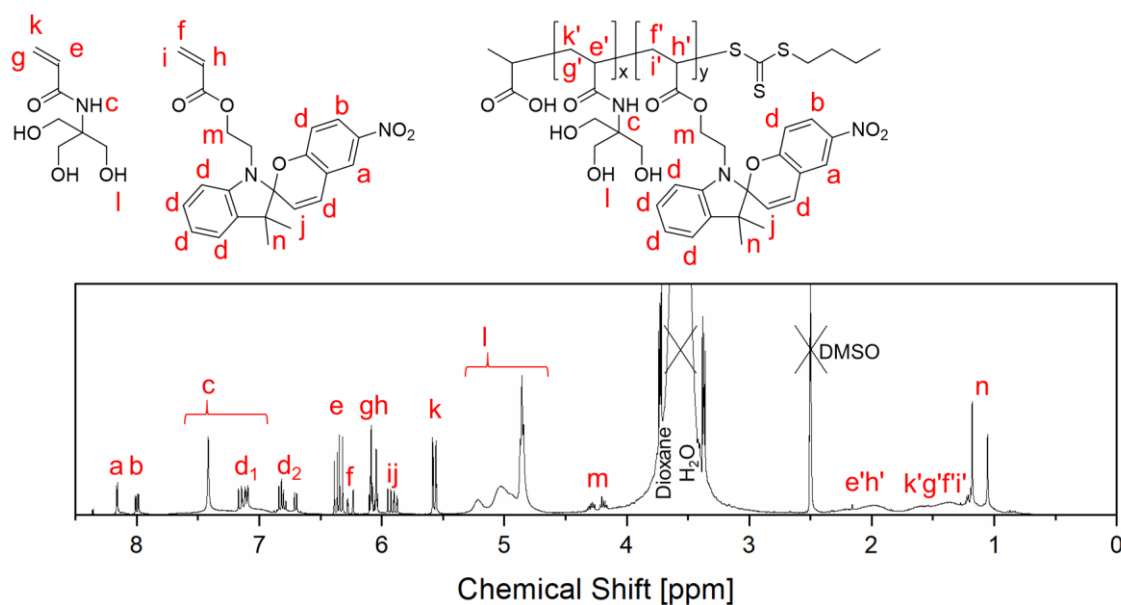
Figure 25: ¹*H-NMR spectrum of the copolymerization of TRISAM and SPA and assignment of the signals to the chemical structures.*

Table 6 shows the results of the copolymerization compared to the previously discussed results of the homopolymerization. It is evident that even after a reaction time more than twice as long as for the homopolymerization of TRISAM, no high conversion is achieved. Consistently, the SEC analysis of the polymer shows a lower molar mass. Furthermore, the molar mass distribution (Figure 24, top) exhibits a monomodal peak. However, the dispersity is significantly increased compared to the TRISAM homopolymerization with a similar targeted degree of polymerization. Thus, the addition of SPA to the polymerization feed shows the same characteristic changes to the homopolymerization as already discussed for the copolymerization of HEA with SPA in Section 3.2.1. The determination of the comonomer-specific conversions gives the values of $X_{TRISAM} = 68\,\%$ and $X_{SPA} = 56\,\%$, respectively. Together with the fact that the resulting polymer appears colored after purification, this allows confirming that SPA is incorporated into the polymer.

The CA value of the CTA-modified wafer is not significantly different after polymerization has been proceeded. However, it should be noted that the CA measurements in this case cannot

exclude the successful surface attachment of the copolymer because the SP unit is nonpolar. Due to the non-polar unit, it can only be expected that the SPA copolymer should exhibit a higher CA than the PTRISAM homopolymer. The exact deviation from the substrate prior to polymerization cannot be predicted with the given comparative samples. However, AFM analysis also indicates that no polymer layer is present on the substrate. Furthermore, no fluorescence could be seen under UV-A light. Therefore, it is concluded that the SPA copolymerization occurred only in solution and no significant chain propagation originated from the surface. Similar to the homopolymerization discussed previously, further experiments are needed to understand this result and determine what conditions are required for successful grafting of SPA using the thermally initiated RAFT process. In particular, the testing of different solvents to improve polymer-surface compatibility is suggested for this purpose.

Nevertheless, the approach was not elaborated further given the scope of this thesis, where the ultimate goal is to generate materials and investigate their switchable properties. An alternative synthesis strategy, PET-RAFT, presented in Chapter 3.2.2.2, leads to better results to obtain the desired copolymer surfaces. For this reason, the thermally initiated RAFT process was not elaborated further.

3.2.2.2 PET-RAFT

This chapter discusses the application of light-initiated PET-RAFT polymerization for the grafting-from approach of SP copolymers. The selected initiator system for this approach consists of Eosin Y and ascorbic acid (EoY/AscA), and works under the use of green light. Yeow et al. applied this system for polymerization in very small reaction volumes and emphasized its advantageous reaction conditions such as ambient temperature and oxygen tolerance.[139] It is a resource efficient approach that makes elaborate techniques such as degassing, Schlenk technique and controlled heating unnecessary. These simplifications compared to thermally initiated RAFT imply a greater potential to meet the demands of industrial manufacturing. In addition to this, the photoinitiator system is also useful for another reason. Pre-experiments on the thermally initiated copolymerization of HEA and SPA in solution revealed that the successful polymerization of SPA requires the aid of light due to the photochromism of SPA (see Section 3.2.1). Accordingly, the applied light can also be used for initiation, thus saving the sacrificial thermal initiator. The absorption spectrum of Figure 19 confirms that green light is suitable for this purpose, as it matches not only the excitation wavelength of the catalyst system, but also that of merocyanin to trigger the photoisomerization process.

The first Chapter 3.2.2.2.1 covers the optimization of the grafting-from homopolymerization of HEA adapting the reported EoY/AscA initiator system to the desired system of this work. Subsequently, the optimized synthesis is tested for the fabrication of copolymer surfaces with a varying SPA content followed by an assessment of the obtained copolymer surfaces regarding switchable physiochemical properties (Chapter 3.2.2.2.2).

3.2.2.2.1 The Grafting of PHEA from Si Wafers

A previous report described the EoY/AscA initiator system for the polymerization of a few polar monomers including HEA in water.[139] The homopolymerization conditions described in this paper have to be modified and optimized for the purpose of this work, because two new synthetic goals are to be achieved. On the one hand, the method will be used for a grafting-from approach and, on the other hand, it will be adapted for the copolymerization of SPA (see Section 3.2.2.2.2).

The first adjustment aims to find a suitable solvent that also dissolves SPA. Further modifications test the conditions of the surface grafting. In the second step, the two previously discussed wafer modification protocols are compared for the polymerization as they are expected to lead to different CTA densities (see Chapter 3.2.2.1). In the third step, the concentration of AscA is varied thereby tuning the previously reported optimal ratio[139] for the herein used setup. Since the shape of the reaction vessel and the corresponding interface to the air must influence the diffusion of oxygen into solution, this adjustment of the catalyst system is reasonable and is to be checked by this step. Finally, the targeted degree of polymerization is varied to investigate its influence on the thickness of the grafted polymer layer.

After the polymerization experiments, it was observed in all reaction solutions that the color and fluorescence of the photocatalyst employed vanished. In some samples, it was also noticeable that the viscosity of the solution was greatly increased. The increase in viscosity is evidence of successful polymerization, as it is due to the formation of high molar mass macromolecules at low dilution. Consistent with previous reports, the bleaching of the dye is attributed to the conversion of EoY to its leuco form and part of the oxygen-consuming catalytic cycle.[139]

Table 7 summarizes the screened parameters, conversions and molar masses. The conversions are analyzed by ^{1}H-NMR spectroscopy and calculated according to Equation (22) by the ratio between the signals assigned to the olefinic protons of the acrylate and the signals of the aliphatic protons of the polymer backbone. As a reference, a homopolymerization experiment was carried out in water. In this experiment, an almost complete conversion is achieved and the polymerization proceeds significantly faster than in the other media. However, the resulting dispersity is only moderately low. One possibility is that the reaction time is chosen too long. At high conversion rates, the mobility of the polymer-bound transfer agents may be limited due to the strong viscosity development, leading to a loss of reaction control. The loss of reaction control is also confirmed by the peak shape of the molar mass distribution, as the PHEA polymerized in water shows a shoulder at higher molar masses (Figure 26, bottom). This indicates that transesterification reactions or radical side reactions

such as chain transfer and recombination occur. The polymerization in DMF yields only a low conversion after 20 h and is thus not a suitable solvent to replace water for the intended copolymerization. In contrast, DMSO is a better alternative to water. After the selected reaction time, better conversion and higher molar mass were obtained compared to DMF. Yet, both values are not as high as in water. These results are in line with previous reports of EoY initiated PET-RAFT showing slow polymerization rates in DMF and faster reactions in case of water and DMSO.[140] Furthermore, low dispersity and monomodal distribution of the polymer peak in the SEC analysis indicate good reaction control of the reaction in DMSO.

Figure 26 (top) summarizes the results of the surface analytics after the grafting process. The grafting of PHEA from the surface increases the polarity thus lower CA are measured. A comparison of the samples whose reactions were conducted in different media (4-6) with the CTA-modified sample (3) indicate successful grafting of polymer from the surface after each reaction. Interestingly, even the small conversion in DMF is sufficient to subsequently detect a thin grafted PHEA layer on the surface. This is confirmed by the two thickness measurement methods, AFM and ellipsometry. The highest surface thickness is achieved by the polymerization in DMSO. Consequently, this solvent is used as an alternative to water for further experiments.

Table 7: *Summary of varied parameters and results for the optimization of PET-RAFT reaction conditions. Used amount of BPTA = 1 eq. and EoY = 0.018 eq. are maintained throughout all experiments. Conversion and molar masses are determined by ^{1}H-NMR spectroscopy and SEC, respectively.*

Modification	Feed			Polymer			
	HEA [eq.]	AscA [eq.]	Solvent	X [%]	M_n [kg·mol^{-1}]	M_w [kg·mol^{-1}]	Đ
1	200	1	H_2O	99	35.8	50.4	1.41
1	200	1	DMSO	66	19.3	25.6	1.33
1	200	1	DMF	10			
2	200		DMSO	86			
1	200	0.1	DMSO	28	8.7	11.3	1.30
1	200	0.5	DMSO	42	12.6	16.6	1.31
1	200	5	DMSO	85	29.0	39.2	1.35
1	200	10	DMSO	95	29.1	40.3	1.36
1	500	1	DMSO	15			
1	1000	1	DMSO	7			
1	2000	1	DMSO	8			

The results of the two independent thickness measurement methods AFM and ellipsometry show similar trends and thus confirm the presence of a polymer layer. However, a quantitative comparability of the values is not given due to the characteristics of the methods. Inaccuracies of the AFM analysis are mainly caused by the baseline correction during data processing and an incomplete removal of the organic layer at the sample preparation step (see Figure 30 and Chapter 5.1.1). Whereas the processing error causes either over- or underestimation, the preparation error only leads to underestimation. Values determined by ellipsometry are based on assumptions from a multi-layer model that includes the oxidized layer, the silane layer and an organic layer with the CTA. Furthermore, the overestimation of the polymer layers with this method is obvious by a comparison to the samples before the polymerization (1-3 and 10-11). It is visible that silanization of the wafer increases the layer thickness on the wafer by a few nm. This is attributed to the silane polymerizing rather than forming a monolayer. The bonding of the CTA via amidation does not significantly influence the film thickness.

Comparing the different surface modification protocols in terms of their influence on the surface polymerization, the following can be seen. The application of surface modification protocol 2 in the case of sample 12 shows low CA values and a significant film thickness in the AFM analysis, which generally confirms that grafting-from has taken place after polymerization. However, it can be seen that the polymer layer obtained is thinner than in the case of sample 5, which was prepared according to surface modification protocol 1. In addition, even higher conversions were achieved in the batch of sample 12, which theoretically should result in longer polymer brushes and thus a higher film thickness considering the use of similar surfaces. Interestingly, however, the opposite is observed. A possible explanation is that the CTA density of the substrates is different as a result of the two surface modification protocols. This may either affect the density of the grafting points or influence the reaction control on the surfaces during polymerization. However, the CA measurements show approximately the same value for all CTA-modified surfaces (see also Chapter 3.2.2.1), and thus are not suitable to confirm this hypothesis. Accordingly, it is proposed to apply further analytical methods such as XPS to compare the CTA density of the surfaces after the two modification protocols. In general, the results confirm that modification protocol 2 is disadvantageous compared to modification protocol 1 for the grafting-from approach. This is in line with the observations made in the case of thermally initiated polymerization (Chapter 3.2.2.1). Furthermore, the result shows that a targeted and systematic optimization of the surface functionalization is probably useful to further improve the surface polymerization and the obtained film thicknesses. Nevertheless, a detailed, targeted and systematic analysis of the CTA density and its influence on the surface polymerization is not further elaborated in the context of this work, as previously explained (see Section 3.2.2.2.2).
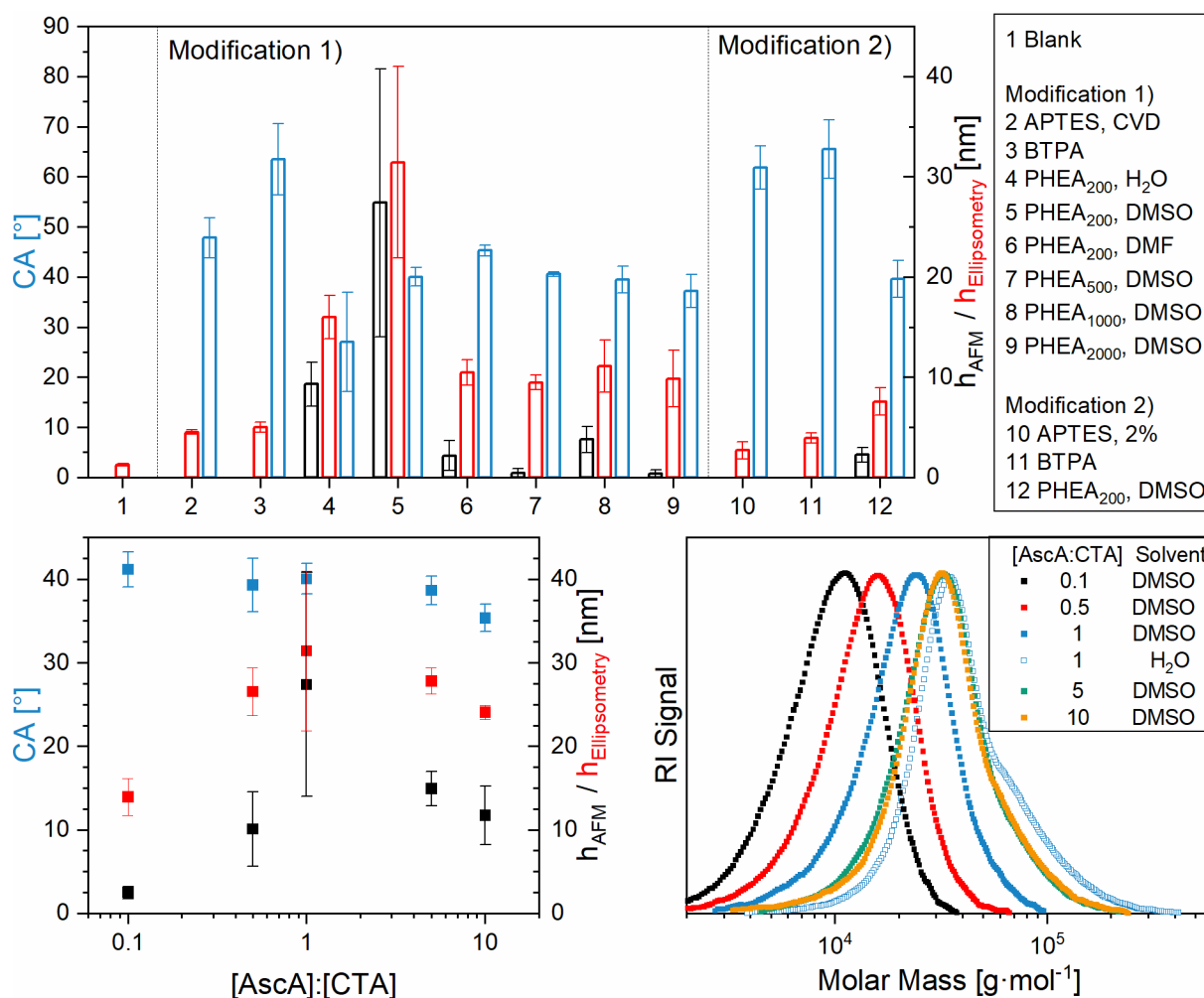
Figure 26:   *Surface characterization (top and bottom left) including film thickness (h) and CA, and molar mass distributions (bottom right) after grafting-from PET-RAFT homopolymerization of HEA (Table 7).*

AscA influences the radical generation and consumption of dissolved oxygen of the initiator system.[139] In previous studies, an optimum concentration was determined, as a minimum amount is required to conduct the polymerization, but surprisingly, decreasing monomer conversion appears above a certain value.[139,141] The studies explain the decreasing monomer conversion above a certain value due to the occurrence of initiator side reactions.

Increasing the concentration of AscA while maintaining the EoY concentration leads to increased conversions and higher molar masses as summarized in Table 7. The higher polymerization rates are attributed to the oxygen consumption and rate of initiation. In contrast to the literature, a decrease of conversion is not observed.[139] Still, a tiny shoulder at higher molar masses is apparent in the peak in the SEC analysis for 5 and 10 eq. of AscA (Figure 26, bottom right). This result is not necessarily connected to initiator related side reactions as also the high viscosity at higher conversions limits the macro-CTA mobility thus increase the probability of radical involving side reactions. Figure 26 (bottom, left) summarizes the surface analysis of the obtained samples for the varying AscA amounts. The results validate the

influence of this parameter. Polymers are successfully grafted in each case as indicated by relatively low CAs and significant films thicknesses. Increasing layer thickness is evident with increasing AscA content in the range of 0.1 to 1 eq., which is consistent with increasing conversions and molar masses (Table 7). No increase of film thickness is apparent for higher amounts of AscA from 1 to 10 eq., although further increasing conversions and molar masses are also verified for these samples. Rather, the opposite tendency is visible, the mean values of the layer thicknesses indicate a decrease in this area. However, the overlapping error margin of the standard deviation indicates the need of more data to finally distinguish, if the film thickness levels off or decreases above AscA values of 1 eq. According to the overall best result, the optimal AscA amount of 1 eq. is chosen as optimal condition for following experiments.

The increase of the targeted molar mass is set by a decrease of the CTA concentration while the monomer concentration is kept constant. For this, the amount of surface-bound CTA is still negligible, as CTA concentration is only decreased by the factor 10 (see Chapter 3.2.2.1 and Equation (16)). Results displayed in Table 7 indicate very low conversions at a HEA feed of ≥ 200 eq. Accordingly, low film thickness found are on respective substrates (Figure 26). The CA measurement confirms a polar modification of the surface after the reaction. It has to be noted that the concentration of the initiator system EoY/AscA is reduced in these experiments to maintain its relative ratio to the CTA. This leads to slower consumption of dissolved oxygen and slower formation of radicals, which explains the low conversions. An alternative strategy for increasing the target molar mass, in which only the concentration of a single component is changed, is to increase the monomer concentration. This strategy, however, has not been tested in this work. It is expected to further amplify the already strong viscosity increase due to polymerization, thus promoting radical side reactions. Consequently, the synthesis of higher molar masses requires the simultaneous adjustment of more than one parameter and is therefore not part of this first basic survey on good grafting-from conditions.

In summary, PET-RAFT using an EoY/AscA initiator system is suitable for the grafting of PHEA from CTA-modified Si wafers. It is shown that DMSO works as an alternative solvent instead of H_2O. The best grafting results are obtained with modification protocol 1 and a ratio [M]:[BTPA]:[AscA]:[EoY] of [200]:[1]:[0018].

3.2.2.2.2 The Grafting of PHEA$_x$SPA$_y$ from Si Wafers

In this chapter, the PET-RAFT technique for grafting SP-containing copolymers from Si wafers is described, followed by an analysis of the switchable properties of the surfaces. The reaction conditions used are based on the optimization of the previous Chapter 3.2.2.2.1, which shows the successful grafting of PHEA homopolymers from Si wafers. As described at the beginning of Section 3.2.2.2, green light is used to stimulate the photoisomerization of the MC isomer (Figure 19) and thus enable the polymerization of SP-containing monomers (Chapter 3.2.1). Furthermore, this wavelength is suitable to excite the EoY/AscA initiator system.

Table 8 summarizes the conducted copolymerization experiments. The SPA content of the polymer feed is varied in three steps. For each of these steps, three batches were tested and the triple-determination is represented by the given results as average values with standard deviation. The reproducibility of the synthesis is good as the standard deviation is approximately as high as the estimated error range of the respective method. The determination of the conversion by ^{1}H-NMR spectroscopy from samples before and after the polymerization is analyzed according to Equations (18) and (19) as discussed in Chapter 3.2.3. In principle, a polymer could be obtained for each polymerization with SPA contents up to 25 %. In this context, however, the conversions show a decrease with increasing SPA content. This observation, attributed to a retardation effect by the SP moiety, is previously observed and discussed (Chapter 3.2.1). The molar masses of PHEA$_{190}$SPA$_{10}$ and PHEA$_{180}$SPA$_{20}$ are similar, even though both polymerizations showed slightly different conversions. This is explained, as the dispersity of the latter is higher. In addition, this can be due to the method itself. SEC measures the elution time of a polymer sample and the result, which is related to the hydrodynamic radius, is typically expressed as molar mass relative to a standard polymer. However, the relationship between the hydrodynamic radius and the degree of polymerization is influenced by the monomer composition, and this monomer composition is not the same for the two SP polymers. The molar mass distribution of the copolymers is shown in Figure 27. Some of the curves show slightly pronounced shoulders at higher molar masses. Together with the results of the dispersities in Table 8, this shows moderate to poor reaction control. This observation is in line with literature reports (see Section 1.6.1.2) and previous results for the SP colymerization (compare with Chapter 3.2.2.1 and Chapter 3.2.1).

Table 8:   *Summary of results after CTA-shuttled grafting-from PET-RAFT polymerization of PHEA$_x$SPA$_y$. Each reaction is triplicated and the given results display average values with standard derivations. The conversion is analyzed by ^{1}H-NMR and the molar masses and dispersities by SEC.*

Monomer Feed		Polymer			
HEA	SPA	X	M$_n$	M$_w$	Đ
[eq.]	[eq.]	[%]	[kg·mol^{-1}]	[kg·mol^{-1}]	
190	10	86.2±0.4	31.8±0.2	47±2	1.49±0.07
180	20	78±3	30±2	51±6	1.7±0.1
150	50	44±5	18±2	29±4	1.55±0.08
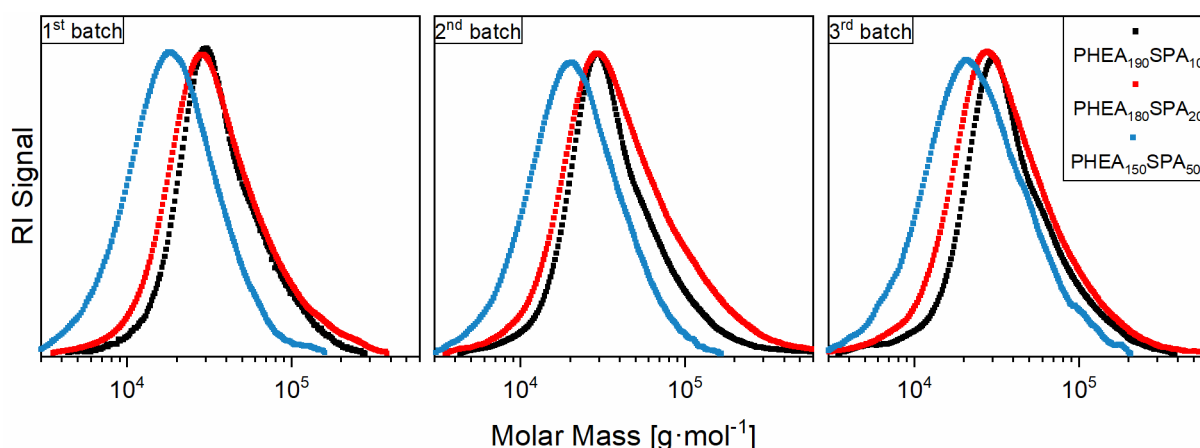
Figure 27:   *Molar mass distributions of three batches of PHEA$_{190}$SPA$_{10}$, PHEA$_{180}$SPA$_{20}$ and PHEA$_{150}$SPA$_{50}$.*

Figure 29 summarizes the surface analysis of the substrates used in the polymerization and includes AFM measurements, ellipsometry and a CA analysis. The comparability between the thickness measurement methods is previously discussed (Chapter 3.2.2.2.1). The ellipsometry analysis indeed reveals a few nm difference in the thickness of the organic layer comparing samples before and after the polymerization. This result is supported by the AFM measurements in which a polymer layer of around 2 nm is detected. The film thickness shows no significant dependence on the SPA content in the monomer feed despite the difference in monomer conversion. However, the film thicknesses are very small, so that low differences are not detectable due to the error range of the method.

SP-containing materials usually exhibit a color in the spectrum between blue and red, coming from the MC isomer.[55] However, the coloration of the wafers is not visible to the bare eye. Nor does radiation with UV-A, which stimulates the typical fluorescence of the chromophore, show the characteristic light emission (Figure 28). The figure also shows a positive control sample, which is partially coated with a few µm of PHEA$_{37.5}$SPA$_{12.5}$ polymer. This control sample shows fluorescence in an orange-red color. Moreover, the red color of the control sample became more intense after UV-A exposure, indicating the isomerization process to the MC isomer. The

weak optical activity of the polymer film, which is only a few nm thin, in contrast, is attributed to the detection limit.

Nevertheless, another method, the CA analysis, confirms the presence of SP units in the polymer on the surfaces. These measurements determine values between 60 and 80° (Figure 29). This is relatively non-polar compared to the PHEA homopolymer surfaces showing values even below 50° (Figure 26). The copolymer surfaces show increasing CA values as a function of SPA equivalents in the monomer feed. This result fits the expectation derived from the properties of the monomers. HEA is more polar than SPA, which is reflected, for example, in the good solubility of HEA and the rather poor solubility of SPA in water. Therefore, the CA results demonstrate the successful incorporation of SPA and further prove that the fraction of SPA in the monomer feed appropriately influences the composition of the grafted polymer chains.
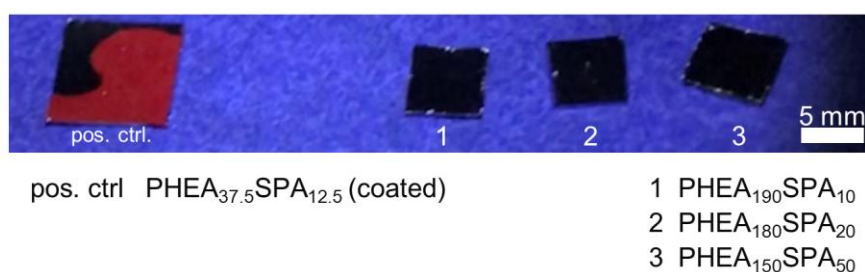
Figure 28: *Photography of Si wafers after grafting-from of PHEA$_x$SPA$_y$ and positive control sample upon UV-A radiation. The positive control is partially coated with a few µm thick layer of fluorescing PHEA$_{37.5}$SPA$_{12.5}$ (see Section 3.2.1). The background is black paper.*

AFM measurements in liquid mode after UV or VIS radiation of the copolymer allow the measurement of the thickness of the polymer film swollen in water, including the possibility of in-situ alteration of the thickness by light. Swelling differences are expected since the incorporated SP unit is known to change the polarity upon radiation. Preliminary experiments with SP containing copolymers showed partial solubility in water, which was evident from the red coloration of the solution. Accordingly, there is a certain compatibility between SP/HEA-copolymers and water, which is necessary for a swelling process. Liquid mode AFM reveals the thickness differences between wet PHEA$_{180}$SPA$_{20}$ and PHEA$_{150}$SPA$_{50}$ surfaces to be insignificant compared to the dry measurement. Accordingly, no swelling could be observed. The measured thickness value of PHEA$_{190}$SPA$_{10}$ even seems to be lower in the liquid measurement, which is the opposite of what is expectable after swelling. This error is attributed to the random and unrepresentative choice of the analyzed spot on the sample. Whereas the dry AFM results are averaged over a few different spots on the sample, the liquid AFM measurement was only performed on one spot after the respective radiation. Consequently, the assigned error bars result from the measurement and data processing such as baseline subtraction. Nevertheless, the comparability of the values after treatment with UV or VIS

radiation should be given, since differences that could result from different measuring points on the sample are excluded. It was expected that an increased swellability could be observed after exposure to UV light, since the isomerization to the MC form increases the polarity of the polymer. Unfortunately, however, no significant change in film thickness is observed when exposed to UV or VIS radiation. It is possible, that the synthesized films are too thin to reveal detectable changes of the relative swelling ratios. The relative ratio between average value and error bars of the measurement indicate indeed, that the experimental setup operated at its lower resolution limit. The analysis of thicker layers, another swelling agent or the use of an experimental setup with improved precision is suggested for future investigations on the light-responsive swelling of the films. Unfortunately, other swelling agents could not be tested within the scope of the work so far, since the available experimental setup is only designed for measurements in water.
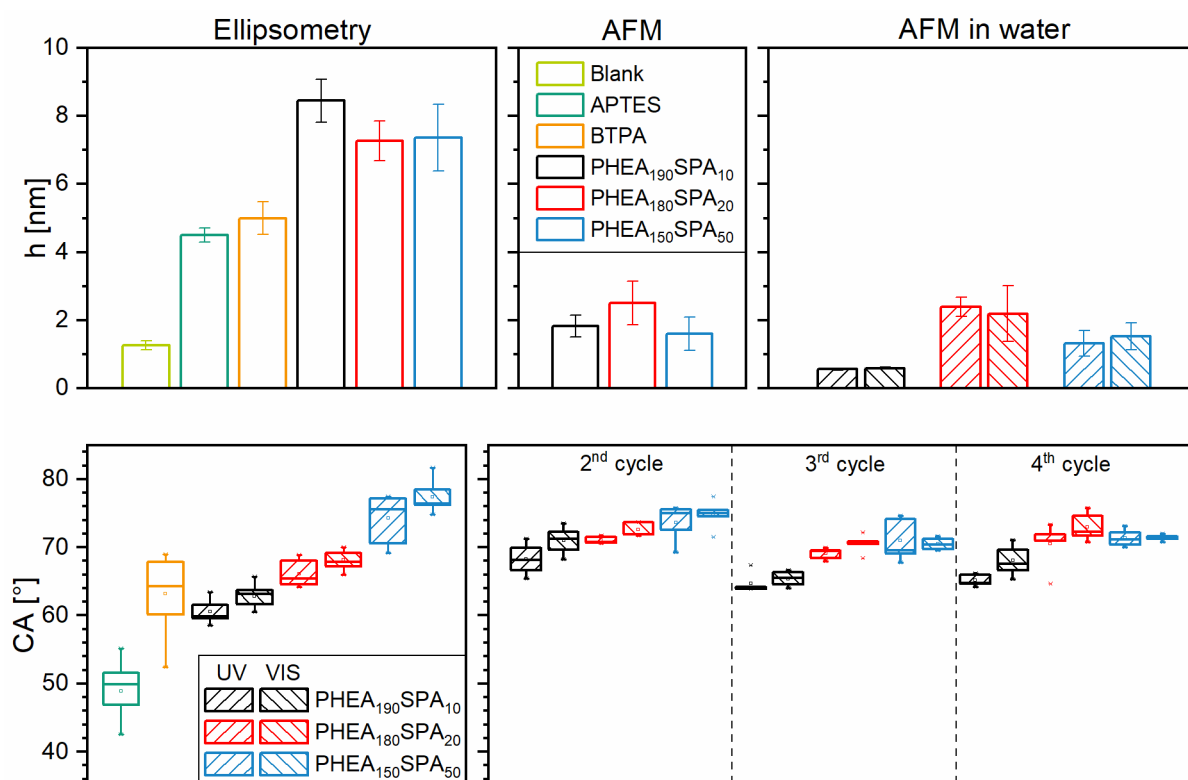
Figure 29:   Surface characterization including film thickness (h) and CA measurements of $PHEA_xSPA_y$ copolymer surfaces obtained by PET-RAFT grafting-from polymerization. Their light-responsiveness is analyzed using liquid mode AFM, and CA measurements after UV or VIS radiation.

The analysis of switchable surface polarity by CA measurements after UV and VIS radiation gives results that are more conclusive. Figure 29 (bottom, left) displays the values after a first radiation cycle. The measured range of the CAs after either UV or VIS radiation overlaps in each case. Despite this, the statistical distribution represented by the box plots indicates a less polar surface after VIS radiation. VIS radiation shifts the equilibrium between the zwitterionic MC isomer and the non-polar SP isomer more towards the latter, while UV works in the opposite direction (Scheme 5B). It explains the observed polarity change of the surfaces, which are additionally confirmed in measurements of subsequent radiation cycles (Figure 29, bottom right). Therein, a statistical difference between the CA after UV and VIS radiation of $PHEA_{190}SPA_{10}$ and $PHEA_{180}SPA_{20}$ is apparent in all cycles. A switchable polarity for $PHEA_{150}SPA_{50}$ could not be confirmed in the successive programming cycles. Furthermore, a shift of the values between the first measurement and the other cycles (2-4) becomes apparent. One explanation may be that the CA measurements of the repeating cycles were taken with a time difference of several months from the CA measurements first radiation cycle. It is possible that the surface properties of the soft polymer change over time, for example, as certain domains orient toward the surface. Such surface changes are known, for example, from the thermal annealing of random copolymer films.[142] Accordingly, more investigations on the reproducibility as well as the switchable surface polarity in dependence with time and radiation periods are necessary to explain these shifts.

In summary, SP/HEA copolymers are successfully grafted by PET-RAFT from CTA-modified wafers following the previously optimized polymerization conditions for the PHEA grafting and considering the light-dependent polymerization characteristics of the SPA monomer. The few nm thick polymer layers exhibit light-switchable switchable polarity. Switchable swelling could not be confirmed due to the low film thicknesses, which challenge the detection limit of the analytical method used.

3.2.3   Summary of Chapter 3.2

The second part of this work demonstrates PET-RAFT for the grafting of SP copolymers from CTA-modified Si wafers and gives a first assessment on the light-responsiveness of the obtained surfaces. The surfaces feature switchable surface polarity as indicated by water CA measurements. Liquid mode AFM analysis of the polymer layer height in water, in contrast, could not confirm a light-dependent behavior, which is most likely related to the accuracy of the experimental setup. Nevertheless, the findings suggest the synthesized SP surfaces as promising candidate for further investigations on switchable properties, particularly, a tribological assessment of the light-dependent friction properties.

The applied synthesis optimization strategy included pre-experiments on the thermally initiated solution copolymerization of SPA and HEA, which highlight the light-dependent character of the polymerization and identifies the photochromism of SP as origin of this observation. The inhibition of the polymerization in the dark suggests that the MC isomer interacts with the radicals involved in the mechanism of the polymerization, yet mechanistic details require further investigation. In this regard, however, DFT calculations confirm that the MC isomer should have higher reactivity with radicals than SP.

Grafting-from experiments assessed thermally initiated and PET-initiated polymerization conditions for the fabrication of respective polymer surface layers. The first testing of thermally initiated homopolymerization of different polar monomers leads to detectable polymer layers only in case of TRISAM. In case of HEA, NAM, DMAM and OEGA no polymer layers are detectable, although the respective polymerizations work in solution. The same result is obtained for the copolymerization of SPA and TRISAM, which leads to unsuccessful grafting. Differently prepared CTA-modified Si wafers affect the thickness of the grafted PTRISAM. The methods differ in that the introduction of the amino group, prior to bonding of the CTA via amidation, was carried out in solution or by chemical vapor deposition (CVD). The preparation with CVD ultimately resulted in thicker PTRISAM layers. Overall, the results point out that thermally initiated surface polymerization is a demanding method. As the process is initiated in solution, the growing polymer chains must diffuse to the surface to start the grafting-from process. The fact that no polymer layers were found for some monomers tested suggests that the surface compatibility of the growing polymer for the thermally initiated grafting-from process varies depending on the monomer used and is critical for grafting success.

Better grafting results in form of thin layers of detectable polymer were obtained with PET-RAFT. It is assumed that differences in the mechanism compared to the thermally initiated RAFT method explain this finding. In PET RAFT, radical species do not necessarily have to diffuse to the surface, but the surface-bound CTA can also be directly excited by the electron/energy transfer of the photocatalyst, triggering surface-initiated chain growth. The

work shows an optimization of the PET-RAFT homopolymerization conditions for HEA in the grafting-from approach. DMSO is found as an alternative solvent to water and the concentrations of the catalyst system are adjusted. Furthermore, also this method confirms, that CTA-modified surfaces prepared via the CVD route yield better grafting results. Finally, the optimized synthesis protocol is used to immobilize a grafting-from copolymer of HEA and SPA on Si wafers.

The first optimization of the HEA/SPA grafting-from copolymer synthesis is a promising starting point for further research on light-switchable polymer brushes for the alteration of macroscopic surface properties. In this context, the RAFT synthesis applied here offers many opportunities to change certain structural parameters of the polymer layer such as monomer composition, layer thickness and polymer architecture. Accordingly, it could be interesting to investigate how the above-mentioned structural changes affect light-switchable surface properties.

4. Conclusion

The presented thesis deals with the synthesis and the property assessment of two novel light-switchable materials, which are designed to enable the alteration of frictional behavior.

The first type of materials presented are light-switchable silicone oils. These solvent-free fluids consist of PDMS chains functionalized with 9-anthracene ester termini. They were studied in rheological experiments, which showed that certain properties, such as viscosity, can be modified by a mechanism of reversible polymer chain extension. This chain extension is the result of a dimerization of the terminal anthracene units, which is triggered by UV-A light, thereby leading to an increases of the viscosity of the silicone fluids. The increase is partially reversed by UV-C light, while the initial mechanical properties are fully restored upon thermal treatment. Accordingly, the programming of high viscosities is limited by the thermal stability of the anthracene dimers (about 130 °C), even though simultaneous UV-A radiation can compensate the thermal cleavage to some extent. Furthermore, it could be shown that the functionalized silicone fluids are useful additives for a non-functionalized silicone oil. Depending on the chain length and the associated miscibility, the functionalized silicone fluids allow the rheological properties of the corresponding blends to be modified by light.

In principle, the concept of light-programmable viscosity is suitable for improving lubricant materials, since the viscosity can be adapted to a specific operating condition of a friction pair, thus optimizing the Stribeck curve. However, some factors must be considered for the applicability of the presented system. Photochemical programming is more likely to take place inhomogeneously due to the attenuation of the light beam upon its pathway through the material to be programmed. Accordingly, the functionalized silicone oils are considered to be more suitable as light-programmable thin films. Fortunately, this requirement is typically met in lubrication applications. Furthermore, the shear occurring in lubrication applications counteracts the inhomogeneity issue due to a mixing effect. Another important issue of the presented system is the occurrence of photooxidative degradation reactions in the presence of oxygen. Accordingly, only those potential applications come into consideration that get by with a limited number of programming cycles. Otherwise an oxygen-free environment must be ensured.

Polymer brushes containing spiropyran (SP) are presented as a second material concept that is envisioned to enable light-switchable friction properties. The concept is based on the lubrication between polymer brush surfaces, which is due to the osmotic pressure repulsion. The solvation of the polymers and thus the lubricating properties can be changed by the light-switchable polarity of SP. The synthesis of the spiropyran copolymer surfaces was optimized in several steps. First tests on the investigated polymerization system showed that SP-containing monomers polymerize only under the influence of visible light which most likely

stems from a photoisomerization that prevents side reactions between radicals and the merocyanine isomer (MC). Moreover, the optimization process revealed that surface-initiated RAFT polymerization was easier to achieve synthetically with photoelectron/energy transfer (PET) initiation than by classical thermal initiation. This is likely due to the mechanism of PET-RAFT, which enables a direct activation of surface-bound CTA. In addition, PET-RAFT has the advantage of a certain oxygen tolerance. Relying on these results, direct copolymerization of spiropyran acrylates (SPA) with 2-hydroxyethyl acrylate (HEA) by PET-RAFT was achieved, enabling the grafting of polymer brushes with high spiropyran content (5-25%) from Si wafers. The synthesized SP copolymer brushes exhibit light-switchable polarity, rendering them a suitable candidate for further investigations on light-switchable properties. Within the time frame of the thesis, it was not possible to investigate light-switchable friction properties between swollen SP graft copolymer surfaces. Accordingly, further tribological studies need to be performed. In this context, certain parameters of the polymer brushes, such as thickness, SP content, polymer architecture (e.g. SP-containing block copolymers), can be adjusted by changing the polymerization conditions in order to subsequently evaluate the extent to which this improves the light-switchable friction properties.

5. Methods and Materials

5.1 Analytical Techniques

5.1.1 Atomic Force Microscopy (AFM)

Surface topography was acquired with a Dimensions Icon (Bruker) device in the ScanAsyst mode. The device was equipped with a Scanasyst-Air probe (triangular, $r_{tip} = 2$ µm, $f_0 = 70$ kHz, $k = 0.4$ N·m^{-1}) and for measurements in water with a ScanAsyst-Fluid probe (triangular, $r_{tip} = 20$ µm, $f_0 = 150$ kHz, $k = 0.7$ N·m^{-1}). The thickness of the graft-polymer on a modified Si wafer was estimated from the height difference to an area in which the organic layer was selectively removed by scratching with a cannula. All images were collected approximately in the dimensions 5×50 µm at a scanning rate of 0.5 Hz. The software NanoScope Analysis v1.9 (Bruker) executed 2nd and afterwards 1st order correction in the xy plane separately for the scratched and unscratched area. The software's built-in step analysis tool was used to estimate the average height difference between the scratched and unscratched area (Figure 30). All samples measured with air environment were analyzed at three to five different spots. The samples measured in water were radiated 20 min prior to the measurement and additionally during the measurement with either VIS (V-TAC VT-2099, 9W, warm white) or UV-A (Aimaylly 365 nm LED pocket lamp 5W). The topography was recorded three times at the same spot. All results are given as average with standard derivation.
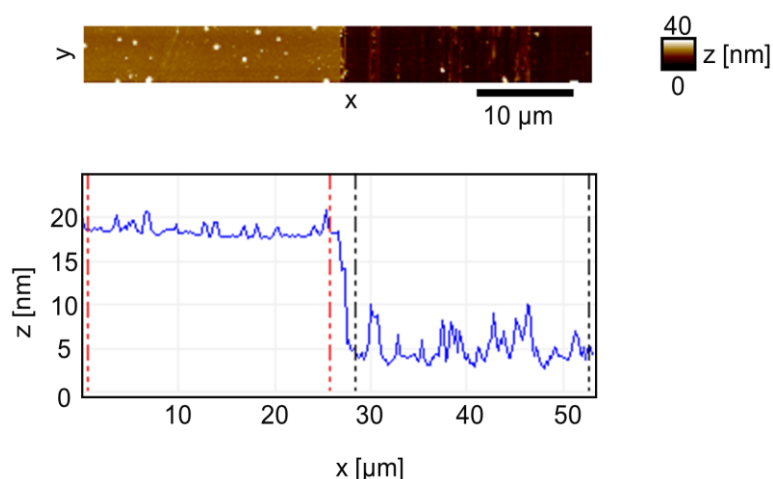
Figure 30:   AFM image (top) at the transition between the area of a non-scratched and scratched polymer layer on a Si wafer (sample [HEA]:[Asc]=200:5: see also Table 7 and Figure 26). The sample was analyzed using the step function tool (bottom) of the Nanoscope Analysis software.

5.1.2　Bright Field and Fluorescence Microscopy (BF, FM)

Microscopy images were acquired using a DMi8 (Leica) device with attached HC PL FLUOTAR L 63x/0.70 dry (Leica) objective and a C11440-22CU (Hamatsu) USB camera. The processing was executed by the LAS X v2 (Leica) software. The same illumination and recording conditions were set in the software for all BF (exposure 20.68 ms, intensity 111, aperature 9) and FM (DAPI-channel, exposure 30.00 ms, FIM 30%, IL-Fid. 6) images, respectively. PDMS and –mixtures were stirred with a spatulus before the thin film was prepared by placing a drop between glass slide and cover slip.

5.1.3　Ellipsometry

Modified Si wafers were cleaned by rinsing EtOH over the surface prior to the measurement with a Multiscope (Optrel GbR) system. The angle of incidence for the null ellipsometer configuration was 70°. Calculations determining the layer thickness were executed using the software Elli v5.2 (Optrel GbR) under the assumption a four-layer model consisting of air ($n_1 = 1.0000$,$k_1 = 0$), organic material ($n_2 = 1.5000$,$k_2 = 0$), silicon oxide ($d_3 = 1.0$ nm, $n_3 = 1.4580$, $k_3 = 0$) and silicon ($n_4 = 3.8858$, $k_4 = -0.0200$). Each sample was measured on at least five different spots and given results are average values with standard derivation.

5.1.4　^{1}H-Nuclear Magnetic Resonance Spectroscopy (NMR)

All spectra were recorded using a Avance Neo (Bruker) 400 MHz device. Spectra processing including phase correction, baseline correction, calibration and analysis of the signals was executed by the software TopSpin v4.07 (Bruker).

PDMS based samples were dissolved in $CDCl_3$. Radiated PDMS samples (two drops, 4 mg each on a glass surface) were treated with either $\lambda_1 = 365$ nm (UV-A) or $\lambda_2 = 254$ nm (UV-C) using a UV handlamp (Analytik Jena UVP UVGL-25) at a distance of 1.3 cm.

All samples containing acrylates, acrylamides, spiropyrans and derived (co-)polymers were dissolved in DMSO-d_6. The samples for the analysis of kinetics and conversions of polymerizations were prepared by diluting 0.1 mL of the reaction solution.

The analysis of the monomer concentration from the spectra was conducted using the spiropyran moiety as internal aromatic standard (polymerization with SPP or SPA). The respective intensity (I_{St}, see Equation (18) in Chapter 3.2.1) is based on the signals g, h, i, j

and k is shown in Figure 21 in case of HEA copolymerizations. Anisol was used as internal aromatic standard for polymerizations without SPA or SPP.

The intensity of signals of aromatic protons assigning to spiropyran or anisol were used as reference for the determination of the conversion.

5.1.5   Rheology

Two different rheometer settings were applied in this work. The first setup applied for the measurements of Section 3.1.1 was as follows: A Discovery HR-3 rheometer (TA Instruments) executed the measurements in plate-plate geometry (diameter 30 mm) at 20 °C. The device was equipped with an upper UV-transparent quartz glass plate that enabled the illumination of the rheometer gap (620-670 µm) from top (Scheme 12). Two dual mode UV-A/C lamps (Analytik Jena UVP UVGL-25) with peak wavelengths at 254 nm and 365 nm were positioned above the upper plate. The homogeneous light intensity distribution of the setup was verified with a UV light film (Fujifilm UVSCALE L). The measurements were recorded in the linear viscoelastic region as verified by amplitude sweeps. Six oscillations (0.3 %, ω = 3 rad·s^{-1}) were averaged to calculate dynamic moduli G' and G'' at a shear rate of $\dot{\gamma}$ = 0.033 s^{-1}. Rotation and oscillation sequences were performed in an alternating order. A rotation experiment (170 s per sequence) was carried out after each oscillation experiment (760 s per sequence) for the homogenization of the silicone oil. For the viscosity measurements, PDMS samples were strained between 12 and 30 s at each shear rate step and the viscosity was averaged over the last three seconds when a deviation of ≤1 % occurred. Heating and cooling (both 10 K·min^{-1}) of temperature dependent measurements were respectively controlled by the built-in Peltier and counter-cooling element in the lower plate of the rheometer. The second setup applied for the measurements in Chapter 3.1.2 was adjusted to improve the programming time of the responsive material and therefore improve the experimental throughput. The rotation sequences were removed from the rheometer program. The light sources were replaced by two NVSU233B (Nichia) UV-A (365 nm) LEDs. Tobias Rosenstingl, Florian Schlüter, Lukas Wirth, and Teodora Rangova carried out the measurements at the Fraunhofer IWM in Karlsruhe.

5.1.6   Size Exclusion Chromatography (SEC)

All samples were passed through a 0.45 µm PTFE filter before injection. PDMS based polymers were measured with simultaneous UV (TSP UV 2000 at λ = 254 nm) and RI (Wyatt Optilab DSP RI) detection in THF as eluent at 25 °C and a flow rate of 0.5 mL min^{-1}. Separation was performed by a 3 µm 8×300 mm^2 linear M column (PSS SDV). Polyacrylate and -acrylamide based polymers were detected by RI (Shimadzu RID-6A) in NMP with 0.5 %

LiBr as eluent at 25 °C at a flow rate of 0.5 mL·min^{-1}. The stationary phase was a 7 μm 8×300 mm linear column (PSS GRAM). Both system were calibrated against polystyrene standards (PSS). The analysis of the chromatograms was executed by Sascha Prentzel using the WinGPC UniChrom, Build 4815 (PSS) software.

5.1.7   Ultraviolet-Visible Spectroscopy (UV/VIS)

Spectra were recorded by a Specord 300 (Jena Analytics) device at a resolution of 2 nm^{-1}. Background correction was performed against air. SPP and SPA were measured in DMSO (0.1 M) of using a quartz cuvettes (Hellma Analytics, d = 0.2 mm). BTPA was measured in DMSO (0.05 M) using other quartz cuvettes (Hellma Analytics, d_1 = 0.2 mm, d_2 = 10 mm).

5.1.8   Water Contact Angle (CA)

Shortly before measurements were performed, all surfaces were rinsed with EtOH and dried with at air. Static water droplets (5 μL, MilliQ) were dosed (500 μL syringe, Hamilton) and recorded after a few seconds using a OCA 15 device (DataPhysics Instruments). After the baseline was manually applied, contact angles were determined by the device's software SCA (DataPhysics Instruments). Three to five measurements per sample were performed and all results are given as average with standard derivation. Radiated samples were treated 20 min with either UV-A (Aimaylly 365 nm LED pocket lamp 5W) or VIS (V-TAC VT-2099, 9W, warm white) at a distance of ~ 2 cm and equilibrated for > 1 min at RT before the measurement in a darkened room.

5.1.9   X-Ray Photoelectron Spectroscopy (XPS)

XPS measurements were performed on an AXIS Supra+ instrument (Kratos Analytical, U.K.). For this purpose, monochromatic Al Kα-radiation (300 W) was used for excitation. The instrument was operated in hybrid mode with electrostatic and magnetic lenses. For neutralization of the sample charges, thermal electrons from a filament were used. During the measurement, the instrument was operated with a takeoff angle of 90° with an analysis depth of ~10 nm. Data analysis was performed using CASA-XPS Software.

The samples were prepared as follows. SPP (25 mg, 0.6 mmol) an AIBN (1 mg, 0.6 mmol) were dissolved in DMSO (0.6 mL) and heated for 48 h at 65 °C. A control experiment was performed similar but without AIBN. The samples were freeze-dried before XPS analysis.

5.2 DFT-Calculations

The radical association energies ΔE have been determined by Equation (27), where E_{bond}, $E_{SP/MC}$, and $E_{rad.}$ are the DFT ground state energies of the bonded system (after radical attack), the isolated SP/MC isomer and the isolated radical, respectively.

$$\Delta E = E_{bond} - E_{SP/MC} - E_{rad} \tag{27}$$

All DFT calculations were performed using the Vienna ab initio simulations packag (VASP).[143] VASP uses a plane wav basis set in order to describe the valence electrons. For the expansion of the corresponding Kohn-Sham wavefunctions a plane wave basis set with a cut-off energy of 600 eV was employed. Core electrons were taken into account by using the projector-augmented wave method (PAW).[144] As DFT approximation the standard semilocal PBE functional was employed and augmented by Grimme's D3 correction with the Becke-Johnson damping in order to improve the description of long-range dispersion effects.[145] All systems were relaxed until the maximum atomic force was below 0.01 eV·Å^{-1}. To avoid spurious interactions between periodic images large simulations were carried out with unit cells of dimension 3.75×2.55×2.55 nm^3.

5.3 Materials

ABCVA (≥ 98 %, Sigma Aldrich), anisol (99% Acros), APTES (> 98 %, TCI), DABCO (99 %, Sigma Aldrich), dioxane (≥ 99.5 %, Fischer Scientific), DMF (99 %, Sigma Aldrich), DMSO (≥ 99.8 %, VWR), DMSO-d_6 (99.8 % D, Euroisotop), EDC·HCl (>99 %, Carl Roth), EtOAc (≥ 99.8%, VWR), EoY (> 95 %, TCI) EtOH (96 %, Chemsolute), HCl, (37 /, Carl Roth), HDI (> 99 %.Sigma Aldrich), H_2SO_4 (95 % Chem Solute), NaCl (≥ 99, ChemSolute), NaOH (≥ 99 %, Carl Roth), NH_4OH solution (30 wt%, Carl Roth), n-hexane (≥ 95 %, VWR), PDMS (XIAMETER^{TM} PMX-200 100 cSt, DOW) propionyl chloride (99.5 %, Acros), Si Wafer ([1.0.0], p-Type, thickness 625 μm) TRISAM (93 %, Sigma Aldrich), toluene (99.5 %, Chemsolute) were used as received.

Acryloyl chloride (> 96 %, Merck) was distilled before use. AIBN (98 %, Sigma-Aldrich) was recrystallized from $CHCl_3$ before use. $CDCl_3$ (> 99 %, 99.8 %D, Sigma Aldrich), $CHCl_3$ (amylene stabilized, Sigma Aldrich) and NEt_3 (99.5 %, Sigma Aldrich) were dried over mole sieve (4 Å) before use. α,ω-bis(hydroxyethoxypropyl)-PDMS (PDMS0-(OH)$_2$, Sigma Aldrich, M = 5.600; PDMS-(OH)$_2$, LivchemLogistics, 300-350 cSt, M = 10.000), hydroxyethoxypropyl PDMS (PDMS-OH, Fluorochem, 250 cSt, M = 10.000) and (Tetramethylpiperidinyloxy)-propylmethylsiloxane-dimethylsiloxane copolymer (PDMS-HALS, Fluorochem, cSt 250, 7-9 mol% HALS) were dried under high vacuum before use.

The stabilizer contained in DMAM (99 %, Sigma Aldrich), HEA (96 %, Sigma Aldrich) and NAM (98 %, TCI), and OEGA (M_n = 480 g·mol^{-1},Sigma Aldrich) was removed over Al_2O_3 (neutral, activated, Brockmann I, Sigma Aldrich). All syntheses were carried out under inert atmosphere.

5.4 Syntheses

5.4.1 Anthracene-Functionalized Silicone Oils and -mixtures

The molar masses given by the manufacturer (for PDMS-(OH)$_2$ and PDMS-OH M = 10.000) were assumed as number average value (M_n = 10 kg·mol^{-1}) for the following calculations.

α,ω-Hydroxyalkyl-terminated PDMS precursors **(PDMS2-(OH)$_2$, PDMS3-(OH)$_2$)**
The hydroxyalkyl-terminated precursors PDMS2-(OH)$_2$ and PDMS3-(OH)$_2$ were synthesized by urethane linked chain extension of PDMS-OH$_2$ with HDI. The ratio of isocyanate to alcohol groups was 0.44 and 0.67, respectively, and the base DABCO was used equimolar with respect to isocyanate groups. The procedure is exemplified for PDMS2-(OH)$_2$ as follows: PDMS-OH$_2$ (35 g, 7 mmol OH groups) and HDI (0.259 g, 1.54 mmol) were dissolved in toluene (35 mL). After addition of DABCO (0.354 g, 3.08 mmol) the mixture was stirred at 70 °C for 5 h and kept at RT overnight. The solvent was evaporated in vacuo and the crude oil was purified by centrifugation. The supernatant was separated and a clear liquid (30.2 g, 86 %) with an increased viscosity was received.

9-Anthracenecarbonyl chloride **(A-COOH)**
The esterification agent was synthesized as described in the literature.[50]

9-Anthracenecarboxylic acid ester-terminated PDMS **(PDMS-A$_1$, PDM0-A$_2$, PDMS-A$_2$, PDMS2-A$_2$, PDMS3-A$_2$)**
All anthracene-functionalized PDMS'S were synthesized from respective hydroxyalkyl-terminated precursors (PDMS-OH, PDMS0-(OH)$_2$, PDMS-(OH)$_2$, PDMS2-(OH)$_2$, PDMS3-(OH)$_2$) with a 1.5 eq. excess of esterification agent (A-COOH) to hydroxyl group. The procedure is exemplified for PDMS-A$_2$ as follows: Under stirring, 2.16 g (9 mmol) of A-COOH, dissolved in 12 mL CHCl$_3$ were added to a solution of PDMS-(OH)$_2$ (30 g, 6 mmol OH-groups) in 13 mL CHCl$_3$. The reaction was conducted for 20 h at 60 °C. Subsequently, the solvent was removed in vacuo and the residual oil was centrifuged. The supernatant was dissolved in CHCl$_3$ and subsequently washed with 0.1 M NaOH, 0.1 M HCl, H$_2$O, sat. NaCl solution and dried over Na$_2$SO$_4$. After removing the solvent in vacuo, centrifugation was performed in order to remove unreacted anthracene species. Finally, the reaction product was received as yellow viscous liquid (25 g, 83 %).

Mixtures

PDMS were mixed by the mass ratio and subsequently stirred and placed for 10 min in an ultrasonic bath.

5.4.2 CTA and -modified Si Wafer

2-{[(butylsulfanyl)carbothioyl]sulfanyl}-propanoic acid **(BTPA)**
The CTA was synthesized according to the literature.[146]

CTA-modified Si-Wafer

Si Wafer were cut (1×1 or 0.6×0.6 cm) and subsequently immersed in conc. H_2SO_4, Milli-Q water and EtOH. Afterwards, the cleaned surface was activated with O_2 plasma (PlasmaFlecto 10, Plasma Technology GmbH, 300 W, 300 s) before one of the following amine-modification protocol was performed. The first method (modification 1) was CVD with APTES (250 µL) and NH_4OH (250 µL) conducted in a closed PFA vessel (60 mL) at 70 °C for 2 h. The second method (modification 2) was performed by placing the wafers into a solution of APTES in EtOH (2 wt%, 30 mL) at RT overnight. All wafers were rinsed with EtOH and dried with compressed air. Afterwards they were immersed into a solution of BTPA (5 mg, 0.02 mmol), EDC·HCl (5 mg, 0.03 mmol), NEt_3(5 µL, 0.04 mmol) in DMF (1 mL) overnight. Finally, the wafers were cleaned again by rinsing with EtOH.

5.4.3 Spiropyrans

2-(3',3'-dimethyl-6-nitrospiro[chromene-2,2'-indolin]-1'-yl)ethanol **(SPOH)**
Spiropyran alcohol was synthesized as described in the literature[147] and dried in HV before use.

2-(3',3'-dimethyl-6-nitrospiro[chromene-2,2'-indolin]-1'-yl)ethyl-acrylate **(SPA)**
SP-OH (3.33 g, 9.46 mmol, 1 eq.) and NEt_3 (3.95 mL, 2.87 g, 28.4 mmol, 3 eq.) were dissolved in $CHCl_3$ (26 mL) and cooled to 0 °C. After acryloyl chloride (1.15 mL, 1.28 g, 14.2 mmol, 2 eq.) was added dropwise, the reaction solution was stirred for 1 h at 0 °C and overnight at RT. The reaction solution was subsequently washed with H_2O, 1M NaOH, 1M HCl, brine and dried over Na_2SO_4. Finally, the solvent was removed under reduced pressure and the crude red solid (3.03 g, 78 %) was purified using column chromatography with n-hexane/EtOAc (5:1) as eluent. An orange-yellow solid (2.04 g, 53 %) was received as product.

2-(3',3'-dimethyl-6-nitrospiro[chromene-2,2'-indolin]-1'-yl)ethyl-propionat **(SPP)**

The synthesis and purification of SPP was performed similarly as described for SPA using propanyl chloride as esterification agent. An orange-yellow powder (34 %) was received as product.

5.4.4 Polyacrylates and -acrylamides

5.4.4.1 Solution Polymerization

*Poly[2-hydroxyethyl acrylate-co-spiropyran acrylate] (***PHEA$_x$SPA$_y$***)*

The molar ratio between monomers, chain transfer agent and initiator was [M]:[CTA]:[I]=100:2:0.1 eq. throughout all experiments. The composition of the monomer feed M=HEA+SPA was varied between 95+5, 90+10 and 75+25 eq., respectively. Following, a typical polymerization procedure is described for PHEA$_{45}$SPA$_5$: A stock solution of the initiator was prepared by dissolving AIBN (4.7 mg, 0.029 mmol) in DMSO (1 mL). HEA (300 mg, 2.58 mmol, 90 eq.), SPA (117 mg, 0.287 mmol, 10 eq.) and BTPA (13.7 mg, 57.3 µmol, 2 eq.) were dissolved in DMSO (2.5 mL) and an aliquot of the initiator stock solution (0.1 mL, 2.9 µmol, 0.1 eq.) was added. After the solution was degassed by three freeze-pump-thaw cycles, the 25 mL Schlenk tube with the reaction solution was placed in a clear silicon oil bath and the polymerization was performed for 48 h at 65 °C. Meanwhile, the vessel was radiated from the side using a VIS LED bulb (V-TAC VT-2099, 9W, warm white). Samples of the reaction solution (0.1-0.2 mL) were collected after 1, 3, 6, 9, 24 and 48 h using a nitrogen-purged syringe. The polymer was purified by dialysis (Spectrumlabs SpectraPor6 molar mass cut-MWCO = 1 kDa) against DMSO, EtOH and Acetone (3×300 mL) and finally, a red polymer was received.

Control experiments in the dark were performed by wrapping the Schlenk tube in aluminium foil before placing it into the oil bath.

The radical-free polymerization experiments were performed in the same way, except that no BTPA was included.

*Poly(2-hydroxyethyl acrylate) (***PHEA***)*

The same polymerization procedure and molar ratios of [HEA]:[BTPA]:[AIBN]=100:2:0.1 were used for the homopolymerization of PHEA. For the homopolymerization of HEA without presence of SPP, anisol (14 µL, 14 g, 0.12 mmol, 5 eq) was added as internal standard. The homopolymerization of HEA in the presence of a non-monomeric spiropyran was performed using 11 mol% SPP with respect to HEA.

5.4.4.2 Grafting-From Experiments

*CTA-Shuttled RAFT Polymerization **(PTRISAM, PHEA, PNAM, PDMAM, POEGA, PTRISAM$_x$SPA$_y$)***

The polymerization of HEA with a ratio of [HEA]:[BTPA]:[AIBN]=100:2:0.1 in DMSO was performed as described in Chapter 5.4.4.1 with an additional CTA-modified Si Wafer (1×1 cm), which was immersed into the solution before the degassing step. Furthermore, no internal standards were added.

The polymerizations of the monomers TRISAM, HEA, NAM, DMAM and OEGA with ratios [M]:[CTA]:[I] of 200:1:1/15 were performed as follows. Stock solutions of ABCVA (0.19 mg·mL^{-1}, 0.66 mM, 10 mL), PBTA (2.4 mg·mL^{-1}, 10 mM, 4 mL) and each monomer (2 M, 2 mL) were prepared in a mixed solvent of 1,4-dioxane and water (1:1 v/v). The monomer solutions were filtered through columns consisting of a syringes with Al$_2$O$_3$ as stationary phase to remove the contained inhibitors. Aliquots of the stock solutions with monomer (1 mL), PBTA (0.5 mL) and ABCVA (0.5 mL) were mixed and a CTA-modified Si Wafer (1×1 cm) was added. Finally, the solution was purged with N$_2$ for 30 min and placed in an oil bath at 70 °C for 20 h. The polymerization of TRISAM and HEA with a ratio [M]:[CTA]:[I] of 600:1:1/15 were performed with only 1/3 of ABCVA and PBTA in the reaction solution, while the monomer concentration was kept constant.

The polymerization of HEA with a ratio [M]:[CTA]:[I] of 50:1:1/20 in was performed with a monomer concentration of 1 M and AIBN as initiator in DMSO for 6 h at 65 °C.

TRISAM and SPA were copolymerized with ratio [TRISAM]:[SPA]:[CTA]:[I] of 180:20:1:1/15. SPA was added to the monomer solution after the filtration over Al$_2$O$_3$. The solvent ratio was slightly adjusted to 1,4-dioxane/water (1:0.8 v/v) and the solution was illuminated with a white LED (V-TAC VT-2099, 9W, warm white) while the polymerization was conducted at 70 °C for 48 h.

*CTA-Shuttled PET-RAFT Polymerization **(PHEA, PHEA$_x$SPA$_y$)***

HEA was filtered through a column consisting of a syringe with Al$_2$O$_3$ as stationary phase to remove the contained inhibitor. Stock solutions of EoY (20 mg·mL^{-1}, 31 mM, 1 mL) and AscA (100 mg·mL^{-1}, 0.568 M, 2 mL) were prepared. Reaction solutions with different ratios of [HEA]:[SPA]:[BTPA]:[EoY]:[AscA] were prepared by mixing the monomers with BTPA, aliquots of the stock solutions and different solvent accordingly (Table 9, Table 10). The CTA-modified Si wafer (0.6×0.6 cm^2) were placed at the bottom of a squared cuvette cover slips (inside 0.7×0.7cm^2), which was subsequently filled with 180 µL reaction solution. The uniform radiation with green light of the vessels covered with Parafilm lasted 20 h at RT. For this, the

samples were put under a custom-made aluminum bucket (h = 25 cm. r = 9 cm) which was equipped with an LED strip (250 LEDs, JnDee, 12V) mounted on the inner side of the bucke.

Table 9: *Used ratios of monomers, CTA, initiator system and solvents for the syntheses of grafting-from polymer by CTA-shuttled PET-RAFT polymerization.*

#	HEA [eq.]	SPA [eq.]	[M]=[HEA]+[SPA] [mM]	BTPA [eq.]	EoY [eq.]	AscA [eq.]	Solvent
1	200	-	0.52	1	0.018	1	H_2O
2	200	-	0.52	1	0.018	1	DMSO
3	200	-	0.52	1	0.018	1	DMF
4	200	-	0.52	1	0.018	0.1	DMSO
5	200	-	0.52	1	0.018	0.5	DMSO
6	200	-	0.52	1	0.018	5	DMSO
7	200	-	0.52	1	0.018	10	DMSO
8	500	-	0.52	1	0.018	1	DMSO
9	1000	-	0.52	1	0.018	1	DMSO
10	2000	-	0.52	1	0.018	1	DMSO
11	190	10	0.43	1	0.018	1	DMSO
12	180	20	0.43	1	0.018	1	DMSO
13	150	50	0.43	1	0.018	1	DMSO

Table 10: *Used amount of monomers, CTA, initiator solutions and solvents for the syntheses of grafting-from polymer by CTA-shuttled PET-RAFT polymerization.*

| # | Monomer | | BTPA | Stock solution | | Solvent | |
| | HEA | SPA | | EoY, 20 g·L^{-1} | AscA, 100 g·L^{-1} | Type | |
	[mg]	[mg]	[mg]	[µL]	[µL]		[µL]
1	300	-	3.4	8.2	25	H_2O	240
2	300	-	3.4	8.2	25	DMSO	240
3	300	-	3.4	8.2	25	DMF	240
4	300	-	3.4	8.2	2.5	DMSO	262
5	300	-	3.4	8.2	12.5	DMSO	252
6	300	-	3.4	8.2	124	DMSO	140
7	300	-	3.4	8.2	248	DMSO	16
8	300	-	1.3	3.3	10	DMSO	259
9	300	-	0.7	1.6	5	DMSO	266
10	300	-	0.3	0.8	2.5	DMSO	269
11	325	66	3.8	9.4	28.4	DMSO	418
12	325	138	4.1	9.9	30	DMSO	457
13	325	415	4.9	11.9	36	DMSO	607

References

[1] IEA, *IEA, Key World Energy Statistics 2021, IEA, Paris*, **2021**.

[2] K. Holmberg, A. Erdemir, *FME Transactions* **2015**, *43*, 181.

[3] J. Schneider, D. Braun, C. Greiner, *Lubricants* **2017**, *5*, 32.

[4] M. Godet, *Wear* **1984**, *100*, 437.

[5] Michael M. Khonsari and E. Richard Booser in *Recent developments in wear prevention, friction and lubrication, 2010*, Research Signpost, Kerala, India, **2010**, S. 263–278.

[6] J. M. G. Cowie, V. Arrighi in *Polymers. Chemistry and physics of modern materials* (Hrsg.: J. M. G. Cowie, V. Arrighi), CRC Press, Boca Raton, Florida, **2007**, 345-360, 366ff, 377f.

[7] C. L. Lee, K. E. Polmanteer, E. G. King, *J. Polym. Sci. A-2 Polym. Phys.* **1970**, *8*, 1909.

[8] S. Perrier, *Macromolecules* **2017**, *50*, 7433.

[9] K. Matyjaszewski, *Macromolecules* **2012**, *45*, 4015.

[10] J. Nicolas, Y. Guillaneuf, C. Lefay, D. Bertin, D. Gigmes, B. Charleux, *Prog. Polym. Sci.* **2013**, *38*, 63.

[11] G. Moad, *Polym. Chem.* **2017**, *8*, 177.

[12] T. Otsu, *J. Polym. Sci. A Polym. Chem.* **2000**, *38*, 2121.

[13] M. Hartlieb, *Macromol. Rapid Commun.* **2021**, e2100514.

[14] M. L. Allegrezza, D. Konkolewicz, *ACS Macro Lett.* **2021**, *10*, 433.

[15] J. Phommalysack-Lovan, Y. Chu, C. Boyer, J. Xu, *Chem. Commun.* **2018**, *54*, 6591.

[16] S. Ma, X. Zhang, B. Yu, F. Zhou, *NPG Asia Mater* **2019**, *11*, 1.

[17] a) X. Banquy, J. Burdyńska, D. W. Lee, K. Matyjaszewski, J. Israelachvili, *J. Am. Chem. Soc.* **2014**, *136*, 6199; b) M. T. Müller, X. Yan, S. Lee, S. S. Perry, N. D. Spencer, *Macromolecules* **2005**, *38*, 5706.

[18] B. Zdyrko, I. Luzinov, *Macromol. Rapid Commun.* **2011**, *32*, 859.

[19] C. Ligoure, L. Leibler, *J. Phys. France* **1990**, *51*, 1313.

[20] R. Barbey, L. Lavanant, D. Paripovic, N. Schüwer, C. Sugnaux, S. Tugulu, H.-A. Klok, *Chem. Rev.* **2009**, *109*, 5437.

[21] Z. Zheng, J. Ling, A. H. E. Müller, *Macromol. Rapid Commun.* **2014**, *35*, 234.

[22] a) R. J. Mart, R. K. Allemann, *Chem. Commun.* **2016**, *52*, 12262; b) X. Pang, J.-A. Lv, C. Zhu, L. Qin, Y. Yu, *Adv. Mater.* **2019**, *31*, e1904224; c) Z. Li, P. Wang, B. Liu, Y. Wang, J. Zhang, Y. Yan, Y. Ma, *Soft Matter* **2014**, *10*, 8758; d) Z. Mahimwalla, K. G. Yager, J.-i. Mamiya, A. Shishido, A. Priimagi, C. J. Barrett, *Polym. Bull.* **2012**, *69*, 967; e) H. Wen, W. Zhang, Y. Weng, Z. Hu, *RSC Adv* **2014**, *4*, 11776; f) J. Shin, J. Sung, M. Kang, X. Xie, B. Lee, K. M. Lee, T. J. White, C. Leal, N. R. Sottos, P. V. Braun et al., *Proc. Natl. Acad. Sci. U. S. A.* **2019**, *116*, 5973.

[23] H. Sakai, Y. Orihara, H. Kodashima, A. Matsumura, T. Ohkubo, K. Tsuchiya, M. Abe, *J. Am. Chem. Soc.* **2005**, *127*, 13454.

[24] S. Peng, Q. Guo, T. C. Hughes, P. G. Hartley, *Langmuir* **2014**, *30*, 866.

[25] a) H. Yamaguchi, Y. Kobayashi, R. Kobayashi, Y. Takashima, A. Hashidzume, A. Harada, *Nat. Commun.* **2012**, *3*, 603; b) A. Harada, Y. Takashima, M. Nakahata, *Acc. Chem. Res.* **2014**, *47*, 2128.

[26] M. Moniruzzaman, C. J. Sabey, G. F. Fernando, *Macromolecules* **2004**, *37*, 2572.

[27] G. Pouliquen, C. Amiel, C. Tribet, *J. Phys. Chem. B* **2007**, *111*, 5587.

[28] I. Tomatsu, A. Hashidzume, A. Harada, *Macromolecules* **2005**, *38*, 5223.

[29] a) J. Zhang, H. Tian, *Adv. Opt. Mater.* **2018**, *6*, 1701278; b) E. Orgiu, N. Crivillers, M. Herder, L. Grubert, M. Pätzel, J. Frisch, E. Pavlica, D. T. Duong, G. Bratina, A. Salleo et al., *Nat. Chem.* **2012**, *4*, 675; c) M. Lahikainen, K. Kuntze, H. Zeng, S. Helantera, S. Hecht, A. Priimagi, *ACS Appl. Mater. Interfaces* **2020**, *12*, 47939; d) M. Irie, *Chem. Rev.* **2000**, *100*, 1685; e) Z. Li, H. Chen, B. Li, Y. Xie, X. Gong, X. Liu, H. Li, Y. Zhao, *Adv. Sci.* **2019**, *6*, 1901529.

[30] S. Tang, D. Xue, J. Guo, L. Ma, Y. Tian, J. Luo, *Langmuir* **2020**, *36*, 5820.

[31] L. Li, J. M. Scheiger, P. A. Levkin, *Adv. Mater.* **2019**, *31*, e1807333.

[32] J. Chen, A. R. Vaino, R. L. Smith, S. C. Collins, *J. Polym. Sci. A Polym. Chem.* **2008**, *46*, 3482.

[33] C.-M. Chung, Y.-S. Roh, S.-Y. Cho, J.-G. Kim, *Chem. Mater.* **2004**, *16*, 3982.

[34] a) B. Jin, H. Song, R. Jiang, J. Song, Q. Zhao, T. Xie, *Sci. Adv.* **2018**, *4*, eaao3865; b) Y. Nakayama, T. Matsuda, *J. Polym. Sci. A Polym. Chem.* **1992**, *30*, 2451.

[35] M. Micic, Y. Zheng, V. Moy, X.-H. Zhang, F. M. Andreopoulos, R. M. Leblanc, *Colloids Surf. B* **2003**, *27*, 147.

[36] S. R. Trenor, A. R. Shultz, B. J. Love, T. E. Long, *Chem. Rev.* **2004**, *104*, 3059.

[37] A. S. Fawcett, M. A. Brook, *Macromolecules* **2014**, *47*, 1656.

[38] R. Jellali, V. Bertrand, M. Alexandre, N. Rosière, M. Grauwels, M.-C. de Pauw-Gillet, C. Jérôme, *Macromol. Biosci.* **2017**, *17*.

[39] J. van Damme, O. van den Berg, J. Brancart, L. Vlaminck, C. Huyck, G. van Assche, B. van Mele, F. Du Prez, *Macromolecules* **2017**, *50*, 1930.

[40] Z. Du, Y. Shan, J. Luo, N. Sun, B. Ren, *ACS Macro Lett.* **2019**, *8*, 279.

REFERENCES

[41] J. van Damme, F. Du Prez, *Prog. Polym. Sci.* **2018**, *82*, 92.

[42] a) M. Liu, W. Wenzel, H. Frisch, *Polym. Chem.* **2020**, *11*, 6616; b) D. E. Marschner, H. Frisch, J. T. Offenloch, B. T. Tuten, C. R. Becer, A. Walther, A. S. Goldmann, P. Tzvetkova, C. Barner-Kowollik, *Macromolecules* **2018**, *51*, 3802.

[43] V. X. Truong, F. Li, F. Ercole, J. S. Forsythe, *ACS Macro Lett.* **2018**, *7*, 464.

[44] S. Abou-Hatab, V. A. Spata, S. Matsika, *J. Phys. Chem. A* **2017**, *121*, 1213.

[45] R. S. L. Shon, D. O. Cowan, W. W. Schmiegel, *J. Phys. Chem.* **1975**, *79*, 2087.

[46] H. Bouas-Laurent, J.-P. Desvergne, A. Castellan, R. Lapouyade, *Chem. Soc. Rev.* **2000**, *29*, 43.

[47] a) Y. Li, M. Goswami, Y. Zhang, T. Liu, J. Zhang, M. R. Kessler, L. Wang, O. Rios, *Sci Rep* **2020**, *10*, 20214; b) K. Jin, A. Banerji, D. Kitto, F. S. Bates, C. J. Ellison, *ACS Appl. Mater. Interfaces* **2019**, *11*, 12863.

[48] a) H. Zhang, X. Li, Y. Lin, F. Gao, Z. Tang, P. Su, W. Zhang, Y. Xu, W. Weng, R. Boulatov, *Nat. Commun.* **2017**, *8*, 1147; b) L. Kan, H. Cheng, B. Li, X. Zhang, Q. Wang, H. Wei, N. Ma, *New J. Chem.* **2019**, *43*, 2658.

[49] N. Oya, P. Sukarsaatmadja, K. Ishida, N. Yoshie, *Polym J* **2012**, *44*, 724.

[50] Y. Zheng, M. Micic, S. V. Mello, M. Mabrouki, F. M. Andreopoulos, V. Konka, S. M. Pham, R. M. Leblanc, *Macromolecules* **2002**, *35*, 5228.

[51] H. Bouas-Laurent, J.-P. Desvergne, A. Castellan, R. Lapouyade, *Chem. Soc. Rev.* **2001**, *30*, 248.

[52] Y.-K. Song, C.-M. Chung, *Polym. Chem.* **2013**, *4*, 4940.

[53] R. Jellali, M. Alexandre, C. Jérôme, *Polym. Chem.* **2017**, *8*, 2499.

[54] A. S. Fawcett, T. C. Hughes, L. Zepeda-Velazquez, M. A. Brook, *Macromolecules* **2015**, *48*, 6499.

[55] W. Tian, J. Tian, *Dyes Pigm.* **2014**, *105*, 66.

[56] C. Li, Y. Zhang, J. Hu, J. Cheng, S. Liu, *Angew. Chem., Int. Ed. Engl.* **2010**, *49*, 5120.

[57] Z. Tian, W. Wu, W. Wan, A. D. Q. Li, *J. Am. Chem. Soc.* **2009**, *131*, 4245.

[58] M. Bletz, U. Pfeifer-Fukumura, U. Kolb, W. Baumann, *J. Phys. Chem. A* **2002**, *106*, 2232.

[59] H. Cui, H. Liu, S. Chen, R. Wang, *Dyes Pigm.* **2015**, *115*, 50.

[60] S. Samanta, J. Locklin, *Langmuir* **2008**, *24*, 9558.

[61] a) L. Ma, J. Li, D. Han, H. Geng, G. Chen, Q. Li, *Macromol. Chem. Phys.* **2013**, *214*, 716; b) K. Sumaru, M. Kameda, T. Kanamori, T. Shinbo, *Macromolecules* **2004**, *37*, 4949.

[62] Y. Arisaka, A. Tamura, K. Uchida, H. Yajima, *Chem. Lett.* **2010**, *39*, 58.

[63] H. Gruler, R. Vilanove, F. Rondelez, *Phys. Rev. Lett.* **1980**, *44*, 590.

[64] A. A. García, S. Cherian, J. Park, D. Gust, F. Jahnke, R. Rosario, *J. Phys. Chem. A* **2000**, *104*, 6103.

[65] L. Kortekaas, W. R. Browne, *Chem. Soc. Rev.* **2019**, *48*, 3406.

[66] E. Berman, R. E. Fox, F. D. Thomson, *J. Am. Chem. Soc.* **1959**, *81*, 5605.

[67] M. H. Barbee, T. Kouznetsova, S. L. Barrett, G. R. Gossweiler, Y. Lin, S. K. Rastogi, W. J. Brittain, S. L. Craig, *J. Am. Chem. Soc.* **2018**, *140*, 12746.

[68] M. J. Feeney, S. W. Thomas, *Macromolecules* **2018**, *51*, 8027.

[69] E. Goldburt, F. Shvartsman, S. Fishman, V. Krongauz, *Macromolecules* **1984**, *17*, 1225.

[70] Y. Shiraishi, M. Itoh, T. Hirai, *Phys. Chem. Chem. Phys.* **2010**, *12*, 13737.

[71] F. Jiang, S. Chen, Z. Cao, G. Wang, *Polymer* **2016**, *83*, 85.

[72] S. Guragain, B. P. Bastakoti, M. Ito, S.-i. Yusa, K. Nakashima, *Soft Matter* **2012**, *8*, 9628.

[73] Y. Zhang, M. Cao, B. Yuan, T. Guo, W. Zhang, *Polym. Chem.* **2017**, *8*, 7325.

[74] O. Grimm, F. H. Schacher, *Polymers* **2018**, *10*, 645.

[75] Y. Zhao, L. Tremblay, Y. Zhao, *J. Polym. Sci. A Polym. Chem.* **2010**, *48*, 4055.

[76] Y. Jia, W.-J. Wang, B.-G. Li, S. Zhu, *Macromol. Mater. Eng.* **2018**, *303*, 1800154.

[77] D. A. Davis, A. Hamilton, J. Yang, L. D. Cremar, D. van Gough, S. L. Potisek, M. T. Ong, P. V. Braun, T. J. Martínez, S. R. White et al., *Nature* **2009**, *459*, 68.

[78] R. Klajn, *Chem. Soc. Rev.* **2014**, *43*, 148.

[79] D. Hu, Z. Tian, W. Wu, W. Wan, A. D. Q. Li, *J. Am. Chem. Soc.* **2008**, *130*, 15279.

[80] a) H.-I. Lee, W. Wu, J. K. Oh, L. Mueller, G. Sherwood, L. Peteanu, T. Kowalewski, K. Matyjaszewski, *Angew. Chem., Int. Ed. Engl.* **2007**, *46*, 2453; b) V. K. Kotharangannagari, A. Sánchez-Ferrer, J. Ruokolainen, R. Mezzenga, *Macromolecules* **2011**, *44*, 4569.

[81] Y.-N. Zhou, J.-J. Li, Q. Zhang, Z.-H. Luo, *Langmuir* **2014**, *30*, 12236.

[82] K. Nagata, T. Kurebayashi, K. Imato, N. Takeda, *J. Mater. Chem. B* **2018**, *6*, 2052.

[83] C.-J. Chen, Q. Jin, G.-Y. Liu, D.-D. Li, J.-L. Wang, J. Ji, *Polymer* **2012**, *53*, 3695.

[84] K. Schöller, S. Küpfer, L. Baumann, P. M. Hoyer, D. de Courten, R. M. Rossi, A. Vetushka, M. Wolf, N. Bruns, L. J. Scherer, *Adv. Funct. Mater.* **2014**, *24*, 5194.

[85] S. Coleman, J. ter Schiphorst, A. Ben Azouz, S. Bakker, A. P.H.J. Schenning, D. Diamond, *Sens. Actuators B Chem.* **2017**, *245*, 81.

[86] B. Ziółkowski, L. Florea, J. Theobald, F. Benito-Lopez, D. Diamond, *Soft Matter* **2013**, *9*, 8754.

[87] a) Y. Shiraishi, R. Miyamoto, T. Hirai, *Org. Lett.* **2009**, *11*, 1571; b) H. Schenderlein, A. Voss, R. W. Stark, M. Biesalski, *Langmuir* **2013**, *29*, 4525; c) S. Chen, F. Jiang, Z. Cao, G. Wang, Z.-M. Dang, *Chem. Commun.* **2015**, *51*, 12633; d) V. A. Krongauz, E. S. Goldburt, *Macromolecules* **1981**, *14*, 1382.

REFERENCES

[88]   M. Piech, N. S. Bell, *Macromolecules* **2006**, *39*, 915.

[89]   L.-X. Yu, Y. Liu, S.-C. Chen, Y. Guan, Y.-Z. Wang, *Chin. Chem. Lett.* **2014**, *25*, 389.

[90]   C.-Q. Huang, Y. Wang, C.-Y. Hong, C.-Y. Pan, *Macromol. Rapid Commun.* **2011**, *32*, 1174.

[91]   X. Wang, J. Hu, G. Liu, J. Tian, H. Wang, M. Gong, S. Liu, *J. Am. Chem. Soc.* **2015**, *137*, 15262.

[92]   W.-J. Zhang, C.-Y. Hong, C.-Y. Pan, *Macromol. Chem. Phys.* **2013**, *214*, 2445.

[93]   D. Liu, C. W. M. Bastiaansen, J. M. J. den Toonder, D. J. Broer, *Angew. Chem., Int. Ed. Engl.* **2012**, *51*, 892.

[94]   D. Liu, D. J. Broer, *Angew. Chem., Int. Ed. Engl.* **2014**, *53*, 4542.

[95]   D. Liu, D. J. Broer, *Soft Matter* **2014**, *10*, 7952.

[96]   A. Ryabchun, F. Lancia, N. Katsonis, *ACS Appl. Mater. Interfaces* **2021**, *13*, 4777.

[97]   D. Xue, L. Ma, Y. Tian, Q. Zeng, B. Tu, W. Luo, S. Wen, J. Luo, *Front. Chem.* **2021**, *9*, 707232.

[98]   J. Blass, B. L. Bozna, M. Albrecht, J. A. Krings, B. J. Ravoo, G. Wenz, R. Bennewitz, *Chem. Commun.* **2015**, *51*, 1830.

[99]   B. L. Perotti, A. Cammarata, F. Cemin, S. R. Sales de Mello, L. M. Leidens, F. G. Echeverrigaray, T. Minea, F. Alvarez, A. F. Michels, T. Polcar et al., *ACS Appl. Mater. Interfaces* **2021**, *13*, 43746.

[100] T. Tadros in *Encyclopedia of Colloid and Interface Science* (Hrsg.: T. Tadros), Springer Berlin Heidelberg, Berlin, Heidelberg, **2013**, S. 209–210.

[101] Z. Chu, C. A. Dreiss, Y. Feng, *Chem. Rev.* **2013**, *42*, 7174.

[102] a) T. Wolff, C. S. Emming, T. A. Suck, G. von Buenau, *J. Phys. Chem.* **1989**, *93*, 4894; b) N. Müller, T. Wolff, G. von Bünau, *J. Photochem.* **1984**, *24*, 37.

[103] H. Oh, A. M. Ketner, R. Heymann, E. Kesselman, D. Danino, D. E. Falvey, S. R. Raghavan, *Soft Matter* **2013**, *9*, 5025.

[104] E. A. Kelly, N. Willis-Fox, J. E. Houston, C. Blayo, G. Divitini, N. Cowieson, R. Daly, R. C. Evans, *Nanoscale* **2020**, *12*, 6300.

[105] a) B. Song, Y. Hu, J. Zhao, *J. Colloid Interface Sci.* **2009**, *333*, 820; b) C. T. Lee, K. A. Smith, T. A. Hatton, *Macromolecules* **2004**, *37*, 5397.

[106] a) H.-Y. Lee, K. K. Diehn, K. Sun, T. Chen, S. R. Raghavan, *J. Am. Chem. Soc.* **2011**, *133*, 8461; b) M.-Y. Cho, J.-S. Kim, H. J. Choi, S.-B. Choi, G.-W. Kim, *Smart Mater. Struct.* **2017**, *26*, 54007.

[107] R. Dong, J. Peng, X. Chang, Q. Zhang, L. Hong, B. Ren, *J. Rheol.* **2017**, *61*, 107.

[108] a) M. Irie, Y. Hirano, S. Hashimoto, K. Hayashi, *Macromolecules* **1981**, *14*, 262; b) G. Pouliquen, C. Tribet, *Macromolecules* **2006**, *39*, 373.

[109] S. Tamesue, Y. Takashima, H. Yamaguchi, S. Shinkai, A. Harada, *Angew. Chem., Int. Ed. Engl.* **2010**, *49*, 7461.

[110] a) M. Moniruzzaman, C. J. Sabey, G. F. Fernando, *Polymer* **2007**, *48*, 255; b) A. Menju, K. Hayashi, M. Irie, *Macromolecules* **1981**, *14*, 755.

[111] Z. Du, X. Yan, R. Dong, K. Ke, B. Ren, Z. Tong, *Macromolecules* **2018**, *51*, 1518.

[112] J. Klein, *Proc. Inst. Mech. Eng. J* **2006**, *220*, 691.

[113] R. M. Bielecki, M. Crobu, N. D. Spencer, *Tribol. Lett.* **2013**, *49*, 263.

[114] J. Klein, E. Kumacheva, D. Mahalu, D. Perahia, L. J. Fetters, *Nature* **1994**, *370*, 634.

[115] S. Watson, M. Nie, L. Wang, K. Stokes, *RSC Adv.* **2015**, *5*, 89698.

[116] P. Mocny, H.-A. Klok, *Mol. Syst. Des. Eng.* **2016**, *1*, 141.

[117] Y. Yu, M. Brió Pérez, C. Cao, S. de Beer, *Eur. Polym. J.* **2021**, *147*, 110298.

[118] D. P. Chang, J. E. Dolbow, S. Zauscher, *Langmuir* **2007**, *23*, 250.

[119] Y. Yu, B. D. Kieviet, F. Liu, I. Siretanu, E. Kutnyánszky, G. J. Vancso, S. de Beer, *Soft Matter* **2015**, *11*, 8508.

[120] Y. Yu, M. Cirelli, B. D. Kieviet, E. S. Kooij, G. J. Vancso, S. de Beer, *Polymer* **2016**, *102*, 372.

[121] Q. Wei, M. Cai, F. Zhou, W. Liu, *Macromolecules* **2013**, *46*, 9368.

[122] H. Zeng, Y. Zhang, S. Mao, H. Nakajima, K. Uchiyama, *J. Mater. Chem. C* **2017**, *5*, 5877.

[123] J. E. Mark (Hrsg.) *Polymer data handbook*, Oxford University Press, New York, NY, **1999**.

[124] M. H. Mazurek in *Comprehensive Organometallic Chemistry III* (Hrsg.: M. H. Mazurek), Elsevier, **2007**, S. 673.

[125] C. Gäbert, T. Rosenstingl, D. Linsler, M. Dienwiebel, S. Reinicke, *ACS Appl. Polym. Mater.* **2020**, *2*, 5460.

[126] M. A. J. Bayliss, R. B. Homer, M. J. Shepherd, *J. Chem. Soc., Chem. Commun.* **1990**, 305.

[127] J. D. Ferry, *Viscoelastic properties of polymers*, John Wiley & Sons, New York, Chichester, Brisbane, Toronto, Singapore, **1980**.

[128] M. Klaper, P. Wessig, T. Linker, *Chem. Commun.* **2016**, *52*, 1210.

[129] J.-M. Aubry, C. Pierlot, J. Rigaudy, R. Schmidt, *Acc. Chem. Res.* **2003**, *36*, 668.

[130] R. Ballardini, G. Beggiato, P. Bortolus, A. Faucitano, A. Buttafava, F. Gratani, *Polym. Degrad. Stab* **1984**, *7*, 41.

[131] H. Jacobson, W. H. Stockmayer, *J. Chem. Phys.* **1950**, *18*, 1600.

[132] K. Skrabania, A. Miasnikova, A. M. Bivigou-Koumba, D. Zehm, A. Laschewsky, *Polym. Chem.* **2011**, *2*, 2074.

REFERENCES

[133] a) J. Xu, S. Shanmugam, N. A. Corrigan, C. Boyer in *ACS Symposium Series*, *Vol. 1187* (Hrsg.: K. Matyjaszewski, B. S. Sumerlin, N. V. Tsarevsky, J. Chiefari), ACS American Chemical Society, Washington, **2015**, S. 247–267; b) T. G. McKenzie, Q. Fu, E. H. H. Wong, D. E. Dunstan, G. G. Qiao, *Macromolecules* **2015**, *48*, 3864.

[134] a) T. Foldesberezhnykh, *Eur. Polym. J.* **1972**, *8*, 1247; b) G. Odian in *Principles of polymerization* (Hrsg.: G. G. Odian), Wiley, Hoboken, N.J, **2004**, S. 259–265.

[135] N. Díez, A. Śliwak, S. Gryglewicz, B. Grzyb, G. Gryglewicz, *RSC Adv.* **2015**, *5*, 81831.

[136] G. Beamson, D. Briggs, *High resolution XPS of organic polymers. The Scienta ESCA300 database*, Wiley, Chichester, **1992**.

[137] a) M. Delamar, J.-L. Albert, J. Aubard, J.-E. Dubois, *J. Electron Spectrosc. Relat. Phenom.* **1983**, *32*, 351; b) M. Piantek, G. Schulze, M. Koch, K. J. Franke, F. Leyssner, A. Krüger, C. Navío, J. Miguel, M. Bernien, M. Wolf et al., *J. Am. Chem. Soc.* **2009**, *131*, 12729.

[138] a) K. Bian, M. F. Cunningham, *Macromolecules* **2005**, *38*, 695; b) K. L. Robinson, M. A. Khan, M. V. de Paz Báñez, X. S. Wang, S. P. Armes, *Macromolecules* **2001**, *34*, 3155.

[139] J. Yeow, R. Chapman, J. Xu, C. Boyer, *Polym. Chem.* **2017**, *8*, 5012.

[140] J. Xu, S. Shanmugam, H. T. Duong, C. Boyer, *Polym. Chem.* **2015**, *6*, 5615.

[141] D. R. Pemberton, A. F. Johnson, *Polymer* **1984**, *25*, 536.

[142] J. Deitzel, *Polymer* **2002**, *43*, 1025.

[143] Kresse, Furthmüller, *Phys. Rev. B* **1996**, *54*, 11169.

[144] a) G. Kresse, D. Joubert, *Phys. Rev. B* **1999**, *59*, 1758; b) Blöchl, *Phys. Rev. B* **1994**, *50*, 17953.

[145] a) S. Grimme, J. Antony, S. Ehrlich, H. Krieg, *J. Chem. Phys.* **2010**, *132*, 154104; b) S. Grimme, S. Ehrlich, L. Goerigk, *J. Comput. Chem.* **2011**, *32*, 1456.

[146] S. C. Larnaudie, J. C. Brendel, K. A. Jolliffe, S. Perrier, *J. Polym. Sci. A Polym. Chem.* **2016**, *54*, 1003.

[147] F. M. Raymo, S. Giordani, *J. Am. Chem. Soc.* **2001**, *123*, 4651.

[148] P. Akarsu, R. Grobe, J. Nowaczyk. M. Hartlieb, S. Reinicke, A. Böker, M. Sperling, M. Reifrath, *Appl. Polym. Mater.* **2021**, 3, 5, 2420-2431
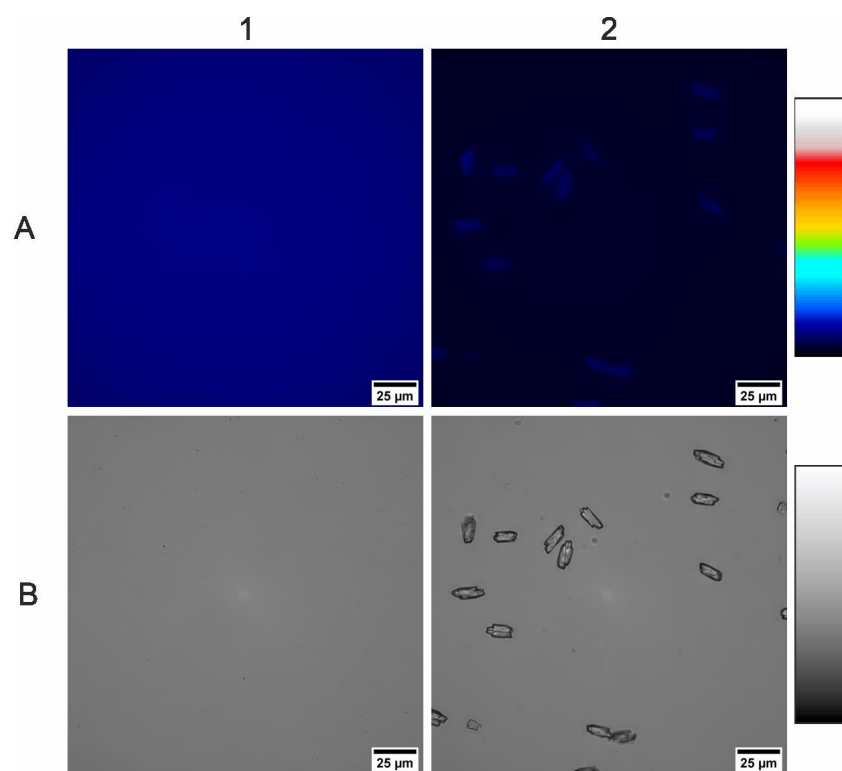
Appendix

Figure 31:   *FM (A) and BF (B) images of a saturated solution of 9-anthracenecarboxylic acid ethyl ester in a PDMS base oil. Before radiation (1), the anthracene derivative was dissolved. After radiation (2) with UV-A, crystals were apparent.*
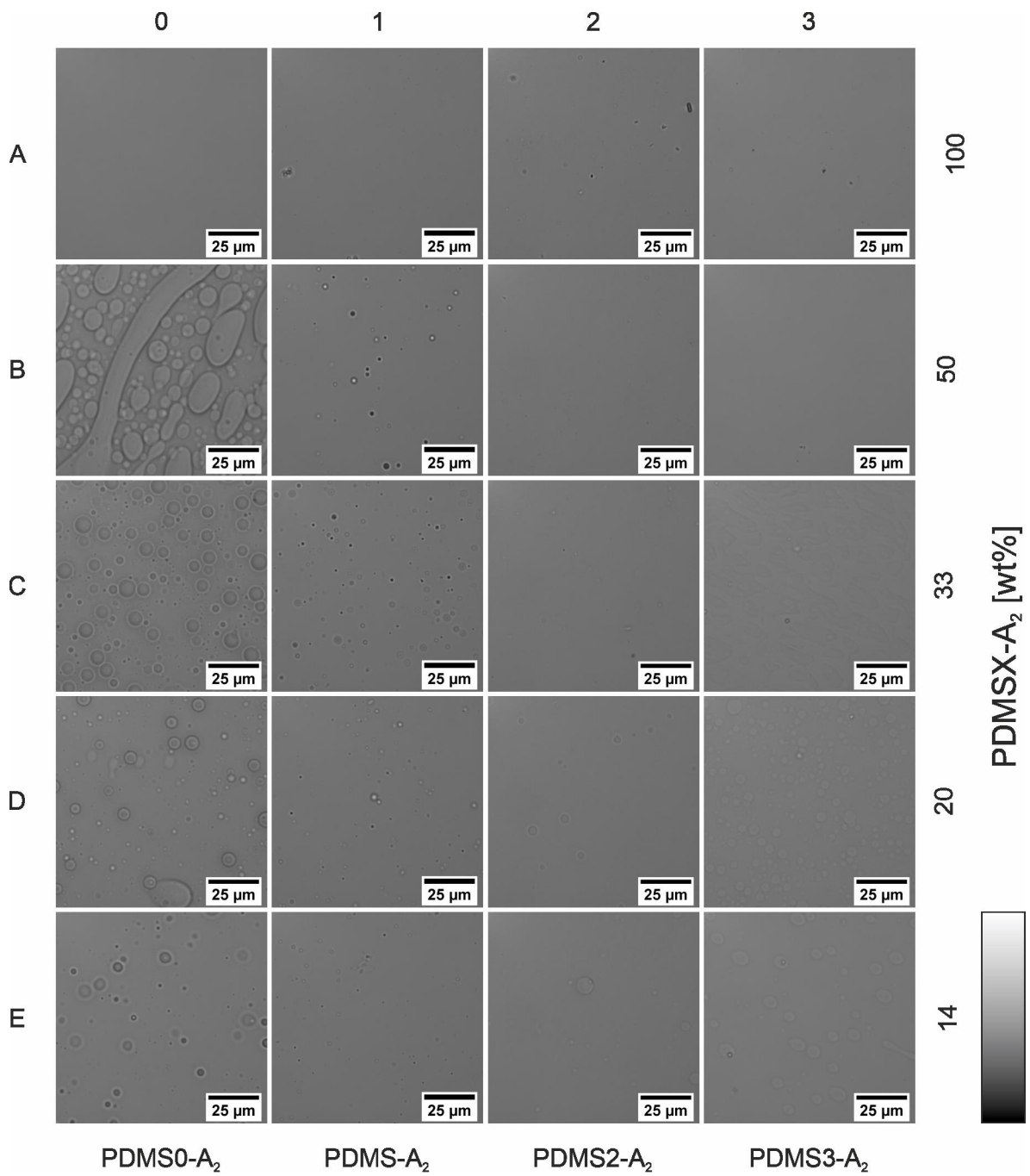
Figure 32:   BF images of mixtures of either (0) PDMS0-A_2, (1) PDMS-A_2, (2) PDMS2-A_2 or (3) PDMS3-A_2 with PDMS base oil in (A-E) varying mass fractions. Associated-field microscopy images are shown in Figure 16.
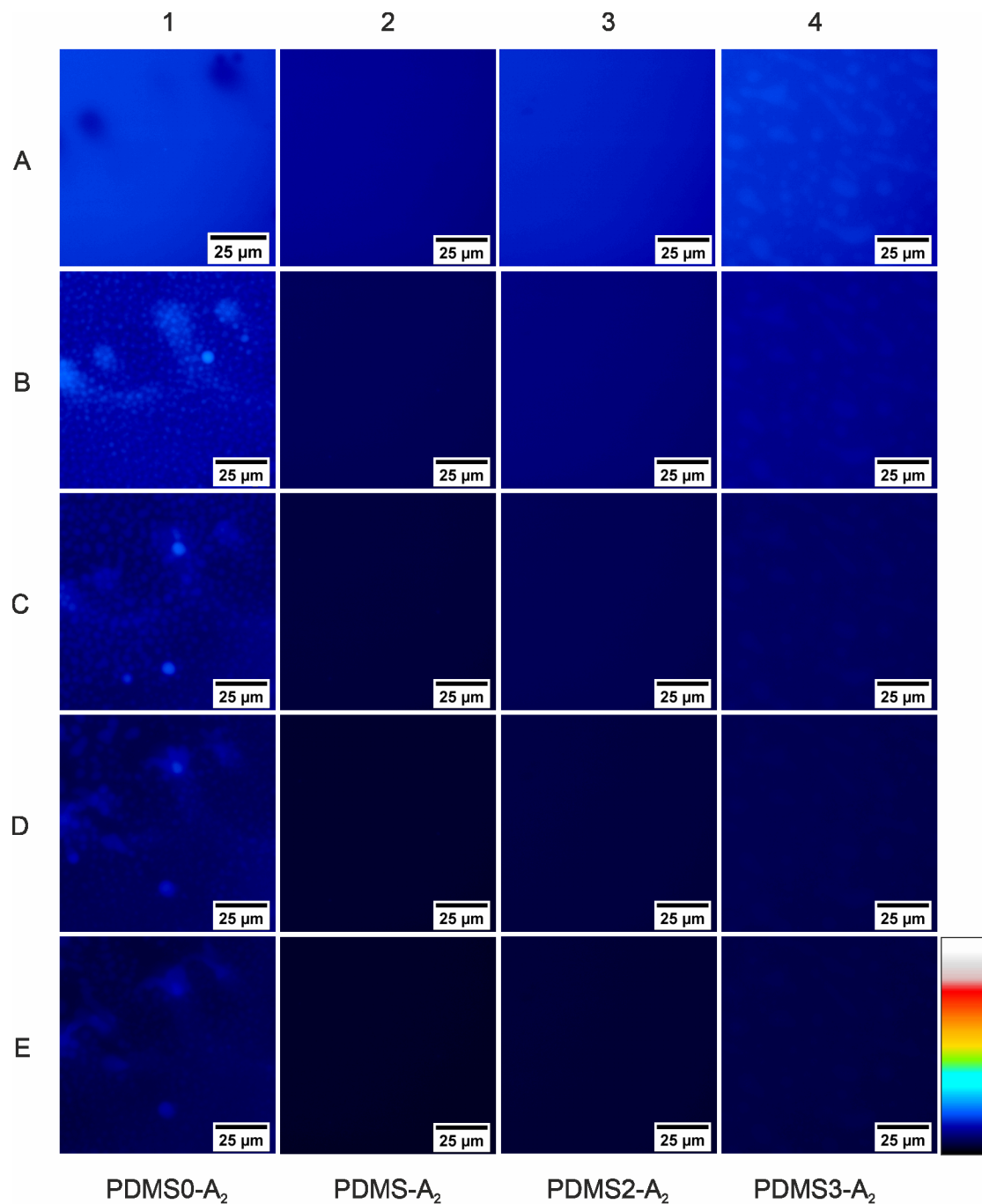
	1	2	3	4
A	25 µm	25 µm	25 µm	25 µm
B	25 µm	25 µm	25 µm	25 µm
C	25 µm	25 µm	25 µm	25 µm
D	25 µm	25 µm	25 µm	25 µm
E	25 µm	25 µm	25 µm	25 µm

PDMS0-A$_2$ PDMS-A$_2$ PDMS2-A$_2$ PDMS3-A$_2$

Figure 33:   *FM images of mixtures composed of PDMS base oil with 33 wt% of either (0) PDMS0-A$_2$, (1) PDMS-A$_2$, (2) PDMS2-A$_2$ or (3) PDMS3-A$_2$ (A) before (B-E) and after four radiation cycles with UV-A light.. The radiation cycles (B-E) were subsequently performed every 15 s. Associated BF images are shown in Figure 17.*
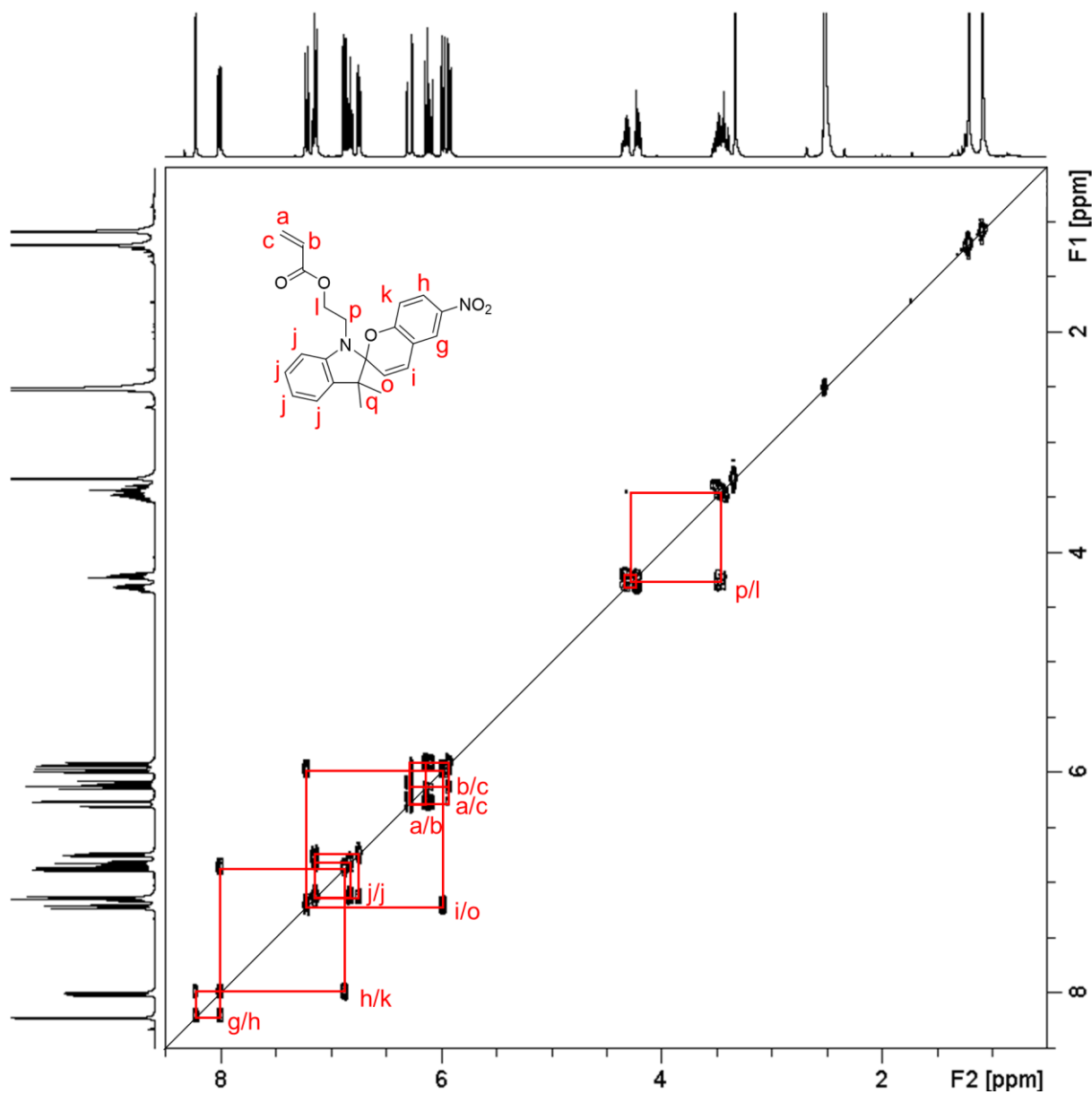
Figure 34: ^1H-^1H-COSY spectrum of SPA supporting assignment of SPA signals (see Figure 21).
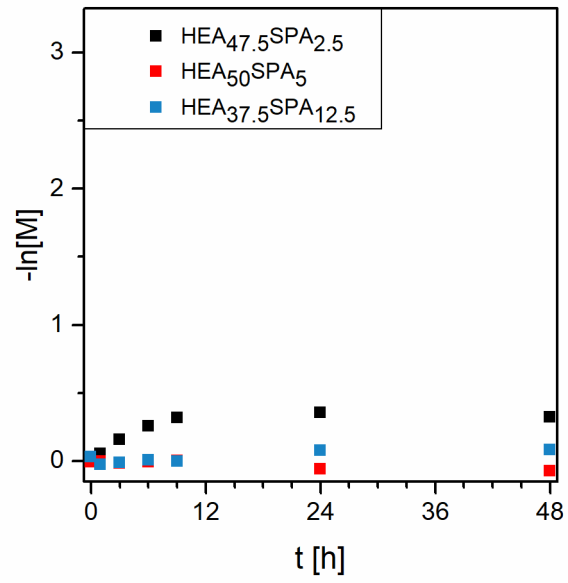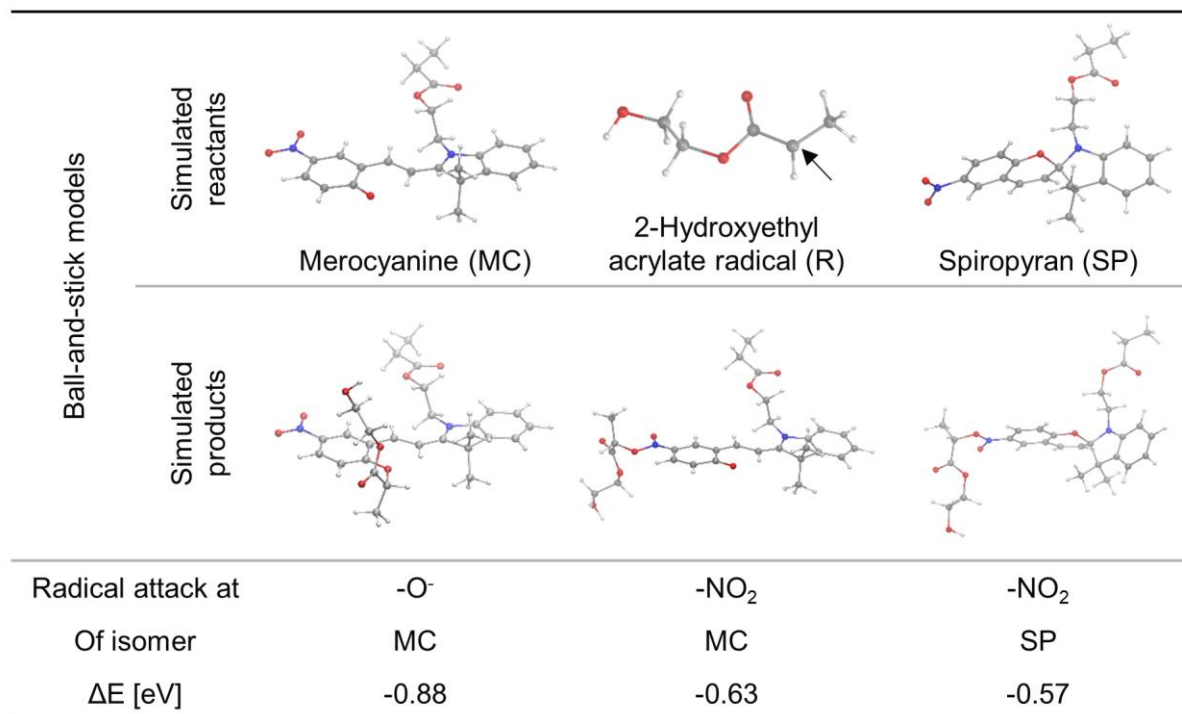
Figure 35:   *First order kinetic plot of the HEA and SPA copolymerization experiments with different monomer feed ratios in the dark.*

Scheme 18: Ball-and-stick models (red = O, blue = N, dark grey = C, light grey = H) and calculated radical association energies of the DFT simulation for the attack of a monomer radical on different ring substituents of spiropyran or merocyanine isomer.
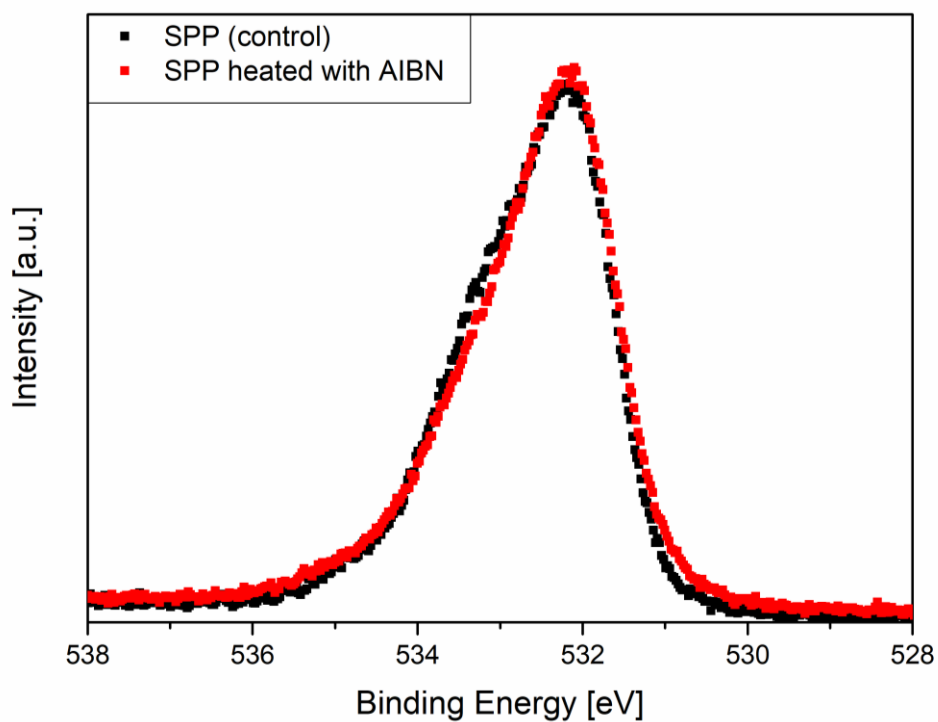

Figure 36: O1s peak of the XPS spectra of SPP after heating with AIBN as radical source and of SPP after heating as control experiment.